

# HRMA Effective Area: SSD C-continuum Measurements

*Ping Zhao*

## 11.1 Introduction

During the calibration, the HRMA on-axis effective area was measured in two different ways in terms of the X-ray source characteristics: the discrete line measurements and the carbon-continuum (C-continuum) measurements. The former uses characteristic X-ray lines generated by an Electron Impact Point Source (EIPS) with various anodes. The latter uses continuum X-ray radiation generated by EIPS with a carbon anode at 15 kV and using a beryllium (Be) filter to attenuate the lowest energies including the C-K $\alpha$  line (0.277 keV). A preliminary result of this measurement was reported in SPIE '98 (Kolodziejczak et al., 1997).

For the X-ray line measurements, both Flow Proportional Counter (FPC) and Solid State Detector (SSD) were used. For the FPC, 4 energy lines (C-K $\alpha$ : 0.277 keV; Al-K $\alpha$ : 1.486 keV; Ti-K $\alpha$ : 4.51 keV; Fe-K $\alpha$ : 6.40 keV) were used for four individual shells effective area measurements, and 3 energy lines (Cu-L $\alpha$ : 0.9297 keV; Cr-K $\alpha$ : 5.41 keV; Cu-K $\alpha$ : 8.03 keV) were used for the HRMA (all four shells open) effective area measurements. Several other energy lines were used for the HRMA or MEG (Shells 1 and 3 open) or HEG (Shells 4 and 6 open) configurations and with 1 mm and 0.5 mm apertures only. For the SSD, 3 energy lines (Nb-L $\alpha$ : 2.16 keV; Ag-L $\alpha$ : 2.98 keV; Sn-L $\alpha$ : 3.44 keV) were used for the HRMA (all four shells open) effective area measurements. Four energy lines (Al-K $\alpha$ : 1.486 keV; Ag-L $\alpha$ : 2.98 keV; Fe-K $\alpha$ : 6.40 keV; Cu-K $\alpha$ : 8.03 keV) were used for the MEG and HEG configurations and with 0.5 mm aperture only. No SSD measurements were made for the effective area of individual shells.

For the continuum measurements, only SSD was used, and only the effective area of each individual shell were measured. The effective area was measured for each individual mirror shell by comparing the spectrum detected by `ssd_x` (SSD at the HRMA focal plane) with the spectrum detected simultaneously by `ssd_5` (SSD in Building 500 of the XRCF, to one side of the X-ray beam). The continuum measurements have the advantage of providing the effective area data for nearly the entire AXAF energy band, but the data analysis and results evaluation need careful attention. Factors such as SSD response, pileup correction, energy scale, deadtime correction, quantum efficiency, background, icing effect, *etc.*, need to be carefully evaluated.

This Chapter discusses the data analysis and HRMA effective area measured using the C-continuum source and solid state detectors. The results are compared with the X-ray line measurements and with the HRMA raytracing models. The comparison are used to make an on-orbit HRMA effective area prediction.

## 11.2 SSD C-continuum Effective Area Measurements

The effective area measurements with the C-continuum Source were made with two nearly identical high-purity-germanium solid state detectors: one (`ssd_5`) is a beam-normalization-detector (BND) located at 38.199 meters from the source in Building 500, another one (`ssd_x`) is the focal plane detector located at the HRMA focus, 537.778 meters from the source. An aperture wheel was mounted in front of each SSD. The HRMA effective area was measured with a 2 mm diameter aperture in front of the `ssd_5` and apertures with various sizes in front of the `ssd_x`.

Table 11.1 lists all the on-axis effective area measurements with the C-continuum source and SSD detectors. The measurements were made for each of the four HRMA shells. No measurement was made when all four shells were open. Apertures ranging from 0.015 mm to 2 mm diameters were used in front of the `ssd_x` for the measurements. In several measurements of shell 3 (runids 108447–108456), the `ssd_5` was inadvertently turned off. For one measurement of shell 4 (runid 108478), the `ssd_x` was tripped off. Most of the measurements were made in Phase-D on 970112-970113 (Date notation for 12-13 Jan 1997), with various apertures on `ssd_x` and 300-second integrations. One set of measurements was made in Phase-E on 970130 with only the 2 mm aperture on `ssd_x` and 1000-second integrations.

Table 11.2 lists all the off-axis effective area measurements with C-continuum source and SSD detectors. These measurements were made in Phase-E on 970131 with apertures ranging from 0.04 mm to 2 mm diameters, 300-second integrations, and off-axis angles of 5', 10', 15', 20', 25', and 30'.

For the on-axis effective area, measurements with the TRW IDs E-IXS-MC-15.001,2,3,4 (Run ID: 110539, 110540, 110541, 110542) had the longest integration time and the largest apertures. In this Chapter we use this set of data to demonstrate the data reduction and to make the HRMA effective area predictions from this result. All other sets of data can be processed the same way.

Figures 11.1–11.4 show the `ssd_x` and `ssd_5` spectra of this set of measurements. The profiles show the C-continuum spectra with several spectral peaks on top. The largest Gaussian-like peak at around channels 2400–2500 is the injected pulser spectrum to be used for the pileup and deadtime corrections (see §11.3 and §11.6). Other peaks are characteristic X-ray lines due to contaminations to the carbon anode. These peaks will be used to determine the energy scale (see §11.5).

There are many factors need to be considered during the data analysis process, such as the pileup correction, deadtime correction, X-ray beam uniformity, SSD quantum efficiency, SSD energy scale, SSD background, SSD icing effect, etc. We will explain each of these effect in the following sections while we go through the data processing procedure.

### 11.3 Pileup Correction

Before analyzing the SSD spectra, the first thing to do is to make the pileup correction. Pileups are when more than one photon enter the detector within a small time window (a few  $\mu\text{sec}$ ). Instead of recording each photon event, the detector registers only one event with the summed energy of all photons. The pileup can also occur for a real photon with a pulser event. The SSD has pileup rejection electronics to reduce the pileup. However, the rejection does not work well if one of the

Table 11.1: HRMA On-axis Effective Area Measurements

Source: C-continuum      Detector: SSD

TRW ID	Run ID	Date	Shell	Aper ( $\mu\text{m}$ )	Int (sec)	Note
D-IXS-EE-1.001	108425	970112	1	500	300	
D-IXS-EE-1.001	108426	970112	1	2000	300	
D-IXS-EE-1.001	108428	970112	1	70	300	
D-IXS-EE-1.001	108430	970112	1	50	300	
D-IXS-EE-1.001	108432	970112	1	40	300	
D-IXS-EE-1.001	108434	970112	1	30	300	
D-IXS-EE-1.001	108438	970112	1	20	300	
D-IXS-EE-1.001	108441	970112	1	15	300	
D-IXS-EE-1.002	108444	970113	3	100	300	
D-IXS-EE-1.002	108447	970113	3	200	300	SSD-500 off
D-IXS-EE-1.002	108449	970113	3	500	300	SSD-500 off
D-IXS-EE-1.002	108450	970113	3	2000	300	SSD-500 off
D-IXS-EE-1.002	108452	970113	3	70	300	SSD-500 off
D-IXS-EE-1.002	108454	970113	3	50	10	SSD-500 off
D-IXS-EE-1.002	108455	970113	3	50	10	SSD-500 off
D-IXS-EE-1.002	108456	970113	3	50	10	SSD-500 off
D-IXS-EE-1.002	108457	970113	3	50	1500	
D-IXS-EE-1.002	108460	970113	3	50	300	
D-IXS-EE-1.002	108462	970113	3	40	300	
D-IXS-EE-1.002	108464	970113	3	30	300	
D-IXS-EE-1.002	108467	970113	3	20	300	
D-IXS-EE-1.003	108473	970113	4	100	300	
D-IXS-EE-1.003	108475	970113	4	200	300	
D-IXS-EE-1.003	108478	970113	4	500	300	SSD-X off
D-IXS-EE-1.003	108484	970113	4	2000	300	
D-IXS-EE-1.003	108486	970113	4	70	300	
D-IXS-EE-1.003	108488	970113	4	50	300	
D-IXS-EE-1.003	108490	970113	4	40	300	
D-IXS-EE-1.003	108492	970113	4	30	300	
D-IXS-EE-1.003	108494	970113	4	20	300	
D-IXS-EE-1.004	108496	970113	6	100	300	
D-IXS-EE-1.004	108498	970113	6	200	300	
D-IXS-EE-1.004	108499	970113	6	500	300	
D-IXS-EE-1.004	108500	970113	6	2000	300	
D-IXS-EE-1.004	108502	970113	6	70	300	
D-IXS-EE-1.004	108504	970113	6	50	300	
D-IXS-EE-1.004	108506	970113	6	40	300	
D-IXS-EE-1.004	108508	970113	6	30	300	
E-IXS-MC-15.001	110539	970130	1	2000	1000	
E-IXS-MC-15.002	110540	970130	3	2000	1000	
E-IXS-MC-15.003	110541	970130	4	2000	1000	
E-IXS-MC-15.004	110542	970130	6	2000	1000	

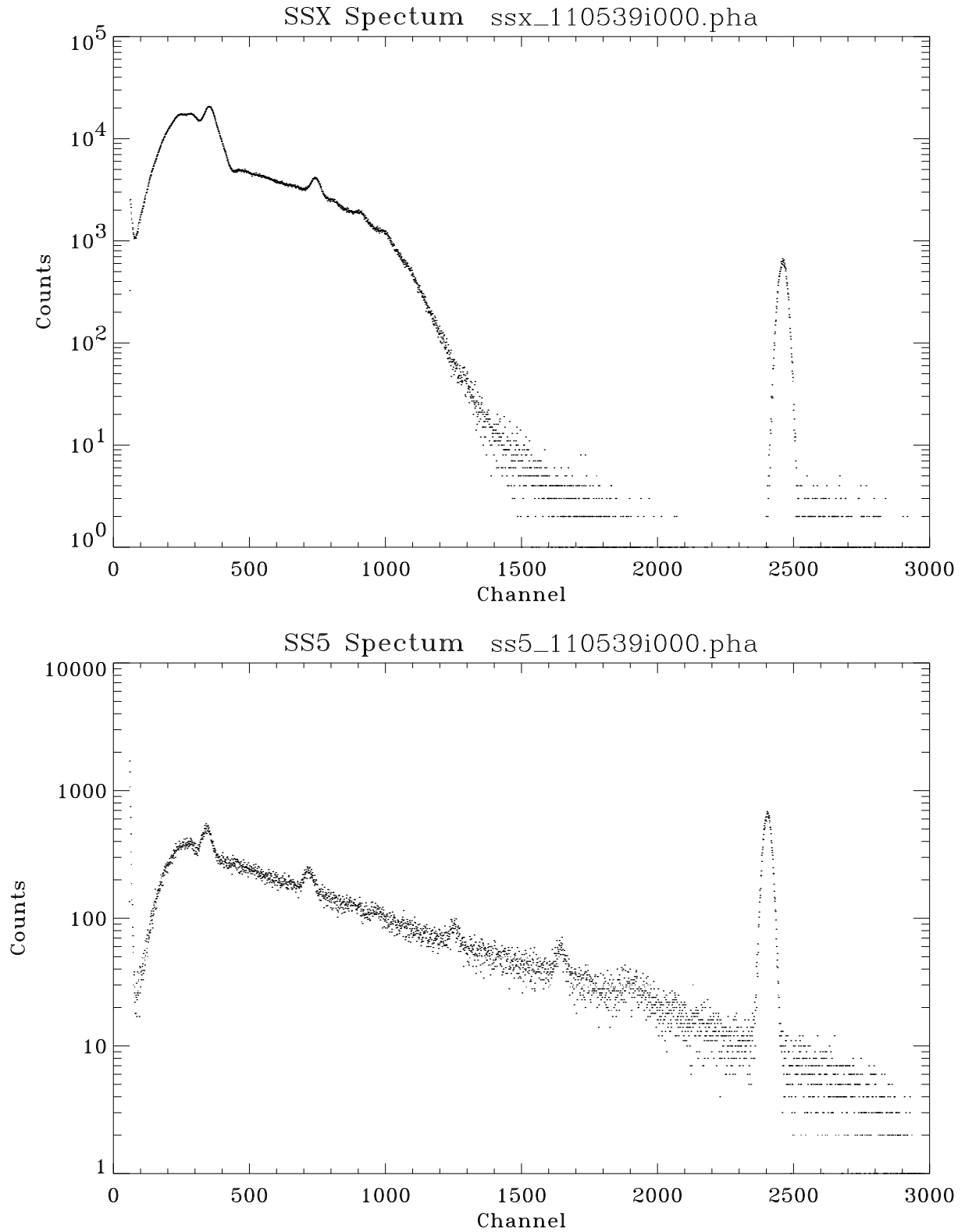


Figure 11.1: C-continuum SSX (focal plane) and SS5 (beam normalization) spectra: Shell 1; Date: 970130; TRW ID: E-IXS-MC-15.001; Run ID: 110539; Aperture: 2 mm; Integration time: 1000 seconds. The Gaussian-like peak at around channels 2400–2500 is due to the electronic pulser.

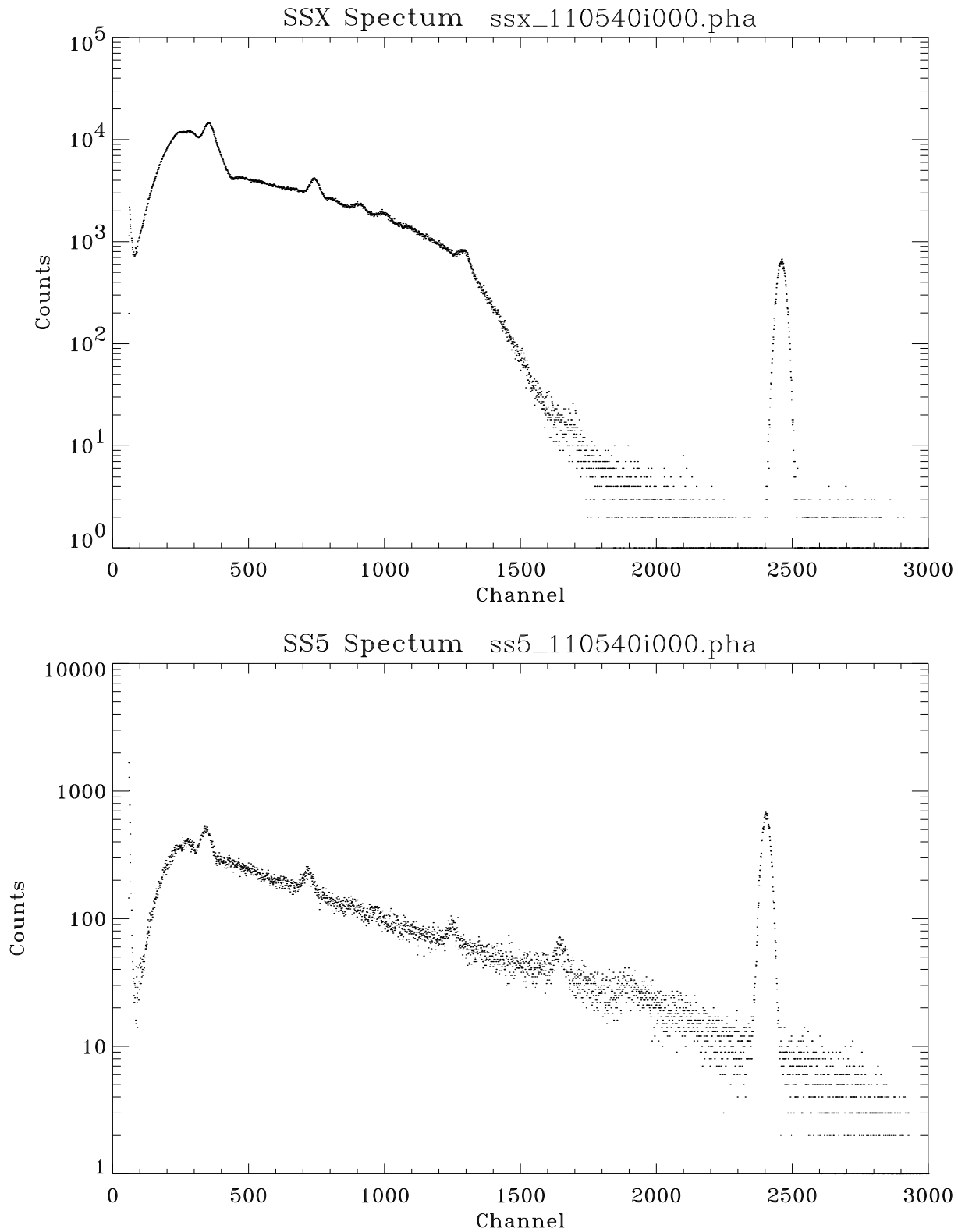


Figure 11.2: C-continuum SSX and SS5 spectra: Shell 3; Date: 970130; TRW ID: E-IXS-MC-15.002; Run ID: 110540; Aperture: 2 mm; Integration time: 1000 seconds.

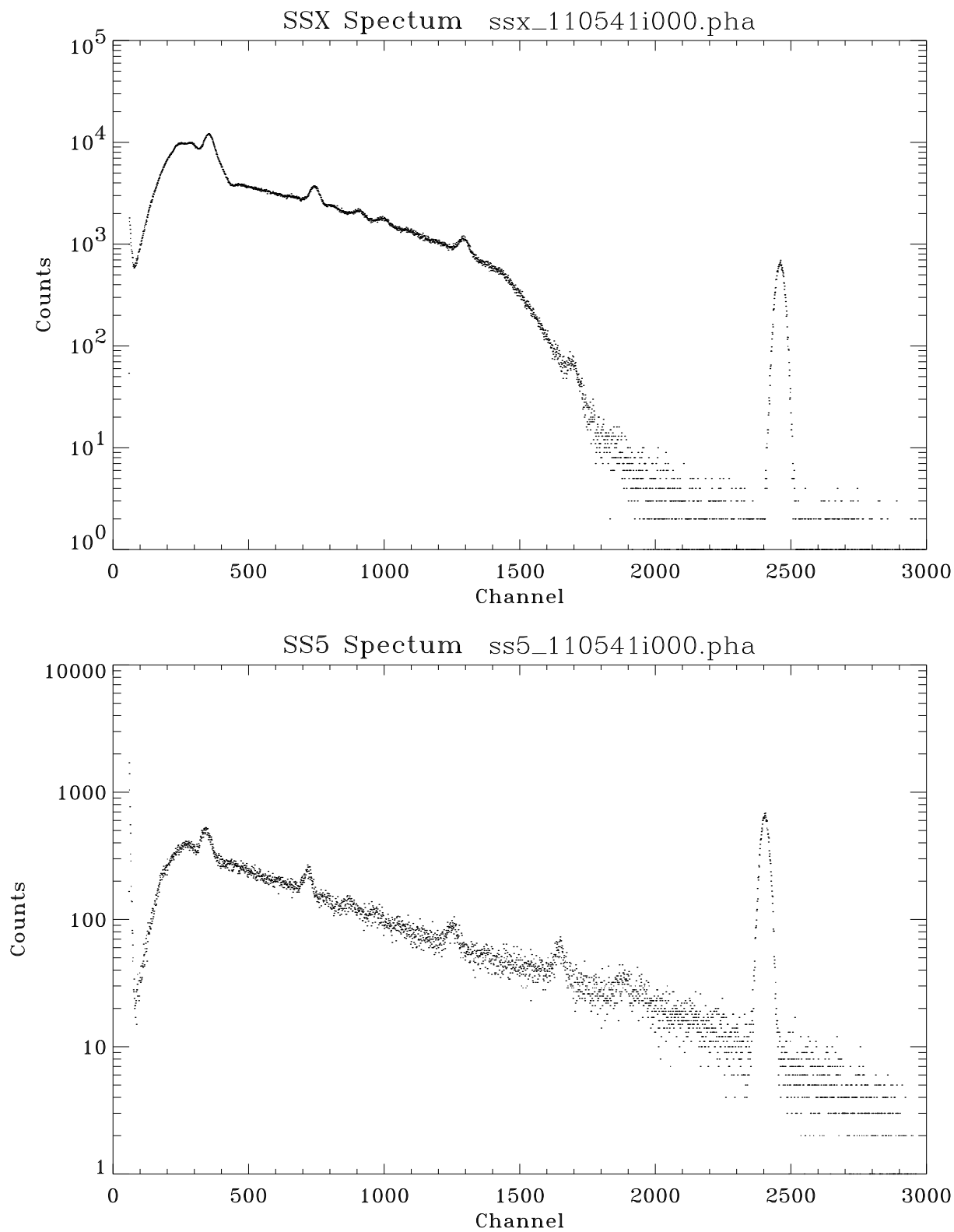


Figure 11.3: C-continuum SSX and SS5 spectra: Shell 4; Date: 970130; TRW ID: E-IXS-MC-15.003; Run ID: 110541; Aperture: 2 mm; Integration time: 1000 seconds.

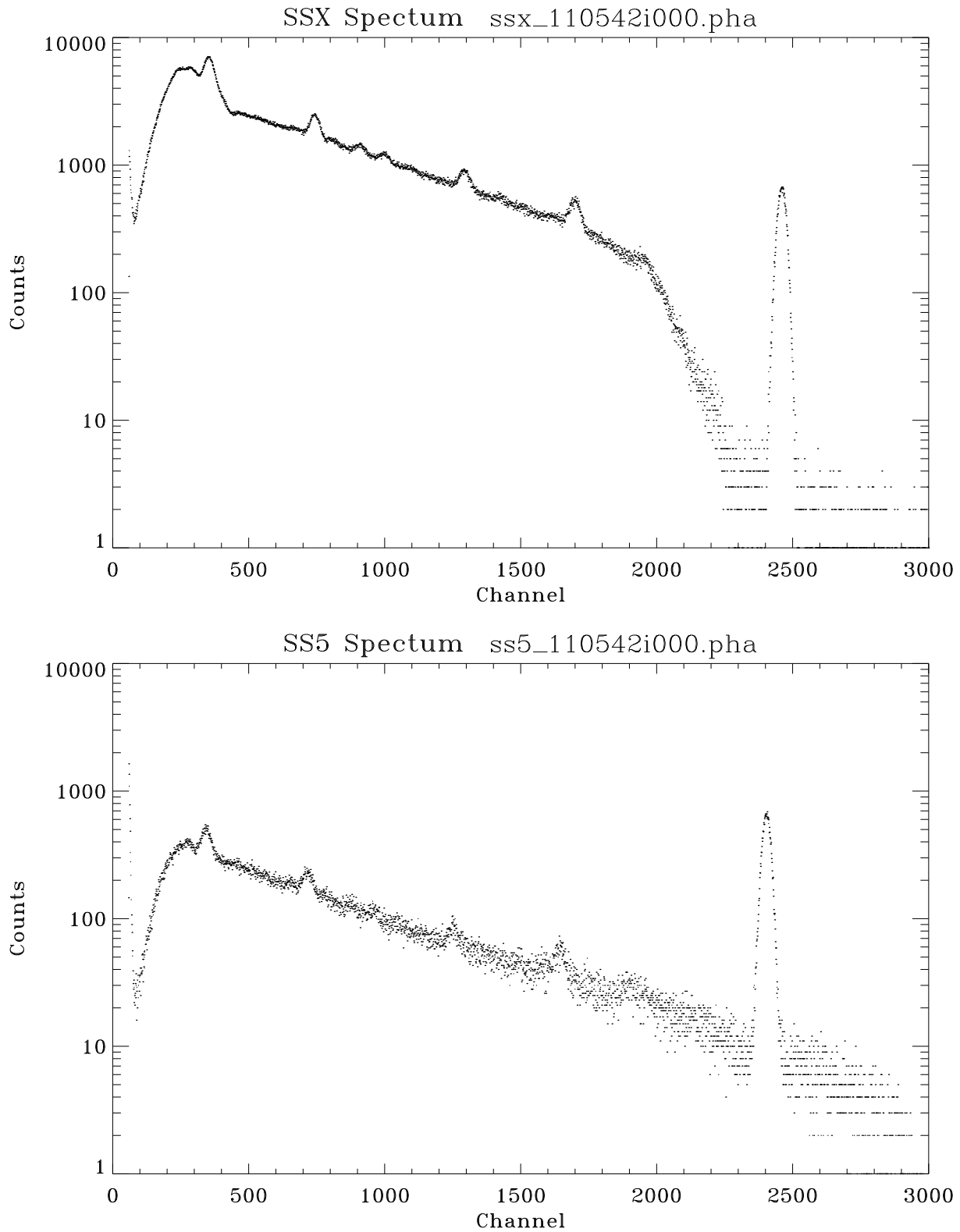


Figure 11.4: C-continuum SSX and SS5 spectra: Shell 6; Date: 970130; TRW ID: E-IXS-MC-15.004; Run ID: 110542; Aperture: 2 mm; Integration time: 1000 seconds.

Table 11.2: HRMA Off-axis Effective Area Measurements  
 Date: 970131      Source: C-continuum      Detector: SSD

TRW ID	Run ID	Shell	Aper ( $\mu\text{m}$ )	Int (sec)	Pitch (arcmin)	Yaw (arcmin)	Off-axis (arcmin)
E-IXS-EE-5.001	110718	HRMA	200	300	-3.53553	3.53553	5
E-IXS-EE-5.001	110719	HRMA	500	300	-3.53553	3.53553	5
E-IXS-EE-5.001	110720	HRMA	500	300	-3.53553	3.53553	5
E-IXS-EE-5.001	110721	HRMA	2000	300	-3.53553	3.53553	5
E-IXS-EE-5.001	110723	HRMA	100	300	-3.53553	3.53553	5
E-IXS-EE-5.001	110725	HRMA	70	300	-3.53553	3.53553	5
E-IXS-EE-5.001	110727	HRMA	50	300	-3.53553	3.53553	5
E-IXS-EE-5.001	110732	HRMA	40	300	-3.53553	3.53553	5
E-IXS-EE-5.004	110733	HRMA	500	300	0	-10	10
E-IXS-EE-5.004	110734	HRMA	2000	300	0	-10	10
E-IXS-EE-5.004	110736	HRMA	200	300	0	-10	10
E-IXS-EE-5.004	110738	HRMA	100	300	0	-10	10
E-IXS-EE-5.004	110740	HRMA	70	300	0	-10	10
E-IXS-EE-5.004	110742	HRMA	50	300	0	-10	10
E-IXS-EE-5.004	110745	HRMA	40	300	0	-10	10
E-IXS-EE-5.005	110749	HRMA	2000	300	-10.6066	10.6066	15
E-IXS-EE-5.005	110751	HRMA	500	300	-10.6066	10.6066	15
E-IXS-EE-5.005	110754	HRMA	200	300	-10.6066	10.6066	15
E-IXS-EE-5.005	110756	HRMA	100	300	-10.6066	10.6066	15
E-IXS-EE-5.005	110759	HRMA	70	300	-10.6066	10.6066	15
E-IXS-EE-5.007	110760	HRMA	2000	300	-14.1421	14.1421	20
E-IXS-EE-5.007	110761	HRMA	500	300	-14.1421	14.1421	20
E-IXS-EE-5.007	110764	HRMA	200	300	-14.1421	14.1421	20
E-IXS-EE-5.009	110766	HRMA	2000	300	-17.6777	17.6777	25
E-IXS-EE-5.010	110768	HRMA	2000	300	-21.2132	21.2132	30

photons has energy below 2 keV, corresponding to a pre-amplifier output signal of 4 mV. Thus each spectrum needs to be corrected for pileups of any photon with a low energy ( $< 2$  keV) photon. Since three or more photon pileups are extremely rare events and their effect is negligible, we only consider two photon pileups.

Figures 11.5–11.8 show the pulser spectra of both `ssd_x` (top panels) and `ssd_5` (bottom panels) for the four measurements. In the `ssd_x` pulser spectra for shell 1 and 3 (Figures 11.5 and 11.6), the pulser pileups are clearly shown to the right of the pulser peak. In the `ssd_x` pulser spectra for shell 4 and 6 (Figures 11.7 and 11.8), the pulser pileups are mixed with the continuum pileups to the right of the pulser peak. There is no direct continuum spectrum above channel  $\sim 2240$  ( $\sim 11$  keV) in `ssd_x` since the HRMA has null reflectivity above  $\sim 11$  keV. In the `ssd_5` pulser spectra, the continuum dominates the right side of the pulser peak; the pileup effects are very small since they are proportional to the counting rate. The total continuum counting rates in `ssd_5` are 1–2 orders of magnitude lower than that of `ssd_x` (see Figures 11.1–11.4).

We use the `ssd_x` pulser spectra for shell 1 and 3 (Run ID 110539 and 110540), where the pulser

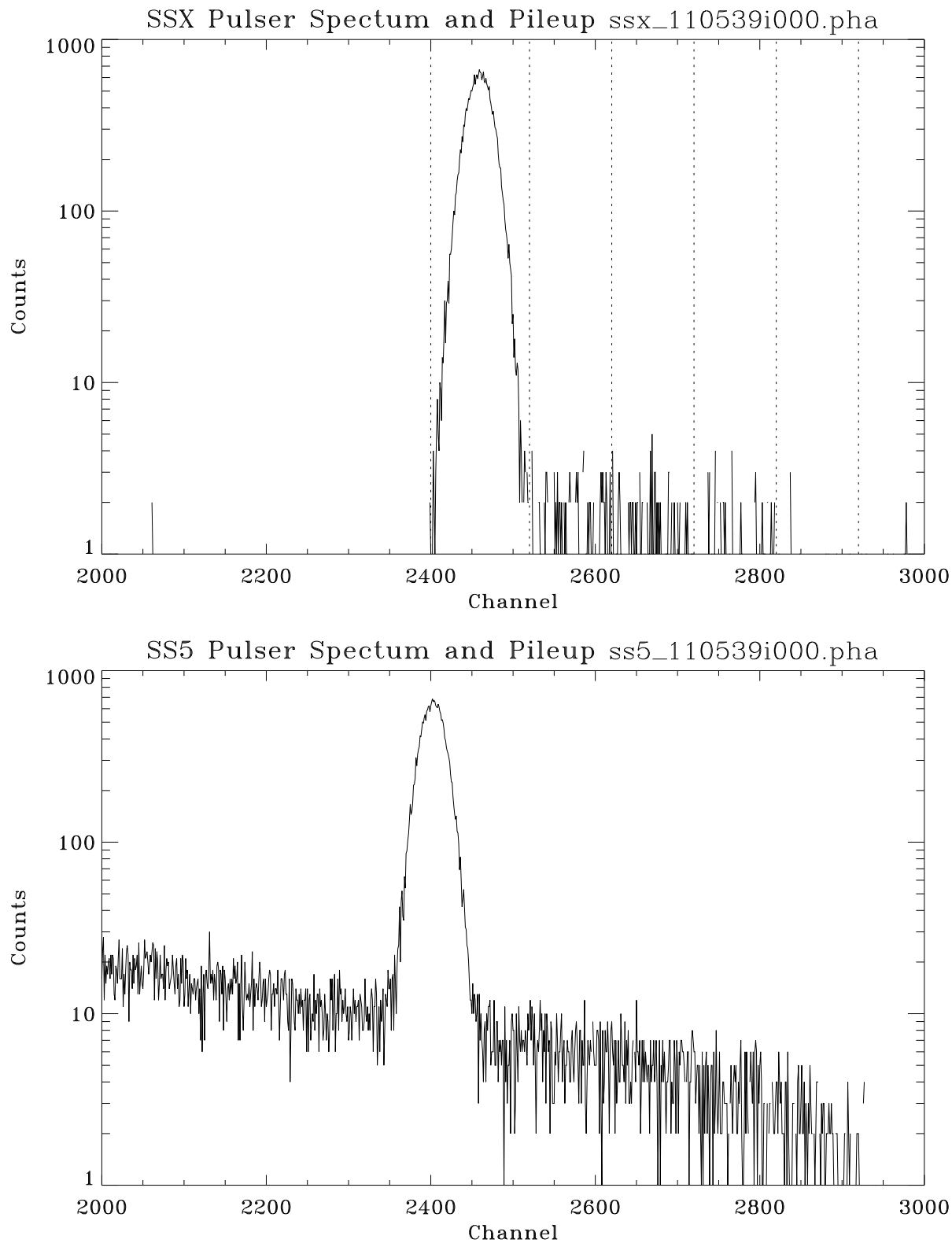


Figure 11.5: SSX and SS5 pulser spectra: Shell 1; Run ID: 110539. Counts to the right of the SSX pulser peak are the pileups from the pulser and low energy photons. Dotted vertical lines in the upper panel indicate the pulser region and four pileup bands.

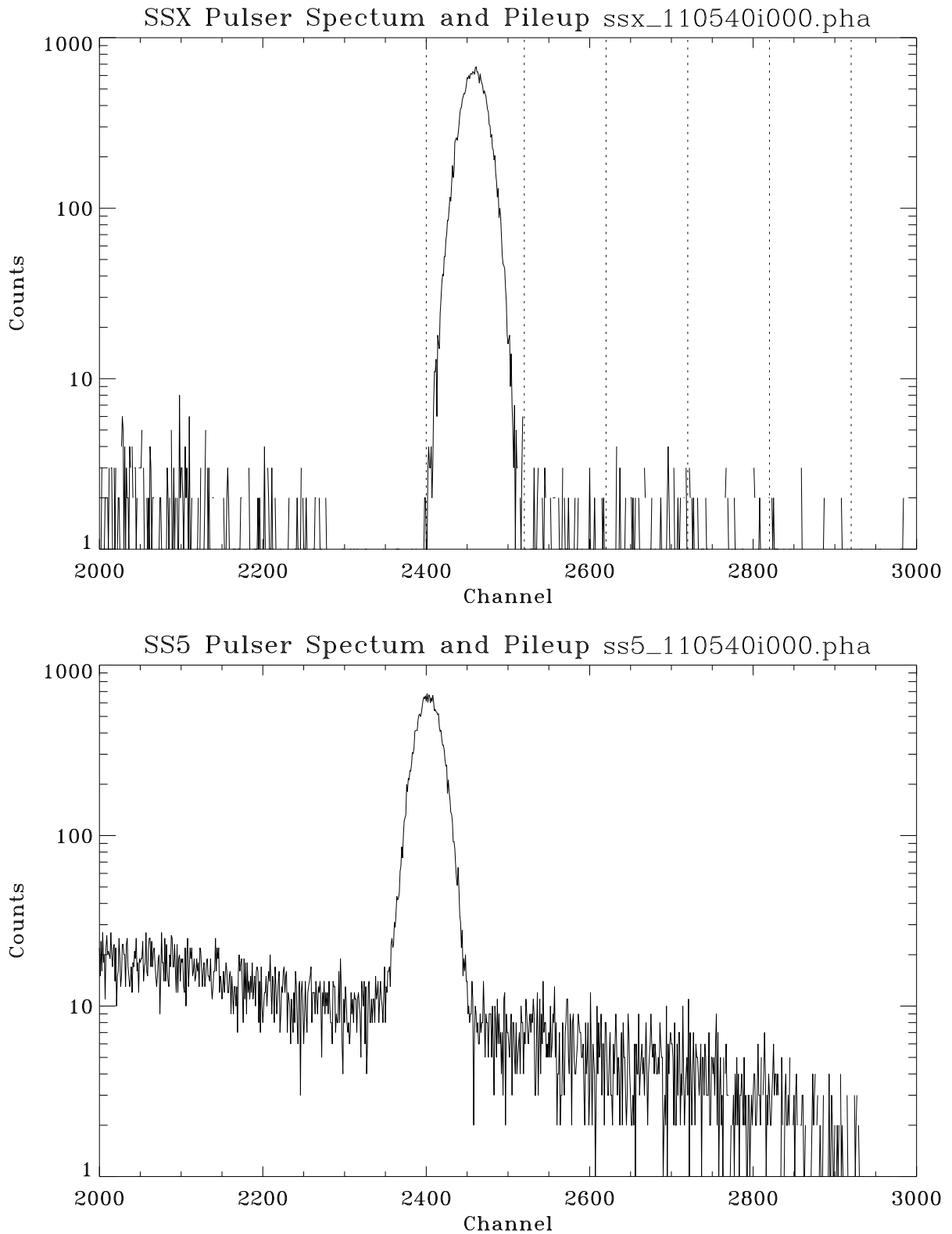


Figure 11.6: SSX and SS5 pulser spectra: Shell 3; Run ID: 110540. Counts to the right of the SSX pulser peak are the pileups from the pulser and low energy photons. Dotted vertical lines in the upper panel indicate the pulser region and four pileup bands.

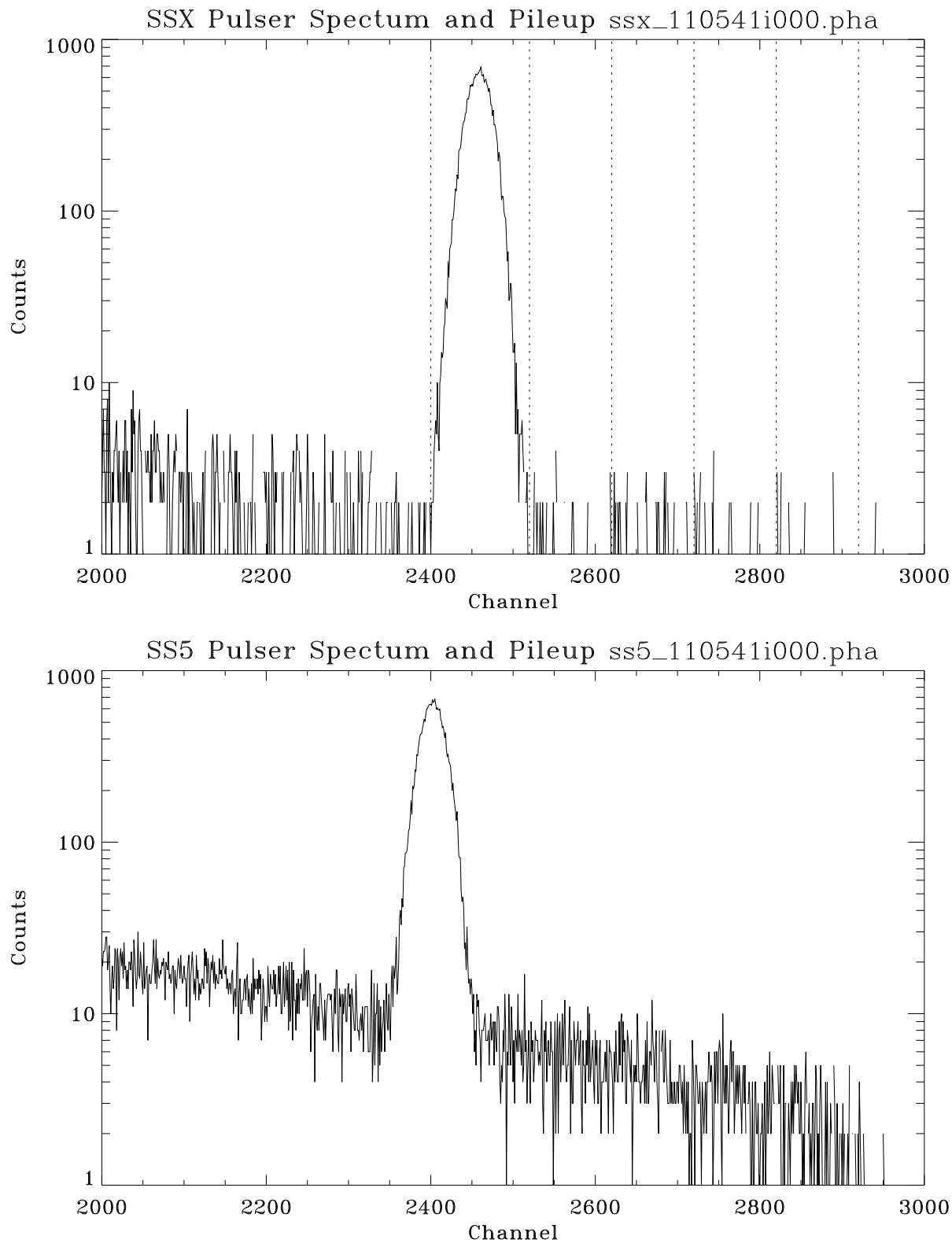


Figure 11.7: SSX and SS5 pulser spectra: Shell 4; Run ID: 110541. Counts to the right of the SSX pulser peak are mainly due to pileups from the pulser, a small amount are due to pileups from the continuum.

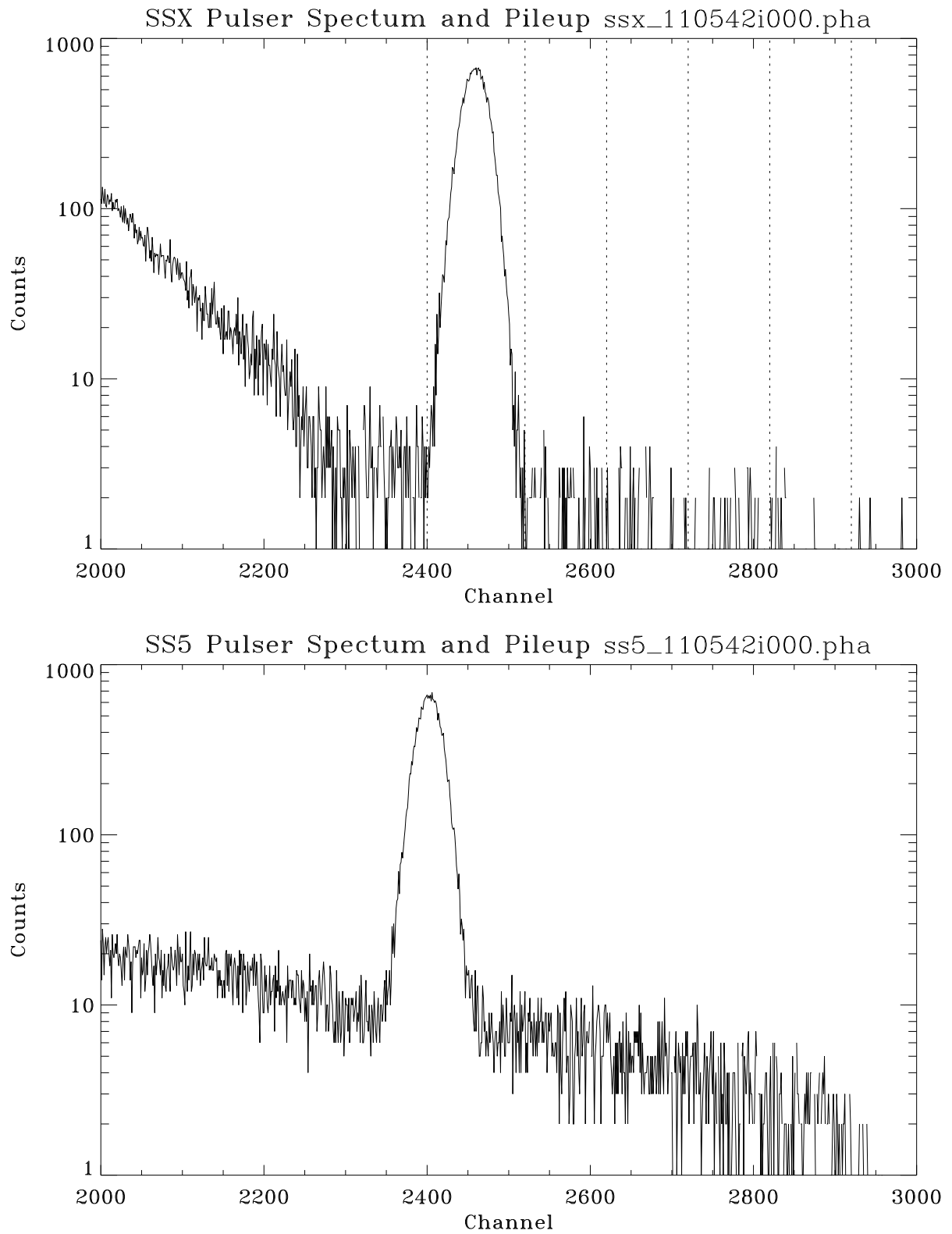


Figure 11.8: SSX and SS5 pulser spectra: Shell 6; Run ID: 110542. Counts to the right of the SSX pulser peak are mixtures of the pulser pileups and the continuum pileups.

pileup effects are clear and not mixed with the continuum pileups, to establish an empirical model for the pileup correction. In *ssd\_x* pulser spectra shown in Figures 11.5–11.8, there are six vertical dotted lines dividing the spectra into 5 bands. The first one on the left covers the pulser peak. The other four bands, with 100 channels per band, cover the pileup region. Since  $2 \text{ keV} \approx 400$  channels, counts in these regions are pileups of low energy photons ( $< 2 \text{ keV}$ ) with the pulser. Since the pileups are proportional to counting rate of photons  $< 2 \text{ keV}$ , we define a pileup rate as the pulser pileup fraction (pulser pileup counts divided by the total pulser counts) divided by the counting rate within channels 0–400. Both *ssd\_x* spectra give, as it should be, about the same results: for the four 100-channel windows after the pulser, the pileup rates are  $1.2 \times 10^{-6} \text{ sec/count}$  in channels 1–100,  $1.0 \times 10^{-6} \text{ sec/count}$  in channels 101–200,  $0.7 \times 10^{-6} \text{ sec/count}$  in channels 201–300, and  $0.3 \times 10^{-6} \text{ sec/count}$  in channels 301–400. Notice that here the unit for pileup rate is "second/count". When calculating the pileup fraction, we need to multiply these pileup rates by the counting rate within channels 0–400. For example, for *ssd\_x* spectrum 110539,  $\text{CR}(0-400) = 4448 \text{ counts/second}$ , pileup fractions are 0.005337, 0.004448, 0.003114, 0.001334 in the four windows; for *ssd\_x* spectrum 110542,  $\text{CR}(0-400) = 1415 \text{ counts/second}$ , pileup fractions are 0.001698, 0.001415, 0.000990, 0.000424. Meantime, for all the *ssd.5* spectra,  $\text{CR}(0-400) = 100$ , so the pileup fractions are 0.000120, 0.000100, 0.000070, 0.000030, which are negligible.

In each channel of the raw spectra, there are real events at that energy plus some pileup events which come from lower channels. Meanwhile, some of the real events at that energy were piled up to higher channels following the above empirical model. To make the pileup correction, we need to subtract pileup fractions from each channel and put them back where they belong, and remember each pileup photon came from two lower energy photons. These were done as follows: first multiply the  $\text{CR}(0-400)$  by the pileup rates given above to obtain the pileup fractions for that spectrum; for each channel  $N$ , we add the pileup fractions of channel  $N$  back to channel  $N$ , subtract one percent of pileup fractions of channel  $N$  from each channel  $N + X$  ( $X = 1-400$ ), and also add the same number to channel  $X$ ; then just step along for the entire spectrum.

Figures 11.9–11.12 show the *ssd\_x* pileup corrections. In the top panels, the dots are the raw data, the solid line show the pileup corrected data. It is seen that when the spectra have sharp declines, the pileup corrections make the spectra even lower. The bottom panels show the ratio of the pileup corrected data vs. the raw data.

Figures 11.13–11.16 show the *ssd.5* pileup corrections. Since the counting rates are very low, the pileup effects are negligible. The ratios between the pileup corrected data vs. the raw data are nearly unity between channel 400 and the pulser peak (notice the vertical scale difference comparing to the bottom panels of Figures 11.9–11.12).

The dashed vertical lines in the top panels of Figures 11.9–11.16 indicate the position of six selected X-ray characteristic lines to be used to determine the energy scale of the spectra (see §11.5 and §11.11).

After the pileup correction and before reducing the effective area, we need to know the relative quantum efficiency of the two SSD detectors.

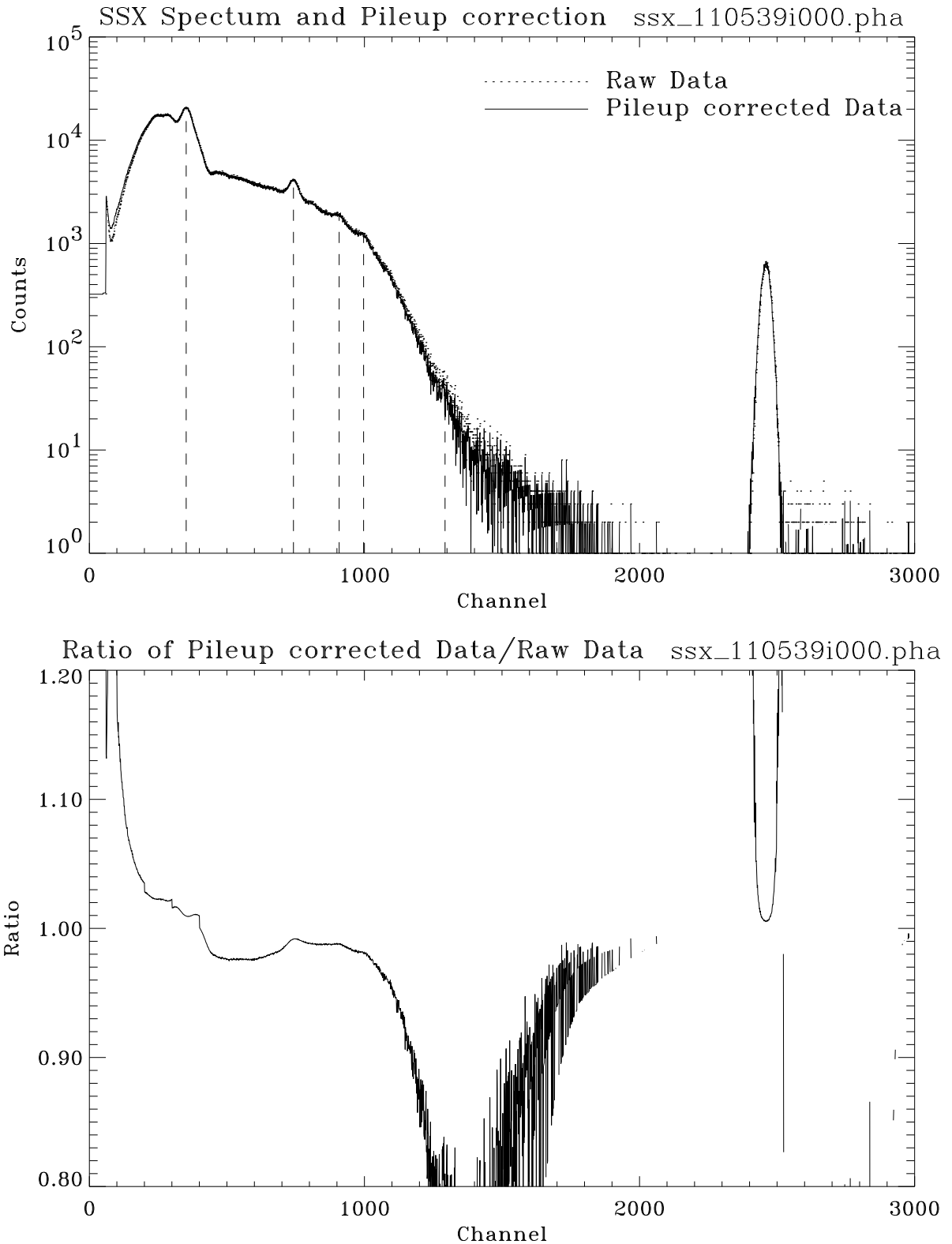


Figure 11.9: SSX spectrum and pileup correction: Shell 1; Run ID: 110539. Upper panel shows the raw data and pileup corrected data. Dashed vertical lines indicate the X-ray lines to be used to calibrate the energy scale. Lower panel shows the ratio of pileup corrected data to the raw data.

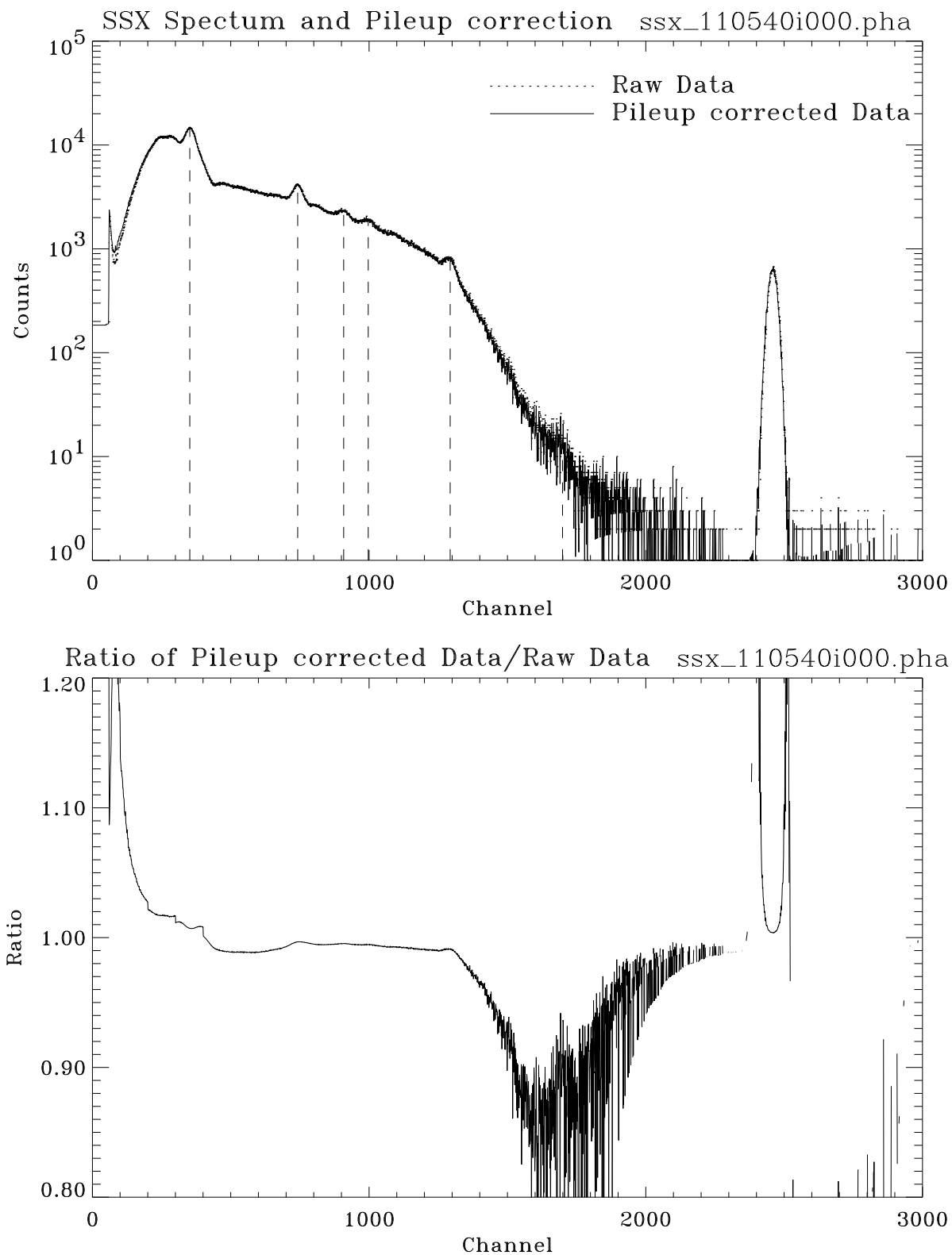


Figure 11.10: SSX spectrum and pileup correction: Shell 3; Run ID: 110540. Upper panel shows the raw data and pileup corrected data. Dashed vertical lines indicate the X-ray lines to be used to calibrate the energy scale. Lower panel shows the ratio of pileup corrected data to the raw data.

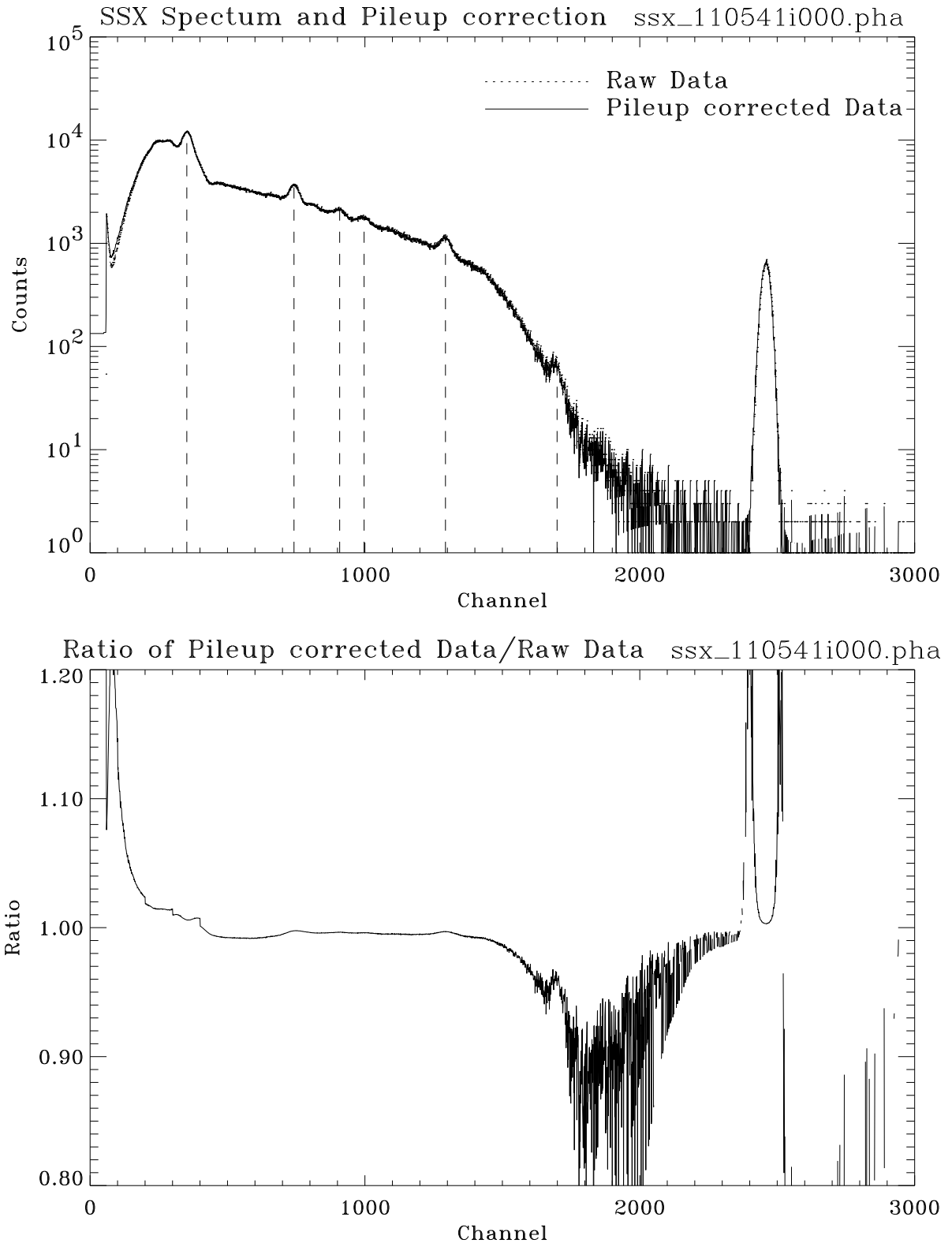


Figure 11.11: SSX spectrum and pileup correction: Shell 4; Run ID: 110541. Upper panel shows the raw data and pileup corrected data. Dashed vertical lines indicate the X-ray lines to be used to calibrate the energy scale. Lower panel shows the ratio of pileup corrected data to the raw data.

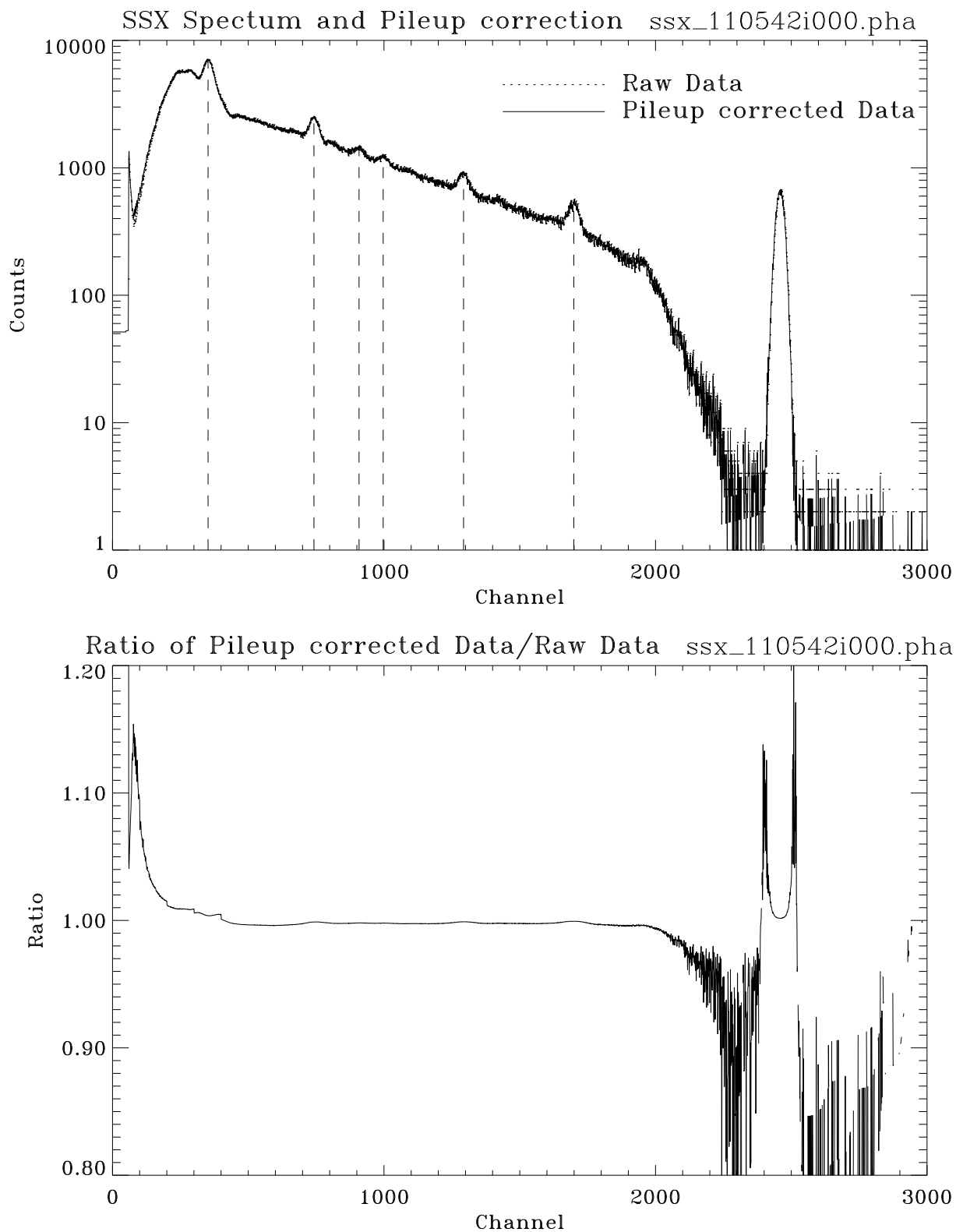


Figure 11.12: SSX spectrum and pileup correction: Shell 6; Run ID: 110542. Upper panel shows the raw data and pileup corrected data. Dashed vertical lines indicate the X-ray lines to be used to calibrate the energy scale. Lower panel shows the ratio of pileup corrected data to the raw data.

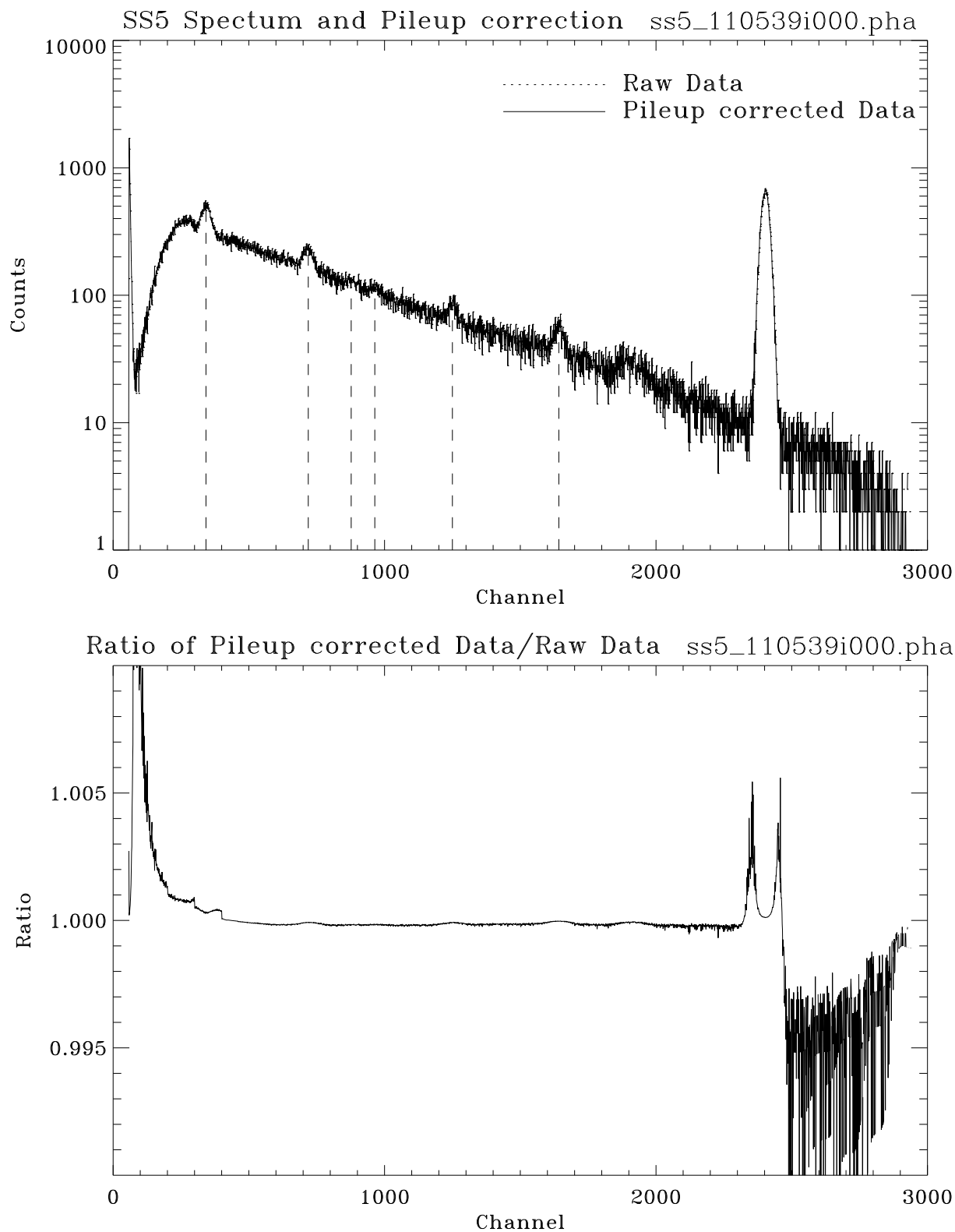


Figure 11.13: SS5 spectrum and pileup correction: Shell 1; Run ID: 110539. Upper panel shows the raw data and pileup corrected data. Dashed vertical lines indicate the X-ray lines to be used to calibrate the energy scale. Lower panel shows the ratio of pileup corrected data to the raw data.

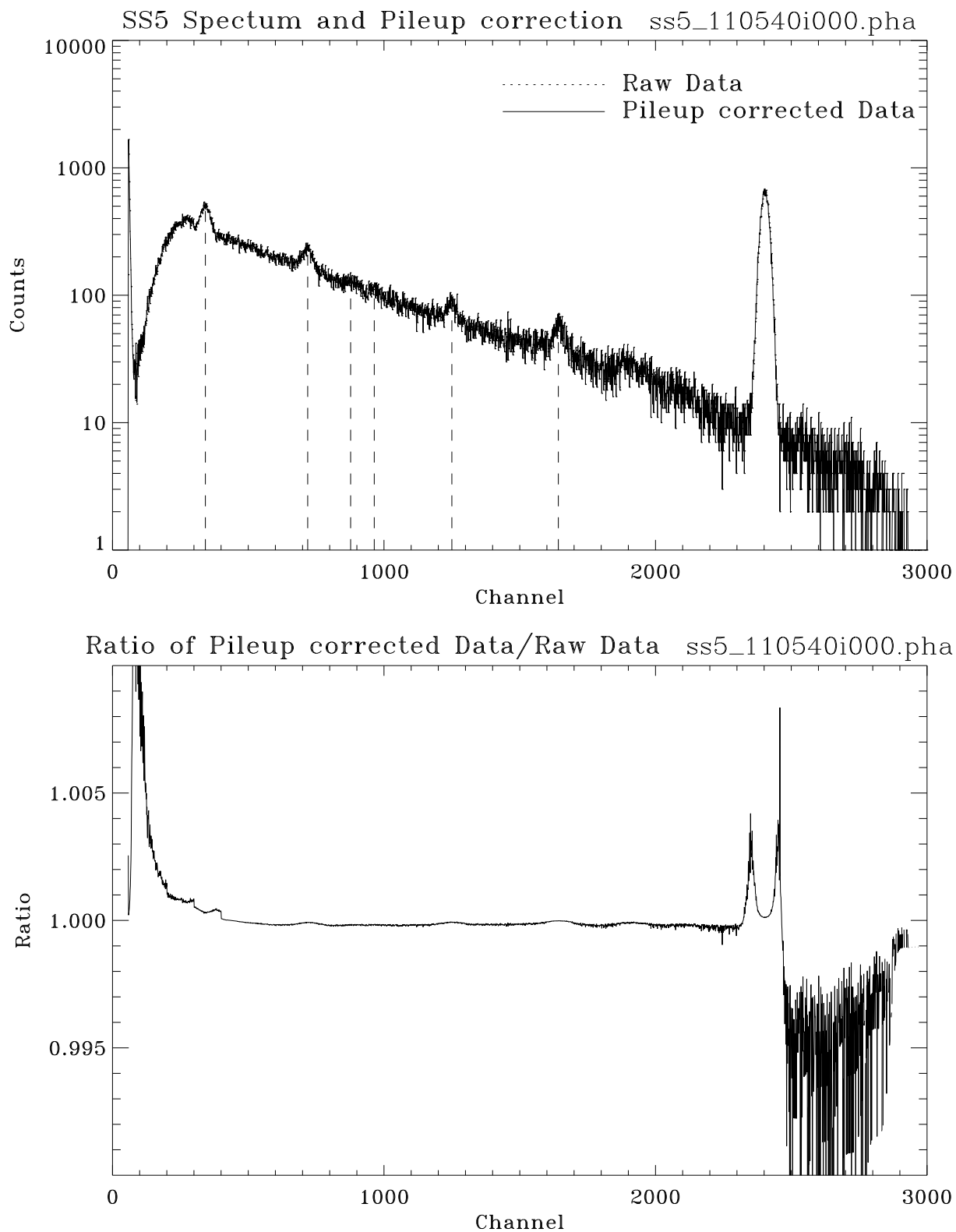


Figure 11.14: SS5 spectrum and pileup correction: Shell 3; Run ID: 110540. Upper panel shows the raw data and pileup corrected data. Dashed vertical lines indicate the X-ray lines to be used to calibrate the energy scale. Lower panel shows the ratio of pileup corrected data to the raw data.

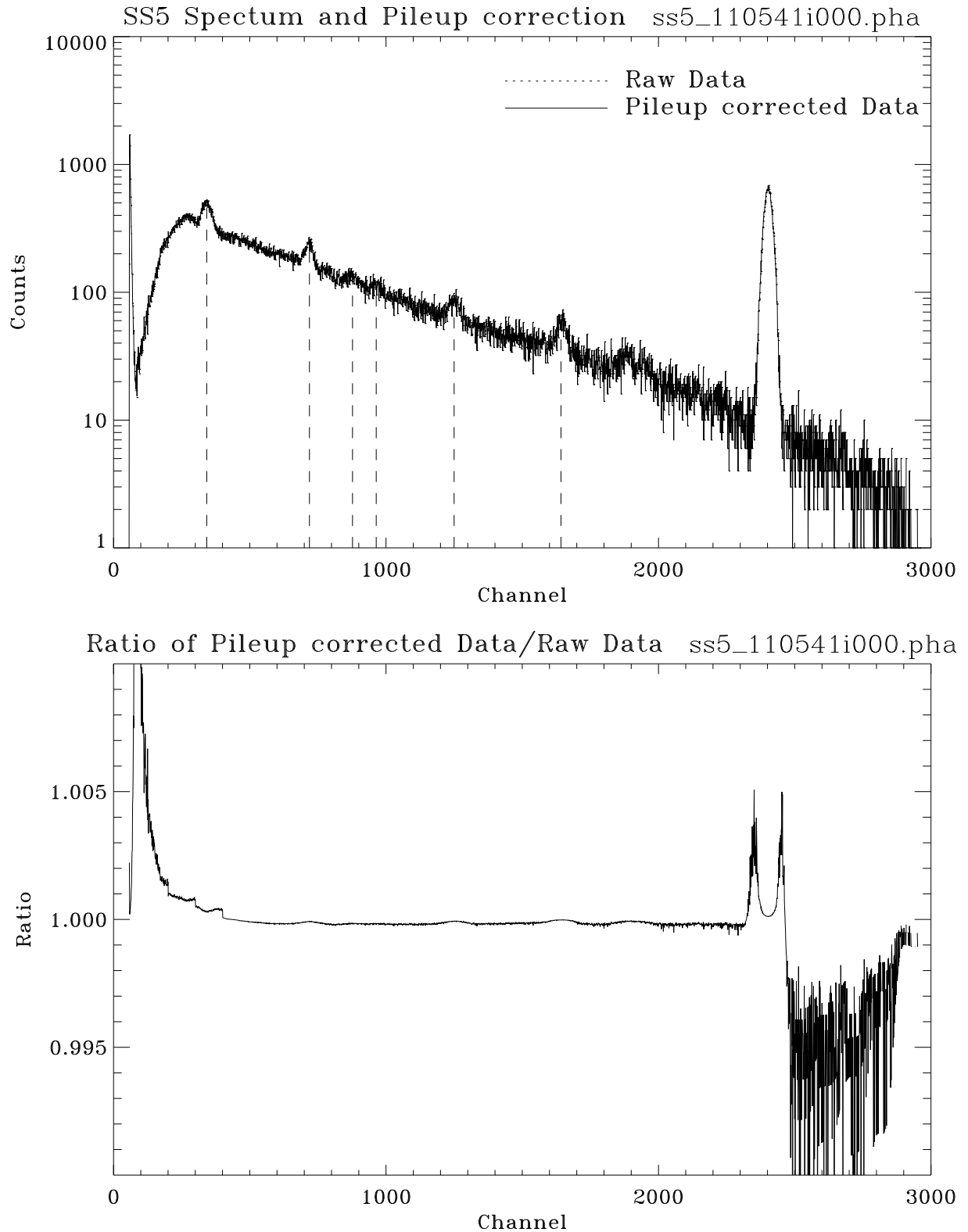


Figure 11.15: SS5 spectrum and pileup correction: Shell 4; Run ID: 110541. Upper panel shows the raw data and pileup corrected data. Dashed vertical lines indicate the X-ray lines to be used to calibrate the energy scale. Lower panel shows the ratio of pileup corrected data to the raw data.

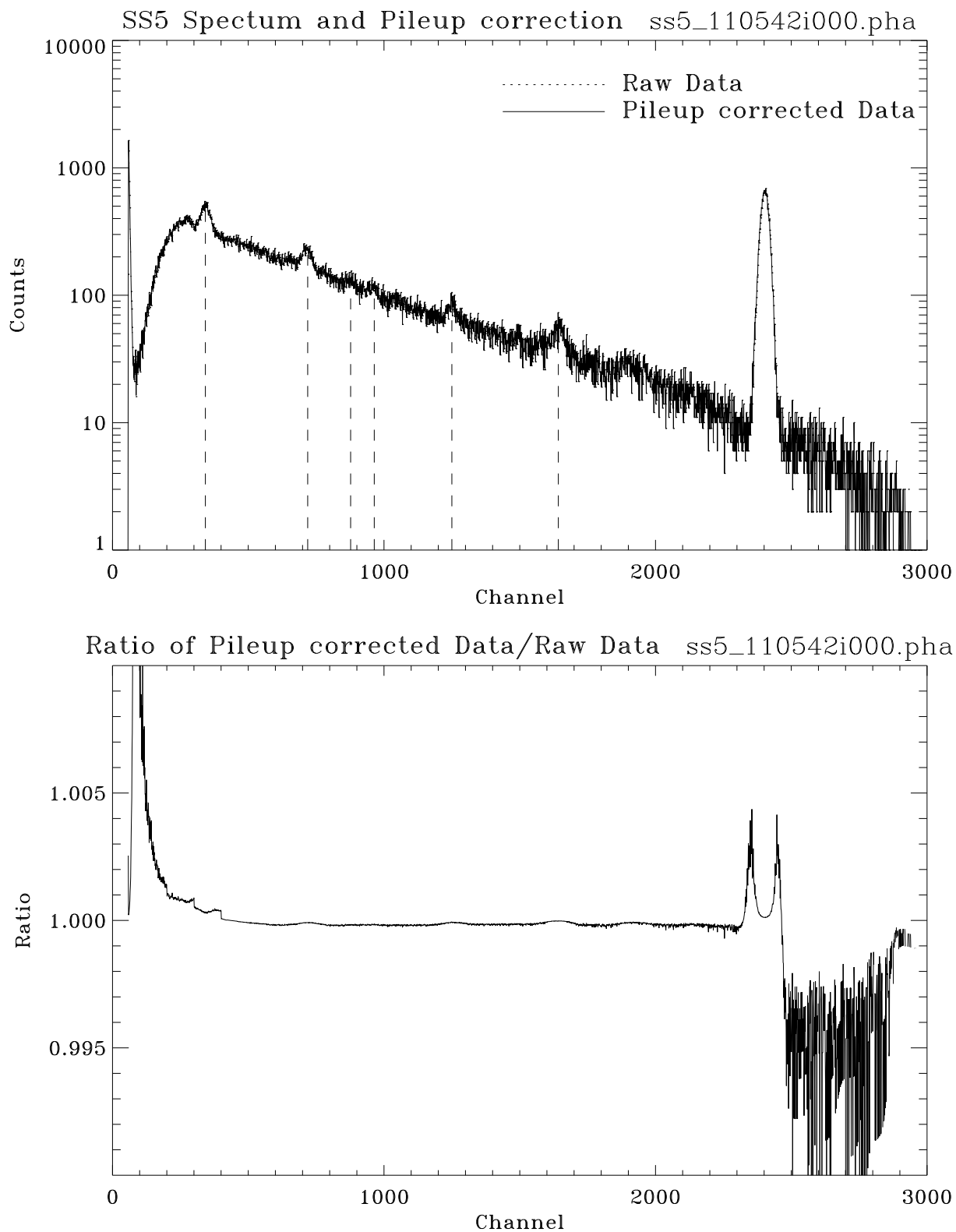


Figure 11.16: SS5 spectrum and pileup correction: Shell 6; Run ID: 110542. Upper panel shows the raw data and pileup corrected data. Dashed vertical lines indicate the X-ray lines to be used to calibrate the energy scale. Lower panel shows the ratio of pileup corrected data to the raw data.

## 11.4 SSD Flat Field Test

In order to obtain the effective area by dividing the spectra of `ssd_x` and `ssd_5`, we need to know the relative Quantum Efficiency (QE) of the two SSDs as a function of energy. The SSD QE was measured as part of the HRMA calibration at both the XRCF and BESSY. This section discusses the SSD QE measurement made at the XRCF, i.e. the SSD C-continuum flat field test.

The C-continuum flat field test was done in June 1997, when the HRMA had been removed from the testing chamber and shipped to TRW. The two SSDs were swapped, `ssd_x` was placed at the `ssd_5` location in building 500 and `ssd_5` was placed at the focal plane.

If the X-ray beam were uniform (this is not exactly the case – see §11.7), the X-ray flux at the two SSDs should be proportional to inverse square of their distance to the source. The distance from the source to `ssd_x` was 38.199 m and to `ssd_5` was 537.778 m. The 2 mm aperture was used for the `ssd_x` and 5 mm aperture was used for the `ssd_5` for the flat field test.

Figure 11.17 shows the spectra, with counting rate as a function of spectral channel, obtained with the two SSDs.<sup>1</sup> There are several spectral peaks atop the continuum. The largest peak to the right of each spectrum is the pulser peak, which is used to estimate the pileup correction, as discussed in the previous section, and to calculate the deadtime correction (see §11.6). Other peaks are characteristic X-ray lines due to contaminations to the carbon anode (also seen in Figures 11.1–11.4).

As the counting rates for the flat field test were very low (the `ssd_x` counting rate for the flat field test was about the same as the `ssd_5` counting rate during the effective area measurements, see previous Section. The `ssd_5` counting rate was 200 times lower than that of the `ssd_x` during the flat field test.), so the pileup effect is negligible.

## 11.5 SSD Energy Scale

Using the characteristic X-ray lines atop the continuum spectra, the SSD energy scale can be determined. As shown in Figure 11.17, six strong and single peaked lines were selected to determine the energy scale. Table 11.3 lists these six lines, from left to right.

To determine the line centers, a Gaussian profile with a quadratic function base was fitted to each peak. The centers of fitted Gaussian are shown in Figure 11.17 as dashed vertical lines with the peaks. Each SSD energy scale is determined by fitting a linear least square fit of the line energies as a function of line centers:

$$Energy = a + b \cdot Channel \quad (11.1)$$

Figure 11.18 shows the energy to channel linear fit for the two SSDs during the flat field test, i.e. Calibration Phase-J. The fitted energy scale parameters,  $a$  and  $b$ , are listed in the Figure. The fits are extremely good, as shown in Figure 11.19, which plots the residuals of the fits.

Using the above energy scales, the SSD spectra are converted from functions of channel to functions of energy and re-binned into equal energy bins. Figure 11.20 shows the C-continuum `ssd_x` and `ssd_5` spectra as functions of energy, in units of counts per second per keV, where all the spectral lines are aligned up.

Since the operating conditions were different during the calibration, the energy scales were not the same in different phases of the calibration. For the SSD effective area measurements in Phase-E, we use the same method to obtain the energy scale.

<sup>1</sup>Notice that the data file for `ssd_x` starts as 'ss5' and vice versa, because the two SSDs were swapped and the data files were named after the location of the detector.

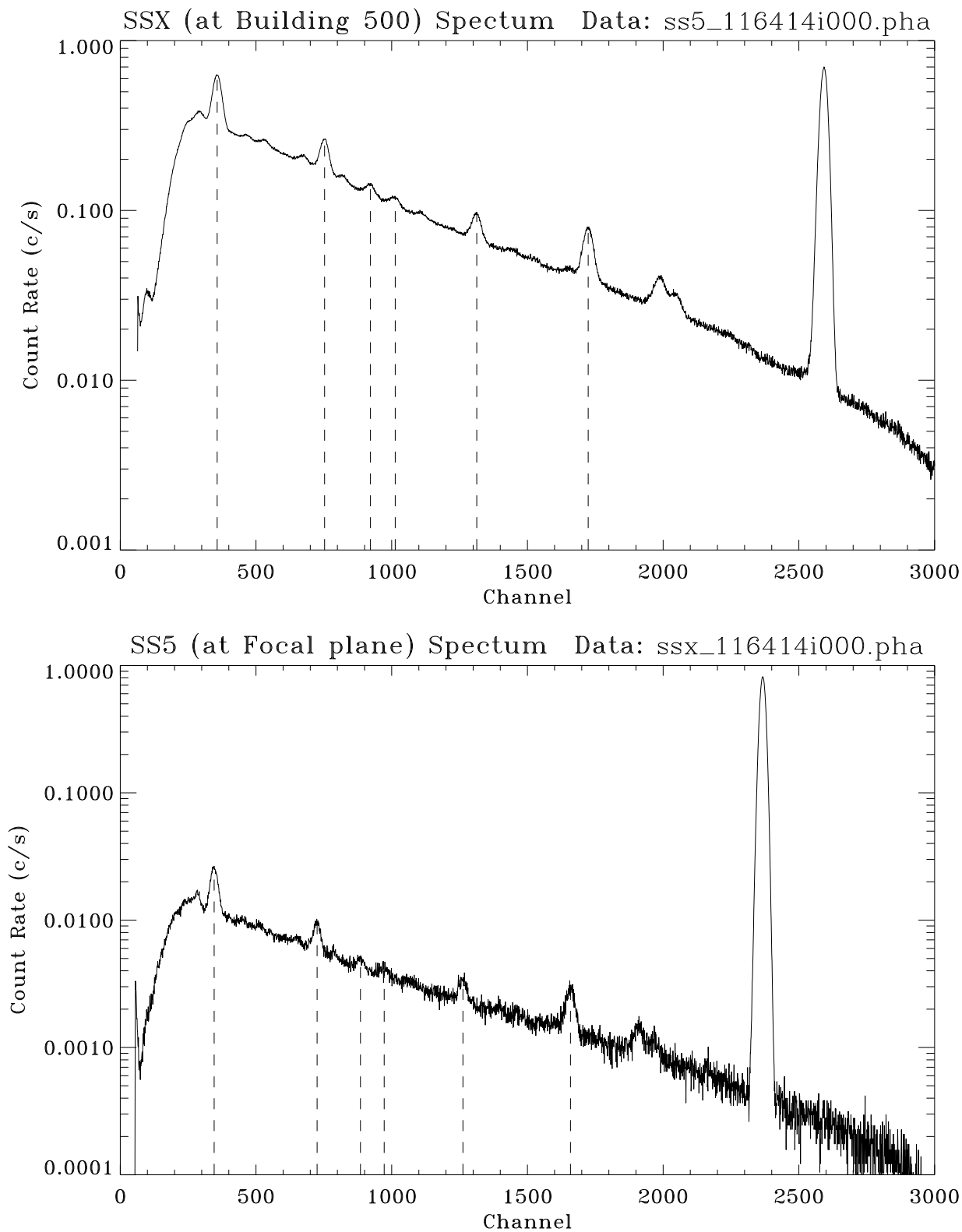


Figure 11.17: C-continuum flat field test SSX and SS5 spectra: Date: 970625; TRW ID: J-BND-BU-2.137; Run ID: 116414; Integration time: 57600 seconds. Dashed vertical lines indicate fitted centers of X-ray characteristic lines atop of the C-continuum spectrum.

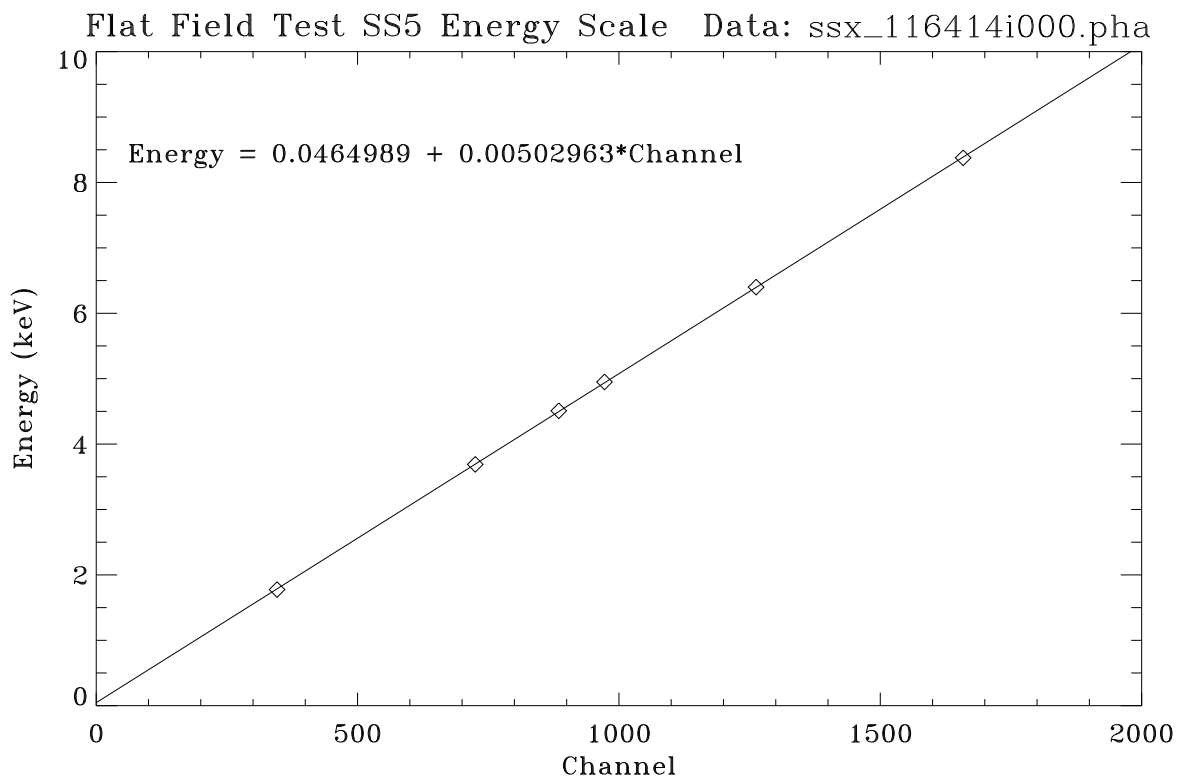
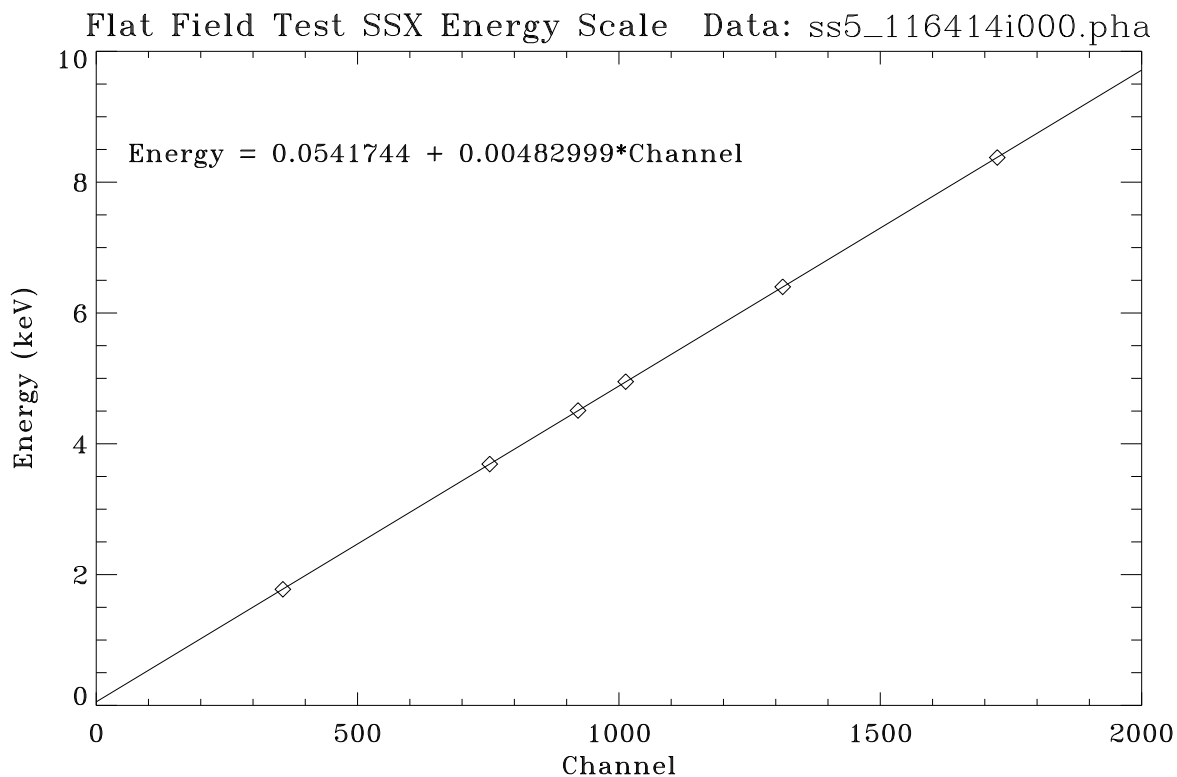


Figure 11.18: SSX and SS5 energy scales for the flat field test (Phase-J), fitted with six X-ray line energies.

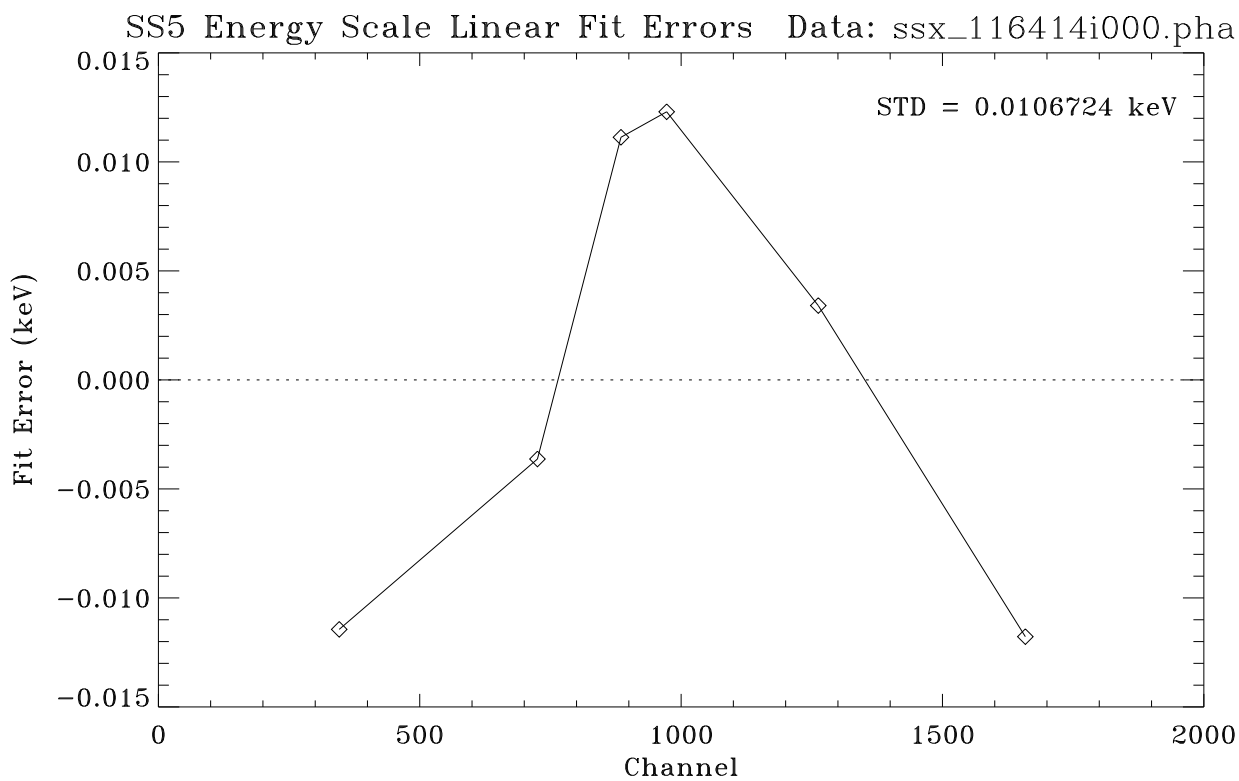
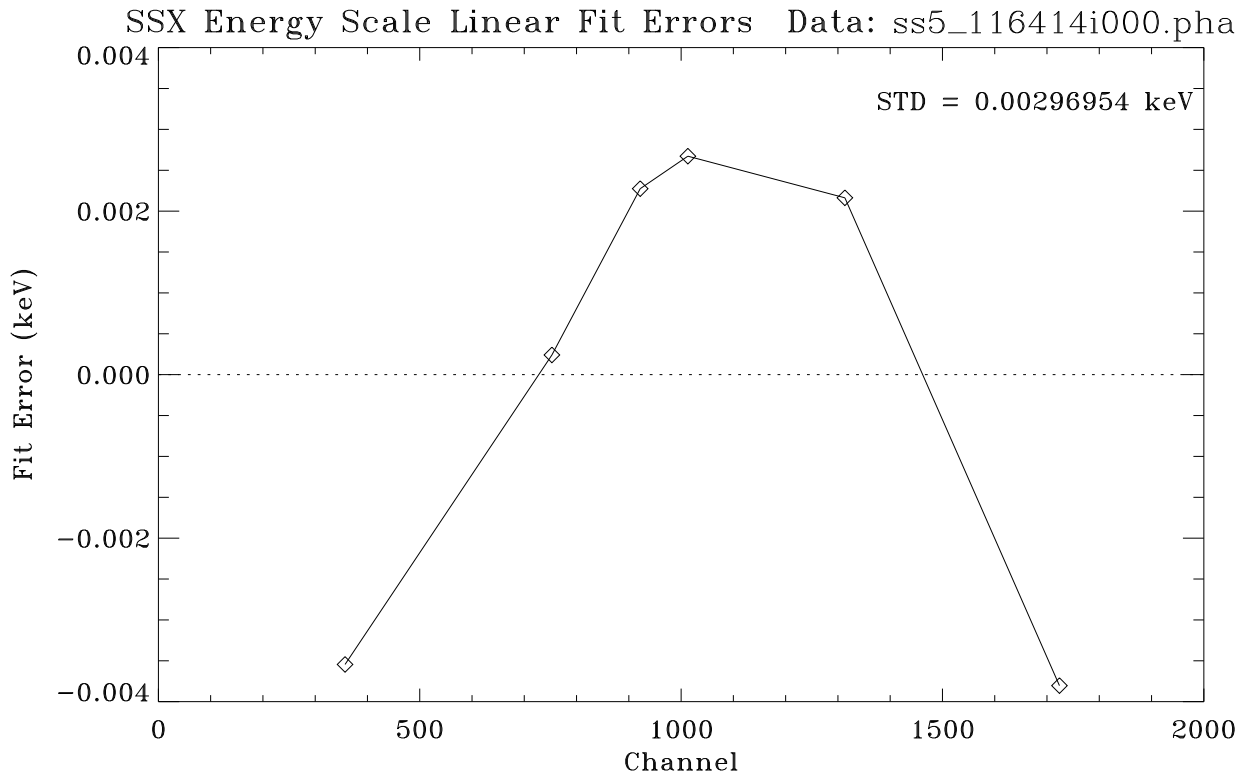


Figure 11.19: SSX and SS5 energy scale linear fit residuals for the flat field test (Phase-J).

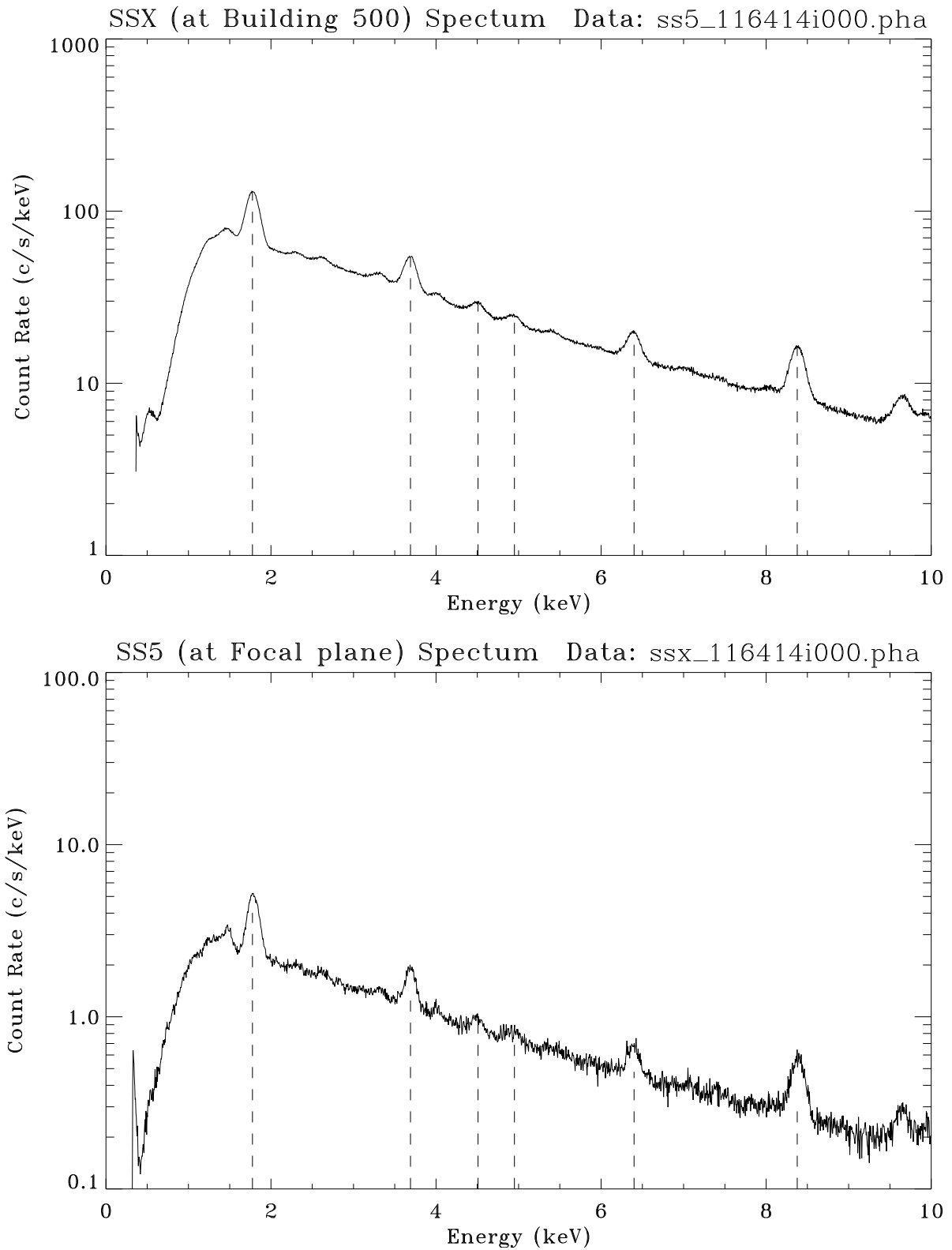


Figure 11.20: C-continuum flat field test SSX and SS5 spectra as functions of energy, using energy scales from Figure 11.18.

Table 11.3: X-ray Lines atop the C-continuum

X-ray Line	Energy
Si-K $\alpha$ , W-M $\alpha$ and W-M $\beta$	1.77525 keV *
Ca-K $\alpha$	3.69048 keV
Ti-K $\alpha$	4.50885 keV
V-K $\alpha$ **	4.94968 keV
Fe-K $\alpha$	6.39951 keV
W-L $\alpha$	8.37680 keV

\* The line center for Si-K $\alpha$ , W-M $\alpha$  and W-M $\beta$  multiplet is weighted by line strength according to the HEG spectrum.

\*\* Another choice for this line is Ti-K $\beta$  (4.93181 keV). We chose V-K $\alpha$  because this line has almost the same intensity as the Ti-K $\alpha$  line, while in the same spectrum all the  $\beta$  lines are about an order of magnitude weaker than their  $\alpha$  counterparts. Also V-K $\alpha$  gives a slightly better linear fit to the energy scale. Had Ti-K $\beta$  been chosen, the result is to lower the energy offset (parameter  $a$  in Eq. 11.1) by 0.003 keV, i.e. to decrease parameter  $a$  in Table 11.4 by 0.003.

We use the pileup corrected `ssd_x` and `ssd_5` spectra (see §11.3) to obtain the energy scale. In Figures 11.9–11.16, the upper panels show the pileup corrected `ssd_x` and `ssd_5` spectra. The SSD energy scale was determined using the six characteristic X-ray lines atop the continuum spectra, indicated by dashed vertical lines and as listed in Table 11.3. First a Gaussian profile with quadratic function was fitted to each peak to determine the line center. The fitted centers for the same line in different spectra of the same SSD differ only by a couple of channels, which is well within the fitted errors. So an averaged center for each line from the four measurements was used to obtain the energy scale. The energy scales of `ssd_x` and `ssd_5` are determined by doing a linear least square fit of the averaged line centers to the line energies.

Figure 11.21 shows the energy to channel linear fit for the two SSDs in Phase-E. The fits are also extremely good, as shown in Figure 11.22, which plots the residuals of the fits.

Same practice was also used to obtain the SSD energy scale in Phase-D. We choose the effective area C-continuum measurements with run IDs 108426, 108450, 108484, and 108500 (TRW IDs D-IXS-EE-1.001,2,3,4), which had integration time of 300 sec and 2 mm apertures. Figure 11.23 shows the energy to channel linear fit for the two SSDs in Phase-D. Figure 11.24 show the residuals of the fits.

Table 11.4 lists the fitted energy scale parameters for the two SSDs in Phase D, E, and J. Notice that the energy scales are slightly different between Phase D and E and quite different for Phase J of the calibration.

Now it seems that we can obtain the relative QE by simply dividing the two spectra and considering the distance and aperture factors. But this can not be done before the deadtime and beam uniformity corrections are carefully evaluated.

## 11.6 SSD Deadtime Correction

In the raw data, the deadtime correction was automatically estimated, using a built-in circuitry and algorithms that follow the Gedcke-Hale formalism (Jenkins et al., 1981), and entered in the pha file header for each spectrum. However, for the SSDs, Gedcke-Hale formalism does not provide an

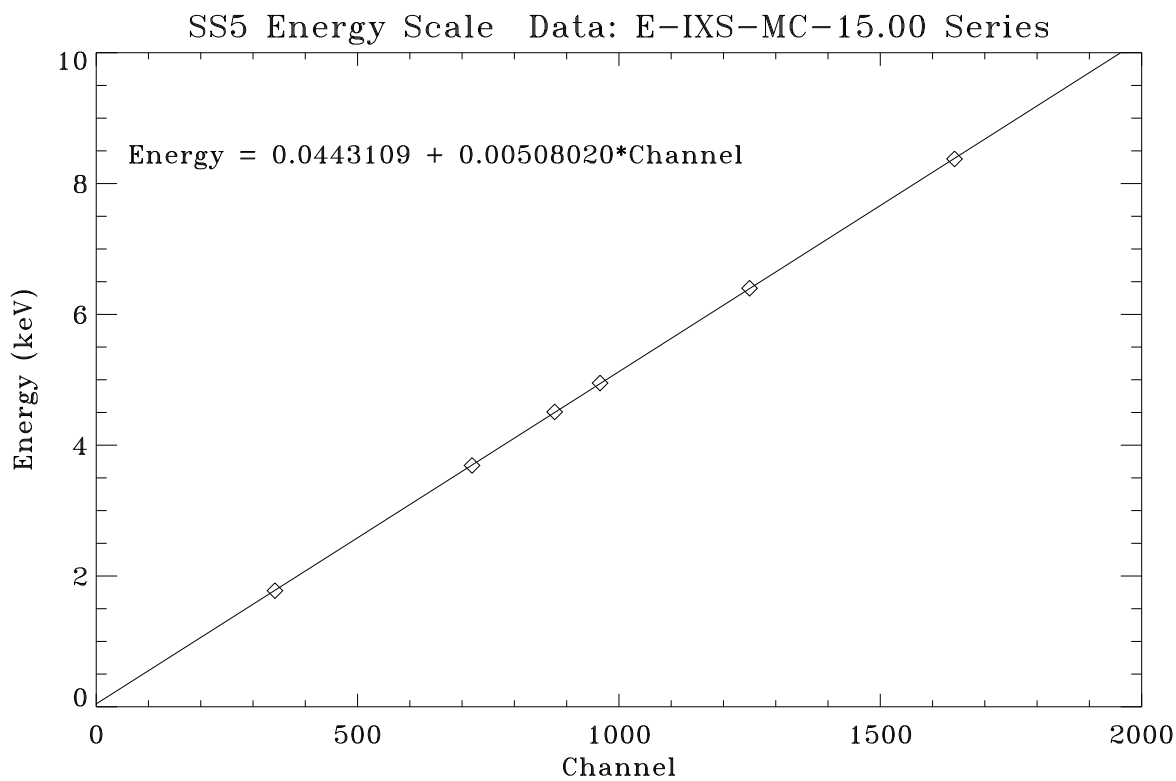
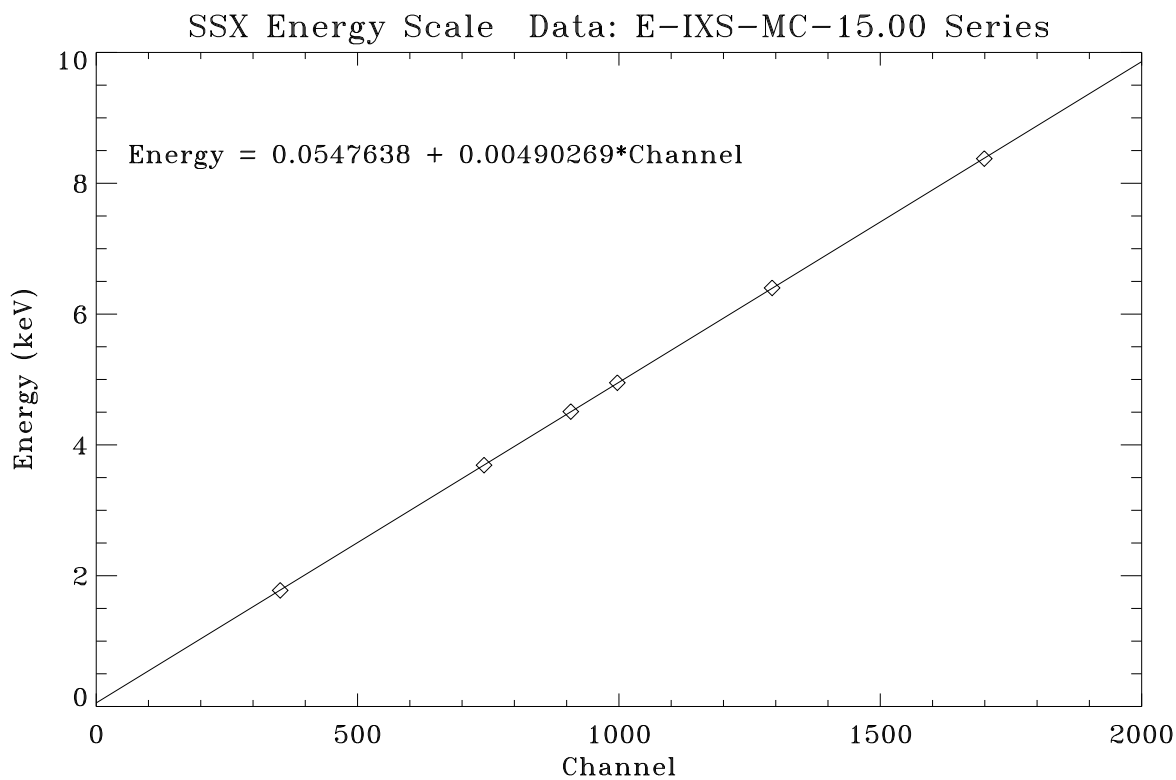


Figure 11.21: SSX and SS5 energy scales for the C-continuum effective area measurements (Phase-E), fitted with six X-ray line energies, averaged over four spectra (Run IDs 110539–110542).

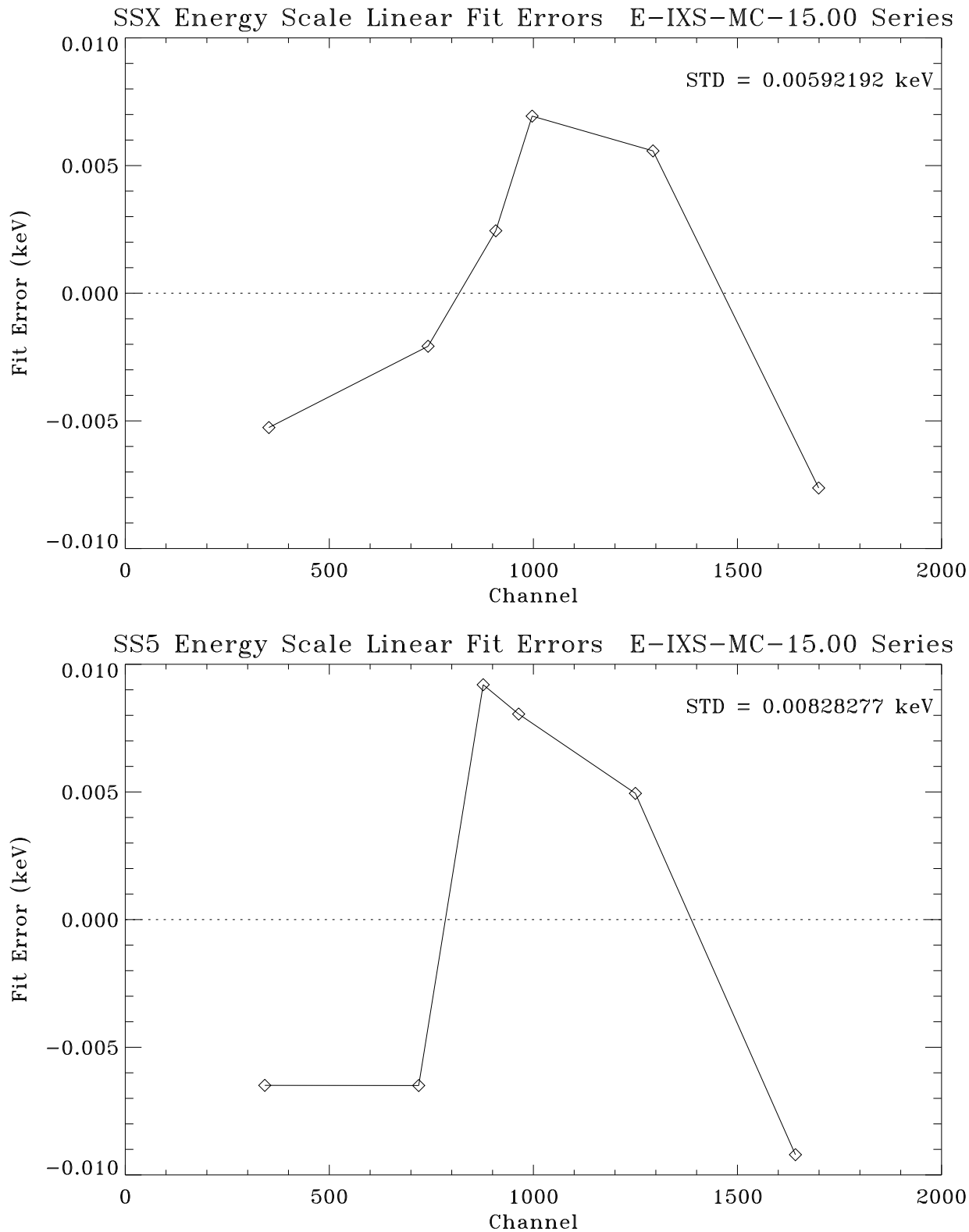


Figure 11.22: SSX and SS5 energy scale linear fit residuals for the C-continuum effective area measurements (Phase-E).

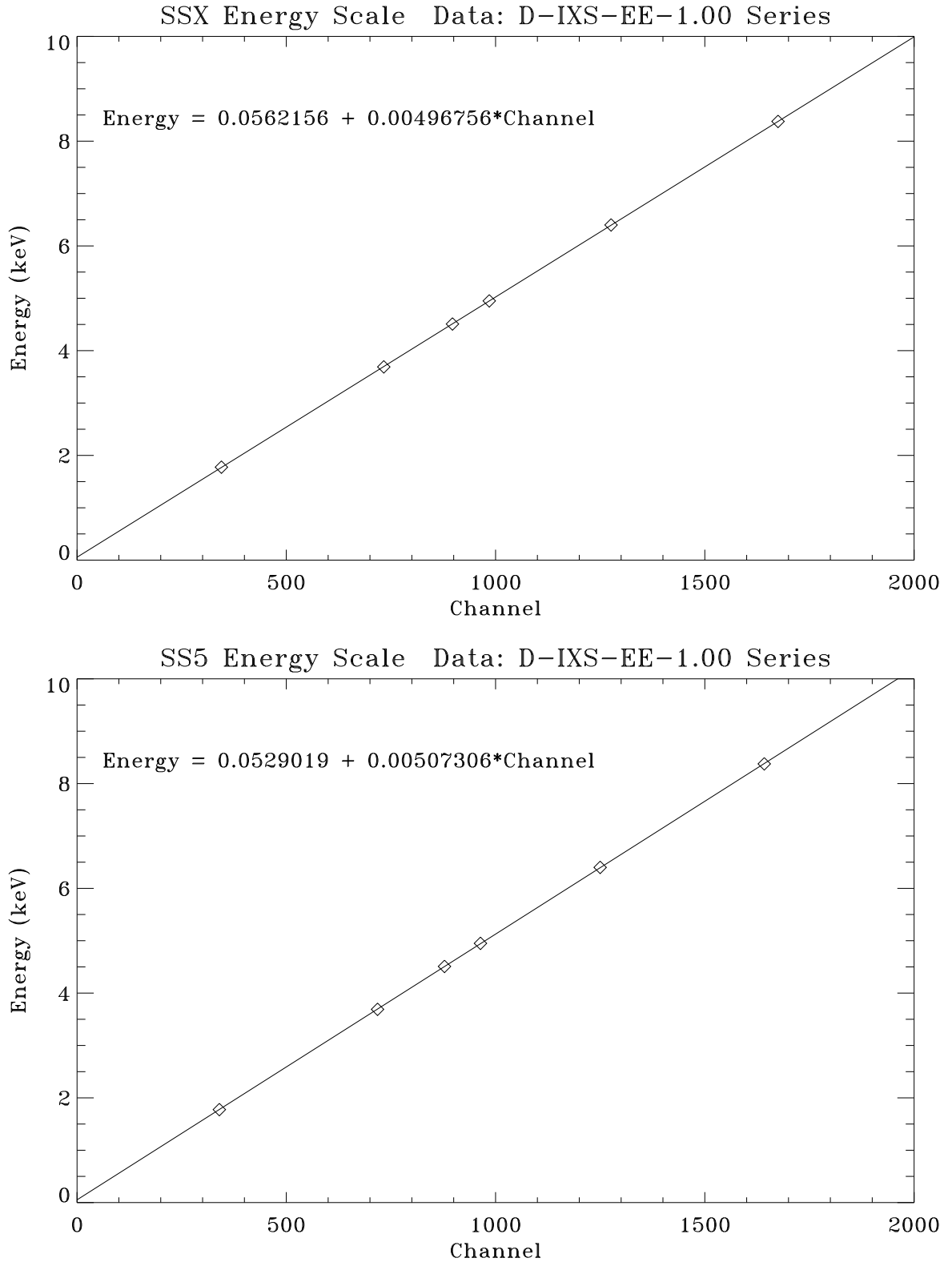


Figure 11.23: SSX and SS5 energy scales for the C-continuum effective area measurements (Phase-D), fitted with six X-ray line energies, averaged over four spectra (Run IDs: 108426, 108450, 108484, 108500).

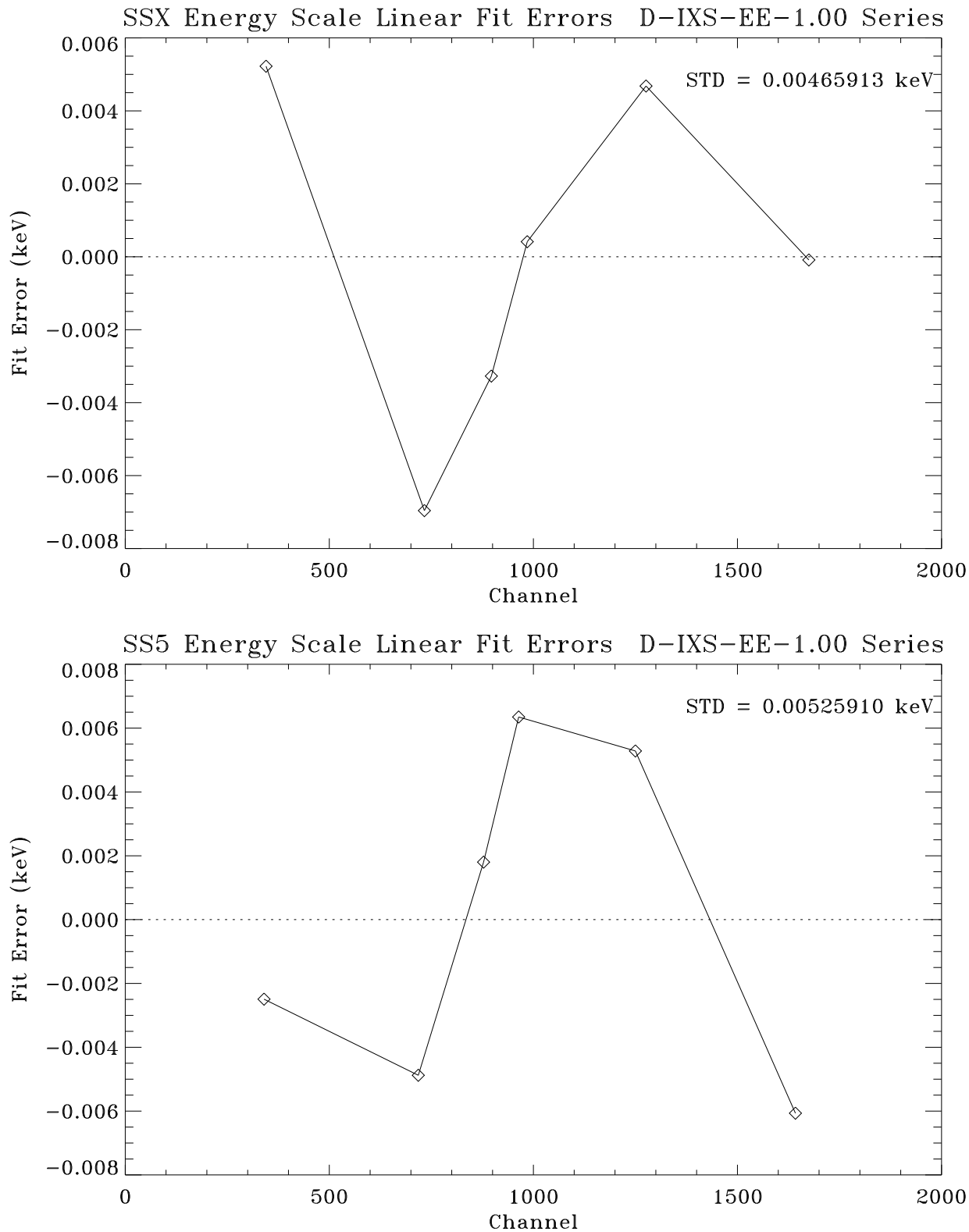


Figure 11.24: SSX and SS5 energy scale linear fit residuals for the C-continuum effective area measurements (Phase-D).

Table 11.4: SSD Energy Scale

Phase & Test	Detector	Spectral data	a	b
Phase-D	ssd_x	ssx_108426,450,484,500i000.pha	0.0562156	0.00496756
(EA Measurements)	ssd_5	ss5_108426,450,484,500i000.pha	0.0529019	0.00507306
Phase-E	ssd_x	ssx_110539,540,541,542i000.pha	0.0547638	0.00490269
(EA Measurements)	ssd_5	ss5_110539,540,541,542i000.pha	0.0443109	0.00508020
Phase-J	ssd_x	ss5_116414i000.pha	0.0541744	0.00482999
(Flat Field Test)	ssd_5	ssx_116414i000.pha	0.0464989	0.00502963

accurate estimation because of low-level noise; the lower level discriminators were set very low to extend the SSDs' energy coverage as low as possible. (For more details on this topic, see Chapter 5.)

A more accurate way to calculate the deadtime correction is to use the pulser method, in which artificial pulses are injected into the detector preamplifier to mimic real x-ray events. Since the pulses are processed just like X-rays – subject to interaction with hidden noise events, preamplifier reset pulses, *etc.* – fraction of pulses that appear in the output spectrum is, to a good approximation, equal to the system livetime fraction. The formula applying the deadtime correction to SSD spectra using the pulser method is:

$$Actual\ counts = Measured\ counts \cdot \frac{Input\ pulser\ counts}{Measured\ pulser\ counts} \quad (11.2)$$

where the *Measured counts* and *Measured pulser counts* are from pileup corrected spectra.<sup>2</sup>

Figure 11.25 illustrates how to determine the measured pulser counts. The top panel shows the *ssd\_x* pulser spectrum from the SSD flat field test (see Figure 11.17). The bottom panel shows the *ssd\_5* pulser spectrum. Two vertical dotted lines surround the pulser peak indicate the pulser region. A power law is fitted to the spectrum outside the pulser region (100 channels below the left vertical line plus 100 channels above the right vertical line). The measured pulser counts equal the total counts under the pulser spectrum within the pulser region minus the total counts under the fitted power law spectrum within the pulser region. Since the counting rates are very low for the flat field test, the pileup effects are negligible. Later when we use the same method to do the deadtime corrections for the effective area measurements, we apply it to the pileup corrected data only.

For X-ray counting rate calculated using the pulser deadtime correction, the formula is:

$$Actual\ rate = \frac{Measured\ counts}{TrueTime} \cdot Pulser\ deadtime\ correction \quad (11.3)$$

$$= \frac{Measured\ counts}{TrueTime} \cdot \frac{Input\ pulser\ counts}{Measured\ Pulser\ counts} \quad (11.4)$$

where *TrueTime* is the full integration time which is listed in the pha file header as *#trueTime.sec*.

<sup>2</sup>In Eq. 11.2, had the raw spectra (without pileup corrections) been used for the *Measured counts* and *Measured pulser counts*, there should be an additional factor of 1.0018 on the right hand side of the equation. This factor accounts for the non-randomness of the pulser events, which can not pileup or cause deadtime loss among themselves, in the case of a 27-Hz pulser rate and 10- $\mu$ sec amplifier shaping time constant. For more details, see Chapter 5.

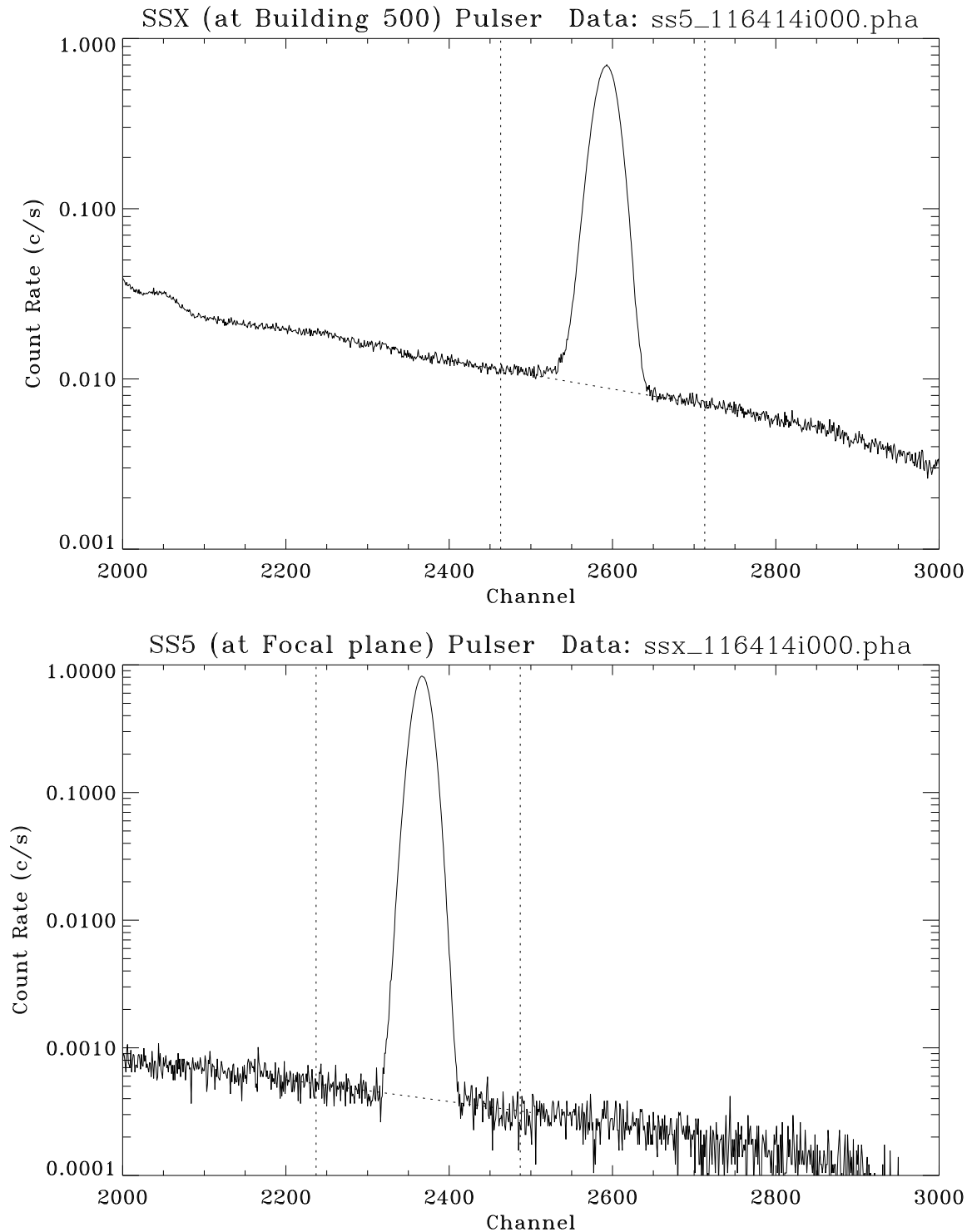


Figure 11.25: C-continuum flat field test SSX and SS5 pulser spectra. Two vertical dotted lines indicate the pulser region. A dotted line under the peak is the power law fit to the continuum. The pulser spectrum counts equal to the total counts under the pulser spectrum within the pulser region minus the total counts under the fitted power law spectrum within the pulser region.

For the effective area,  $A_{eff}(E)$ , calculated using the `ssd_x` counts,  $C_{ssd_x}(E)$ , divided by `ssd_5` counting rate,  $C_{ssd_5}(E)$ , the pulser deadtime correction is:

$$A_{eff} = A_{eff}(w/o\ deadtime\ correction) \cdot \frac{ssd\_x\ Pulser\ deadtime\ correction}{ssd\_5\ Pulser\ deadtime\ correction} \quad (11.5)$$

$$= A_{eff}(w/o\ deadtime\ correction) \cdot \frac{\left(\frac{ssd\_x\ Input\ pulser\ counts}{ssd\_x\ Measured\ pulser\ counts}\right)}{\left(\frac{ssd\_5\ Input\ pulser\ counts}{ssd\_5\ Measured\ pulser\ counts}\right)} \quad (11.6)$$

## 11.7 Beam Uniformity Test

We can obtain the relative quantum efficiency by dividing the two SSD spectra directly only if the X-ray beam intensities were exactly the same toward the directions of the two SSDs. But was the beam from the C-continuum source really uniform? To answer this question, a C-continuum beam uniformity test was made immediately after the C-continuum flatfield test (the flatfield test run ID is 116414, the beam uniformity test run ID is 116415).

During the beam uniformity test, the C-continuum source was operated in the same condition as for the flat field test, and the FPC-5 (i.e. the FPC detector in the Building 500) was scanned from the FPC-5 home position to the center (optical axis towards the HRMA), and to the SSD-5 home position, and then it scanned back in a reversed path. Two spectra were taken at each position. Figure 11.26 shows the six spectra taken during the C-continuum beam uniformity test. The small tick-marks on the horizontal axis are channels. The large tick-marks are the energies in unit of keV, based on the FPC-5 energy scale. The top two panels are the spectra at the FPC-5 home position, the middle two panels are the spectra at the optical axis, the bottom two panels are the spectra at the SSD-5 home position. Those six spectra look very similar. Taking the two spectra taken at the SSD-5 home position and dividing by the average of the two spectra taken on the optical axis, we obtain the relative flux ratio at those two positions as a function of energy (with low spectral resolution). Figure 11.27 show the relative flux ratio. It is seen that the beam is close to but not exactly uniform. It varies between 1.00 and 1.02. The solid curve in Figure 11.27 is a quadratic fit to the data. This is purely an empirical model which fits the data very well. The reduced  $\chi^2$  is 1.01652. So the beam uniformity as a function of energy can be well represented using this quadratic function, with a relative error of 0.0034:

$$FR = 1.01341 - 0.00512E + 0.000567E^2 \quad (11.7)$$

where  $FR$  is the flux ratio of at `ssd_5` position vs. on the optical axis, and  $E$  is the X-ray energy in unit of keV.

## 11.8 SSD Relative Quantum Efficiency

With all above considerations, we now finally can obtain the relative quantum efficiency of the two SSDs. The `ssd_5/ssd_x` quantum efficiency ratio,  $R(E)$ , is:

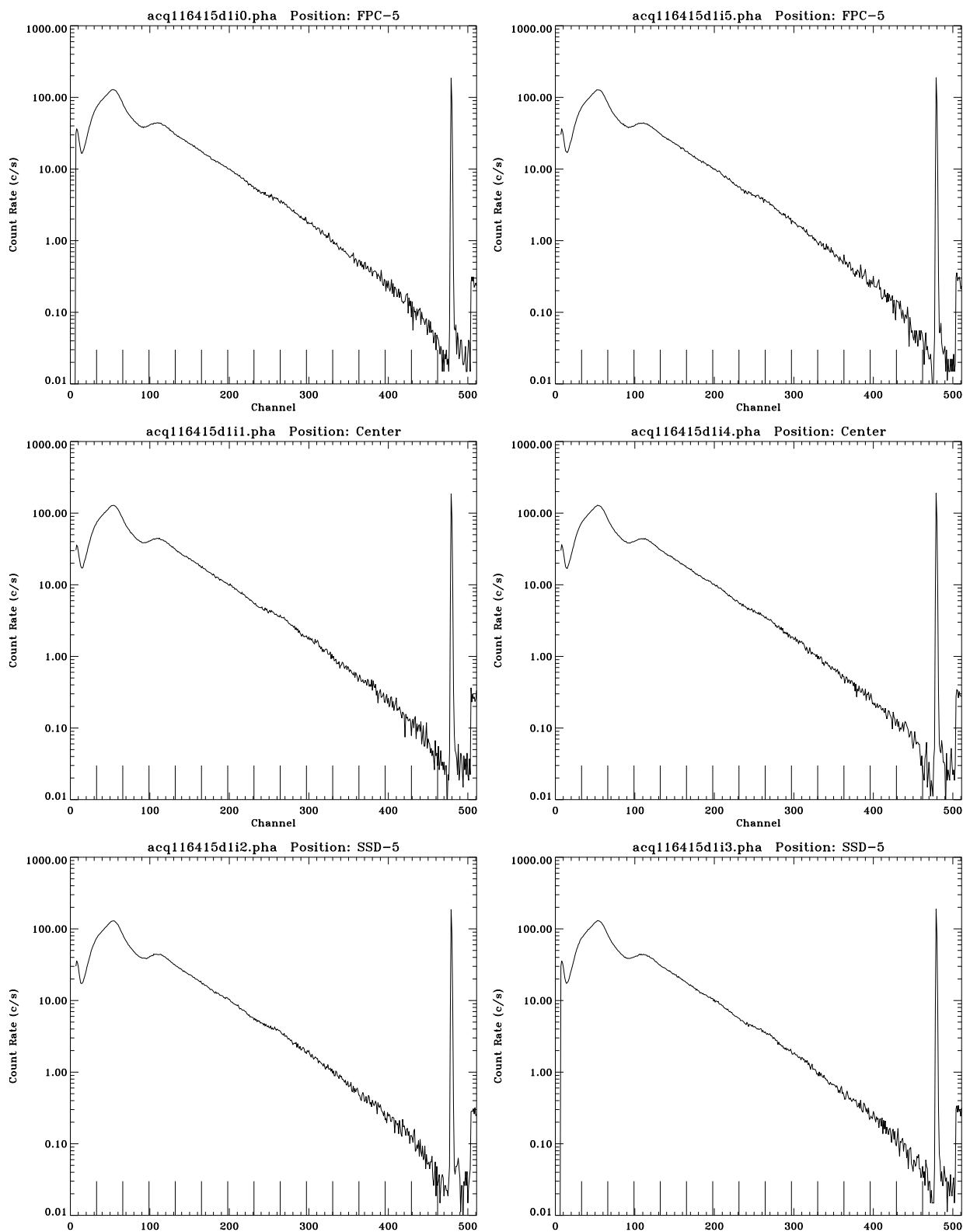


Figure 11.26: C-continuum source beam uniformity test. Scanned FPC-5 spectra at FPC-5 home, center or optical axis, and SSD-5 positions. The small tick-marks on the horizontal axis are channels. The large tick-marks are the energies in unit of keV, based on the FPC-5 energy scale.

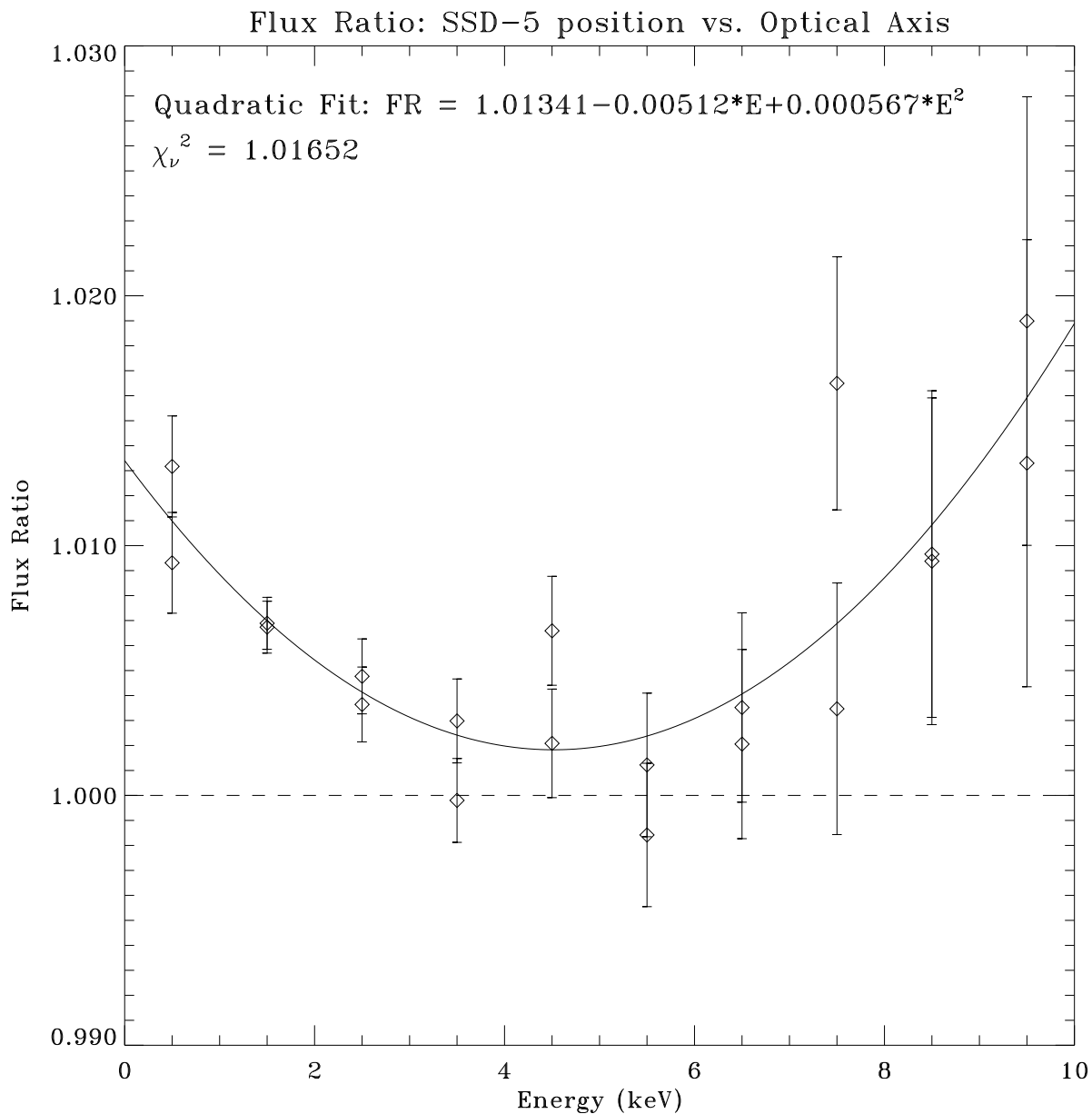


Figure 11.27: C-continuum FPC-5 beam flux ratio – SSD-5 position vs. optical axis – as a function of energy. Data are fit to a quadratic function.

$$R(E) = \frac{C_{\text{ssd}_5 \text{ flatfield}}(E)}{C_{\text{ssd}_x \text{ flatfield}}(E)} \cdot \frac{\text{ssd}_5 \text{ pulser deadtime correction}}{\text{ssd}_x \text{ pulser deadtime correction}} \cdot \frac{(\text{ssd}_5 \text{ to source distance})^2}{(\text{ssd}_x \text{ to source distance})^2} \cdot \frac{\text{ssd}_x \text{ aperture area}}{\text{ssd}_5 \text{ aperture area}} \cdot (\text{Beam flux ratio between ssd}_5 \text{ position and optical axis}) \quad (11.8)$$

where

- $C_{\text{ssd}_5 \text{ flatfield}}(E)$  and  $C_{\text{ssd}_x \text{ flatfield}}(E)$  are counts as functions of energy for the two SSDs from the flatfield test (see Figure 11.20).
- Using the method discussed in §11.6, the pulser deadtime corrections are calculated to be 1.0092 and 1.0569 for `ssd_5` and `ssd_x`, respectively.
- The source to SSD distances are 537.778 m and 38.199 m for `ssd_5` and `ssd_x`, respectively. Errors on the distance measurements are negligible for this calculation.
- For the flat field test, the apertures used were 2 mm (actual diameter =  $1.9990 \pm 0.0073$  mm) for `ssd_x` and 5 mm (actual diameter =  $4.9962 \pm 0.0073$  mm) for `ssd_5`. The combined relative error due to the two aperture area uncertainties is 0.0079.
- For the beam flux ratio, measured with FPC-5, we use Eq. 11.7.

So `ssd_5/ssd_x` Quantum Efficiency ratio is:

$$R(E) = \frac{C_{\text{ssd}_5 \text{ flatfield}}(E)}{C_{\text{ssd}_x \text{ flatfield}}(E)} \cdot \frac{1.0092}{1.0569} \cdot \frac{537.778^2}{38.199^2} \cdot \frac{1.9990^2}{4.9962^2} \cdot FR(E) \quad (11.9)$$

$$= \frac{C_{\text{ssd}_5 \text{ flatfield}}(E)}{C_{\text{ssd}_x \text{ flatfield}}(E)} \cdot 30.2964 \cdot (1.01341 - 0.00512E + 0.000567E^2) \quad (11.10)$$

Figure 11.28 shows the `ssd_5/ssd_x` QE ratio,  $R(E)$ , as a function of energy. The top panel show the QE ratio calculated using formula (Eq. 11.9).  $R(E)$  is near unity for energies above 2 keV as expected.  $R(E)$  varies drastically for energies below 2 keV, because of the icing effect (see the following section). In this case, there was more ice on the `ssd_x` therefore there was much higher transmission for `ssd_5`. A wiggle around line 1.775 keV indicates that the two SSDs have slightly different spectral resolution.

This  $R(E)$  curve is rather noisy. In the bottom panel, the data were binned into 0.3 keV bins and fitted to a flat ratio for energies above 3 keV (since at energies between 2 and 3 keV, the ratio was still slightly effected by the icing). The fit is very good, with a ratio of  $1.0141 \pm 0.0021$  and  $\chi^2_\nu = 1.0897$ . Here the error, 0.0021, is only the standard deviation of the mean of the binned flat field data in the 3–10 keV band. The total error for the quantum efficiency ratio also includes the beam uniformity error (0.0034) and the aperture size error (0.0079). Adding them in quadrature, the total relative error is 0.0088.

Because of the icing effect, the flat field test can only provide us with this ratio within 3–10 keV band. Since this ratio is reasonably energy independent, we assume, for the entire 0–10 keV energy band, the `ssd_5/ssd_x` quantum efficiency ratio is

$$R(E) = 1.0141 \pm 0.0089 \quad (11.11)$$

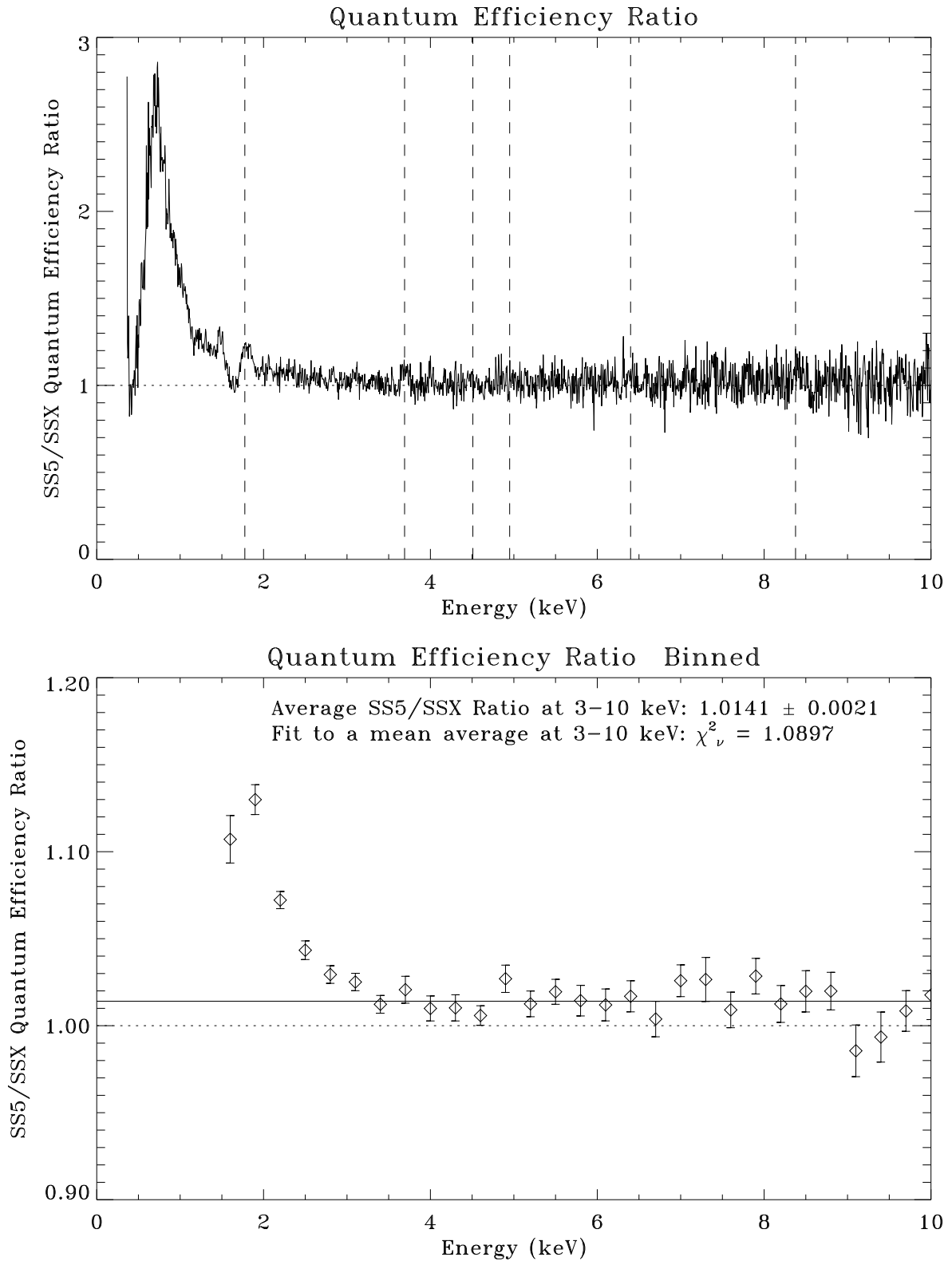


Figure 11.28: SS5/SSX quantum efficiency ratio. In the top panel, the large ratio below 2 keV is mainly due to the different ice build up on the two detectors. The bottom panel shows the ratio curve binned and fitted to a constant ratio. The solid line is the average ratio at 3–10 keV.

In the following we will use this QE ratio to calculate the HRMA effective area.<sup>3</sup>

## 11.9 SSD Icing Effect

In this section we discuss the so called SSD icing effect which we encountered in the previous section. Because SSD was cooled to liquid nitrogen temperature, even in its vacuum container, there was still a small amount of trapped water which condensed on the surface of the SSD to form a very thin layer of ice. This thin ice layer decreases the transmission of low energy X-rays.

In order to monitor the ice build up, a radioactive isotope  $^{244}_{96}\text{Cm}$  excited Fe source was placed on the aperture wheel and rotated in front of the `ssd_5` from time to time. The Figure 11.29 shows the Fe-L $\alpha$  (0.705 keV) and Fe-K $\alpha$  (6.40 keV) line intensity with error bars measured with `ssd_5` as a function of time from 960824 to 970521 (JD 2450320 – 2450590). The SSD C-continuum measurements were made in the middle of that period on 970113 and 970130. In the top panel, the Fe-L $\alpha$  intensity has two peaks, on 961031 and 970223, followed by declines. These two peaks indicate the time when the `ssd_5` was warmed up and we assume there was no ice then. The declines indicate the ice build up, reducing the transmission of Fe-L $\alpha$  into the `ssd_5`. In the bottom panel, the fluctuations of Fe-K $\alpha$  intensity could be due to icing, source aging and other temporal variations. To obtain the icing information, we only need to focus on the intensity ratio of Fe-L $\alpha$ /Fe-K $\alpha$ . Data from Figure 11.29 are listed in Table 11.5:

Table 11.5: SSD-500 Icing Data

Icing Period		Fe-L $\alpha$ Intensity	Fe-K $\alpha$ Intensity	Intensity ratio
First Period	Begin	34.2	90.8	0.3767
961031 – 970129	End	24.5	87.9	0.2787
End/Begin Ratio				74.00 %
Second Period	Begin	32.0	87.1	0.3673
970223 – 970514	End	23.5	86.5	0.2717
End/Begin Ratio				73.97 %

At the end of each ice build up period, the Fe-L $\alpha$ /Fe-K $\alpha$  transmission ratio is 74% of its initial value. This result can be used to obtain the ice thickness.

Figure 11.30 shows the X-ray transmission of ice. The solid line is a fit with Fe-L $\alpha$  (0.705 keV) line transmission being 74% of Fe-K $\alpha$  (6.40 keV) line transmission. The result is a 0.3  $\mu\text{m}$  ice layer. For reference, a transmission curve of a 1 $\mu\text{m}$  ice layer is plotted as a dotted line. According to this fit, during the calibration, the thickest ice build up on `ssd_5` was 0.3  $\mu\text{m}$ , at around 970129 and 970514. At other times, the ice was thinner. The `ssd_x` did not have a  $^{244}_{96}\text{Cm}$  source, so we do not have any data about the icing on the `ssd_x`.

Figure 11.30 tells us that icing has less than 0.7% effect for energies over 3 keV. At 2 keV, it can decrease the X-ray transmission by up to 2%. At the same time, icing has very severe effect for

<sup>3</sup>Because this ratio is energy independent, a large portion of the offset from unity is probably due to the combined aperture size error (0.0079). Because the aperture wheels were built into the SSD system, the apertures moved with the SSDs when the two SSDs were swapped during the flat field test. The measured `ssd_5/ssd_x` quantum efficiency ratio reflects a combination of real QE ratio of the SSDs and the aperture area ratio. In any case, the result of  $R = 1.0141 \pm 0.0089$  provides the correct QE ratio for the effective area measurements. To measure the 2 mm and 5 mm aperture areas more accurately will reduce the QE ratio error.

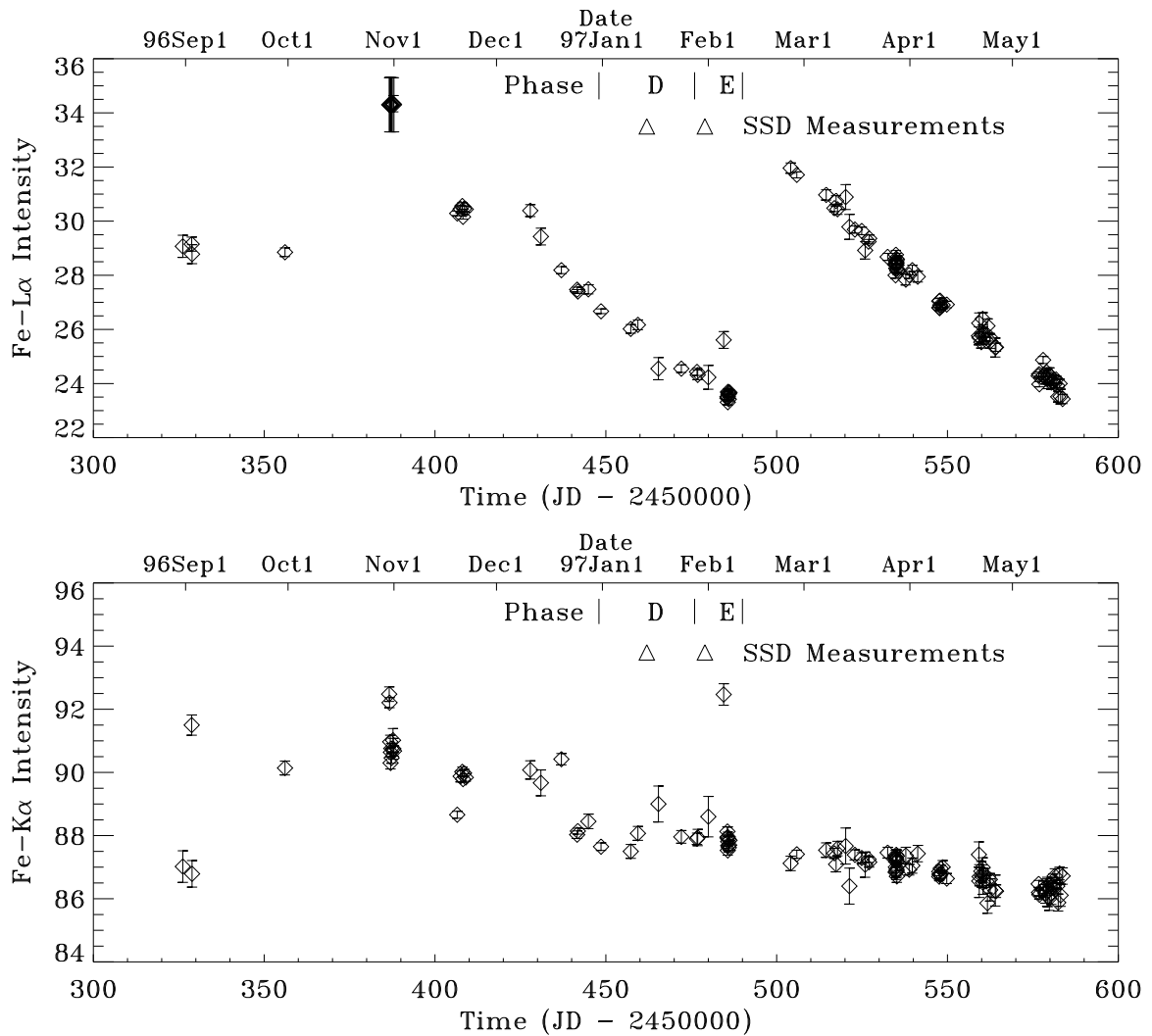


Figure 11.29: SSD 500 icing data (courtesy: Allyn Tennant). In order to monitor the ice build up, a radioactive isotope  $^{244}\text{Cm}$  excited Fe source was placed on the aperture wheel and rotated to front of the SS5 from time to time. The Figure shows the Fe-L $\alpha$  (0.705 keV) and Fe-K $\alpha$  (6.40 keV) line intensity with error bars measured with SS5 as a function of time from 960824 to 970521 (JD 2450320 – 2450590). Upper portions of each panel show the Phase D and E of the HRMA calibration and the dates of the SSD C-continuum measurements. In the top panel, the Fe-L $\alpha$  intensity has two peaks, on 961031 and 970223, followed by declines. These two peaks indicate the time when the SS5 was warmed up and assuming there was no ice then. The declines indicate the ice build up and therefore reducing the transmission of Fe-L $\alpha$  into the SS5. In the bottom panel, the fluctuations of Fe-K $\alpha$  intensity could be due to icing, source aging and other temporal variations. To obtain the icing information, we only need to focus on the intensity ratio of Fe-L $\alpha$ /Fe-K $\alpha$ . At the end of each ice build up period, the Fe-L $\alpha$ /Fe-K $\alpha$  transmission ratio is 74% of its value at the beginning. This result is used to obtain the ice thickness.

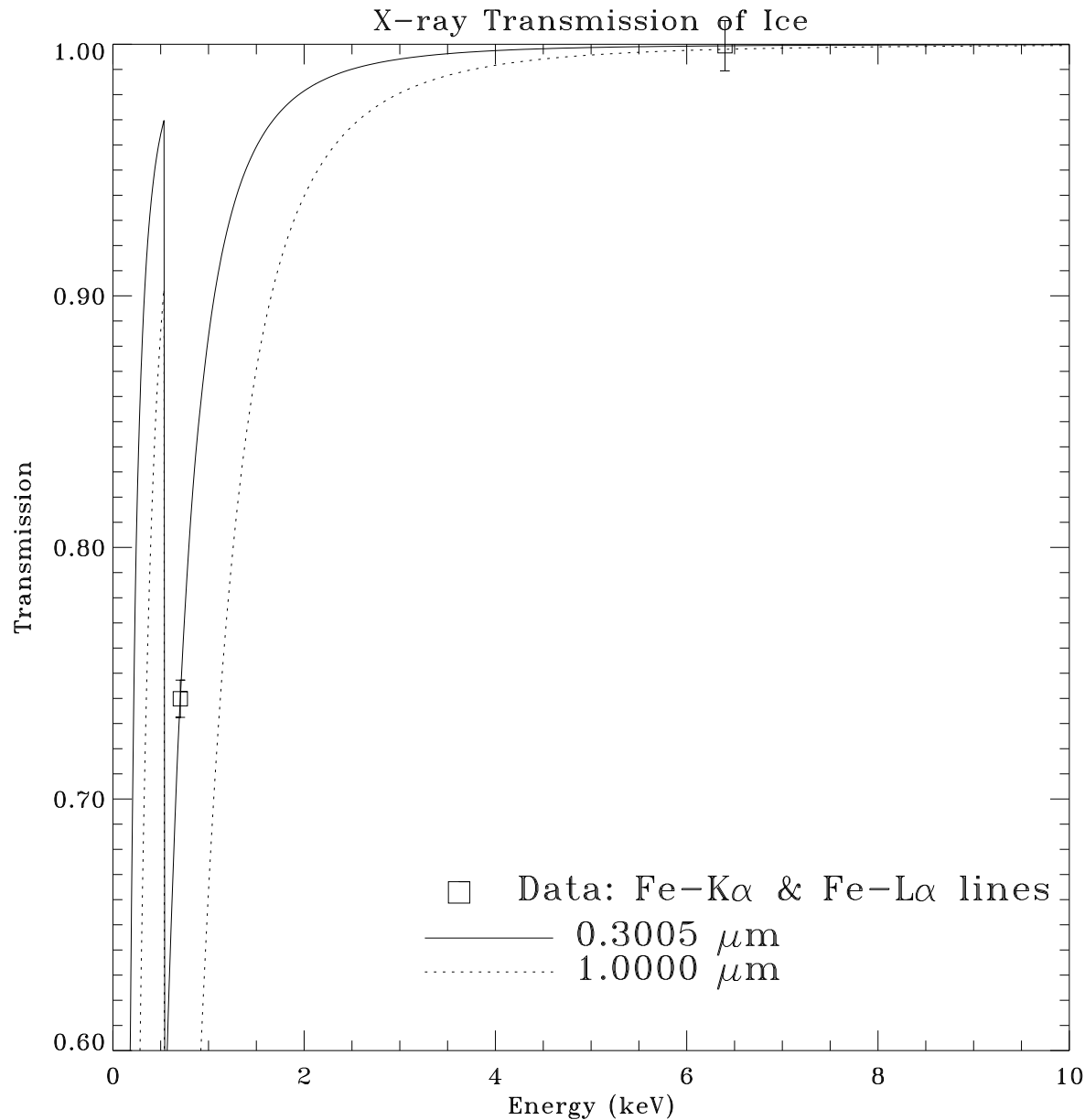


Figure 11.30: X-ray transmission of ice. The solid line is a fit with Fe-L $\alpha$  (0.705 keV) line transmission being 74% of Fe-K $\alpha$  (6.40 keV) line transmission. The result is a 0.3  $\mu\text{m}$  ice layer. According to this fit, during the calibration, the thickest ice build up on SS5 was 0.3  $\mu\text{m}$ , at around 970129 and 970514. This layer would have caused <2% decrease in transmission for X-rays above 2 keV, but a much larger attenuation below 2 keV. For reference, the transmission curve of a 1 $\mu\text{m}$  ice layer is plotted as a dotted line.

energies below 2 keV. Because the ice build up is a function of time and the build up on two SSDs could be different, the SSD data below 2 keV are not reliable. We have seen an indication of that in the previous section (see Figure 11.28). So in the flat field data analysis and in the following effective area data, we will not use the SSD spectra at low energies.

## 11.10 Background

During the HRMA calibration, background runs were taken almost every day when the source valve was closed and all the detectors were turned on. To evaluate the effect of the background on the SSD C-continuum measurements, we examined all the SSD background spectra and found that the background is extremely low.

Figure 11.31 shows a pair of typical SSD background spectra. It was taken on 970124, with TRW ID D-IXF-BG-1.021, run ID 110036 and integration time of 2100 seconds. They are summed spectra of seven background runs of 300 seconds each. It is seen that, other than the pulser peak near channel 2400 and some electronic noise at near channel 60, the spectra are very clean in the region to be used to reduce the HRMA effective area (channels 100–2000). The average counts per channel per second are 0.000046 and 0.000024 for `ssd_x` and `ssd_5`, respectively. For all the background spectra, the average counting rate in channels 100–2000 ranges from 0.000019 to 0.000098 c/s/ch. This level of background is negligible in our data analysis.

## 11.11 Data Analysis and Reduction

With all the above considerations, we can now obtain the HRMA effective area. In this section we use the C-continuum SSD on-axis effective area measurements in Phase-E to demonstrate the data reduction process. All other measurements listed in Tables 11.1 and 11.2 can be reduced the same way.

The four Phase-E SSD effective area measurements for the four shells have TRW IDs of E-IXS-MC-15.001,2,3,4 and run IDs 110539, 110540, 110541, and 110542. The “MC” in TRW ID stands for molecular contamination measurements, but they also serve as on-axis effective area C-continuum measurements. They have longer integration time, 1000 seconds, and the largest `ssd_x` aperture, 2 mm, used for this kind of measurements.

We start with the pileup corrected `ssd_x` and `ssd_5` spectra (see §11.3). In Figures 11.9–11.16, the upper panels show the pileup corrected `ssd_x` and `ssd_5` spectra. The SSD energy scale was determined in §11.5.

Using the linear fit parameters listed in Table 11.4, each of the eight SSD spectra was scaled as a function of energy. Then they were binned into equal energy bins by dividing the spectra by the fitting parameter  $b$  in Table 11.4. The pulser deadtime corrections are also applied to the spectra the same way as to the flat field data. The results are four pairs of `ssd_x` and `ssd_5` spectra as functions of energy and in units of counts/second/keV. They are shown in the top and middle panels of Figures 11.32–11.35. The dashed vertical lines indicate the six X-ray lines used for energy scaling.

## 11.12 Effective Area

The HRMA effective area at the XRCF is defined to be the photon collecting area in the plane of the HRMA pre-collimator entrance, which is 1491.64 mm forward from CAP Datum-A (the front

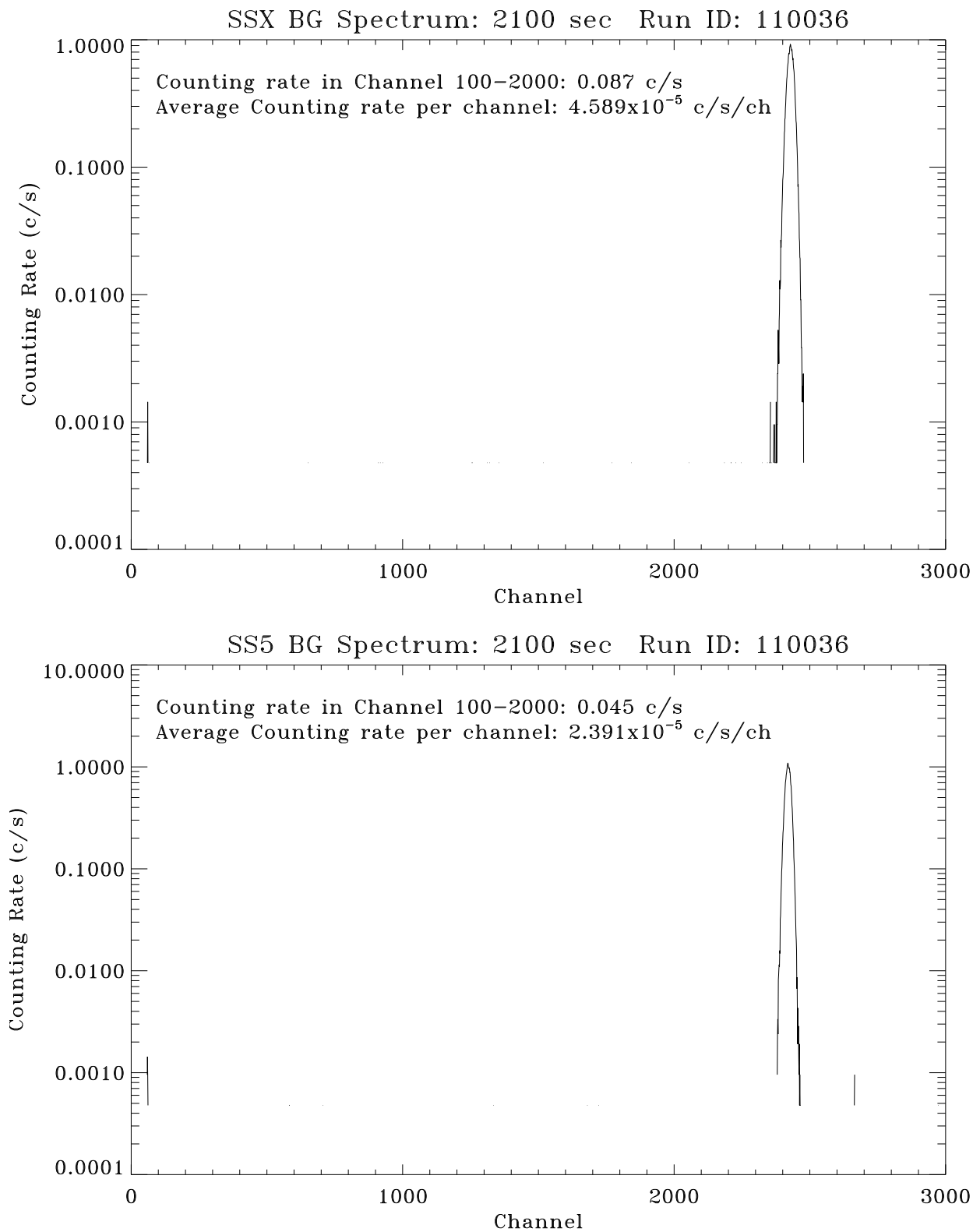


Figure 11.31: SSX and SS5 spectra of background run. Date: 970124; TRW ID: E-IXS-BG-1.021; Run ID: 110036; Integration time: 2100 seconds. The average counts per channel per seconds are 0.000046 and 0.000024 for SSX and SS5, respectively.

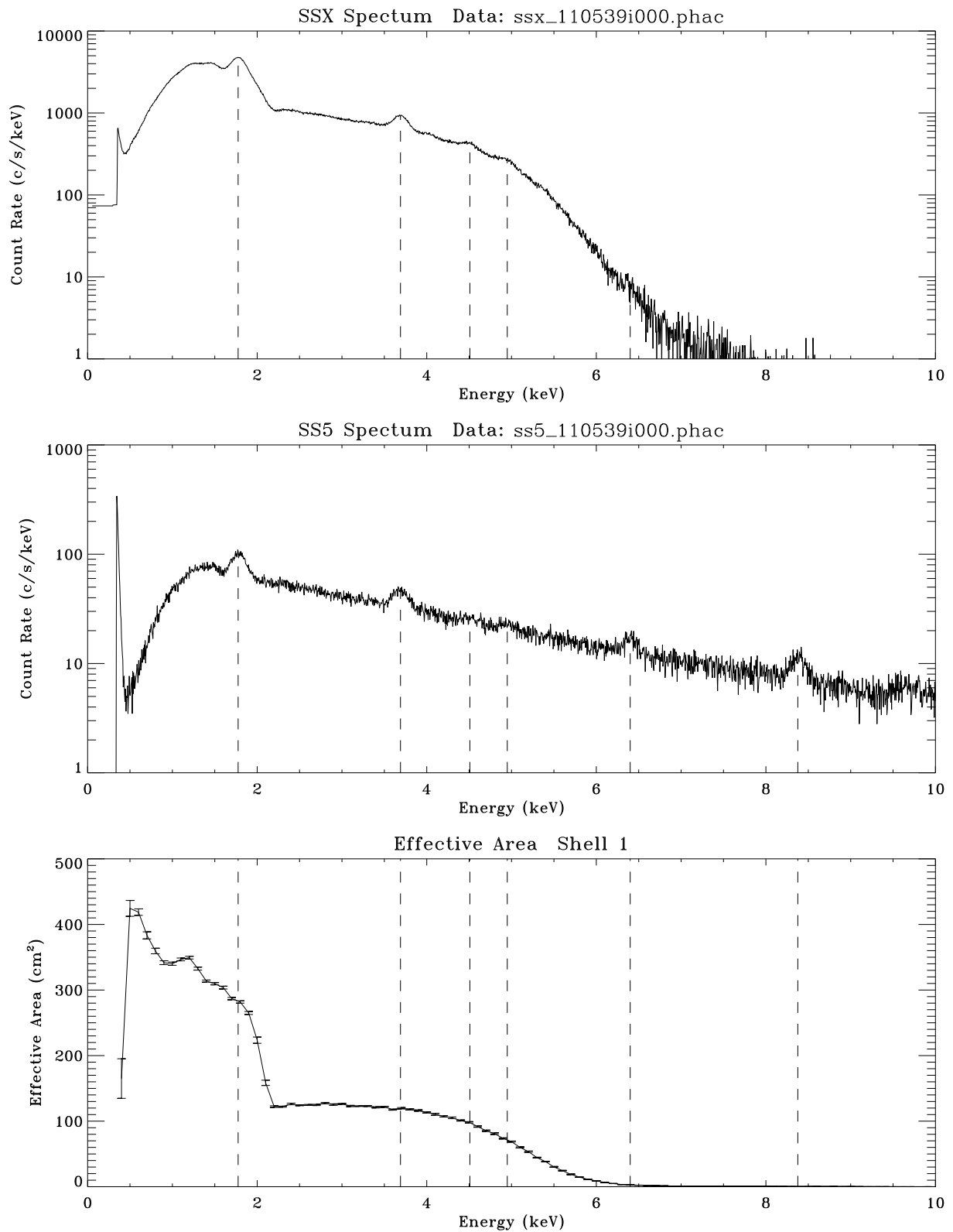


Figure 11.32: SSD C-continuum effective area measurement: Shell 1; 2 mm aperture; Run ID: 110539. Top panel is the SSX spectrum. Middle panel is the SS5 spectrum. Bottom panel is the measured effective area.

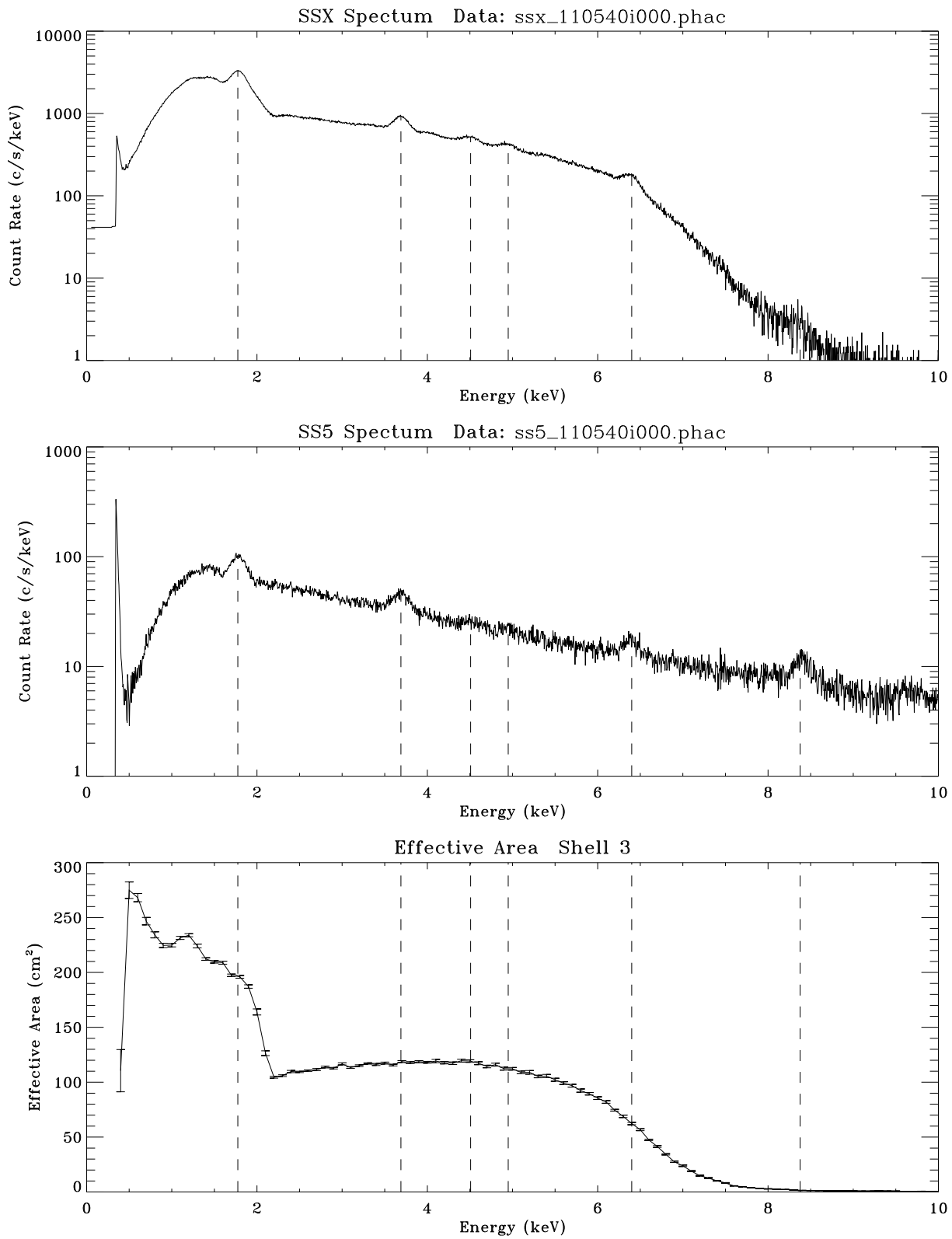


Figure 11.33: SSD C-continuum effective area measurement: Shell 3; 2 mm aperture; Run ID: 110540. Top panel is the SSX spectrum. Middle panel is the SS5 spectrum. Bottom panel is the measured effective area.

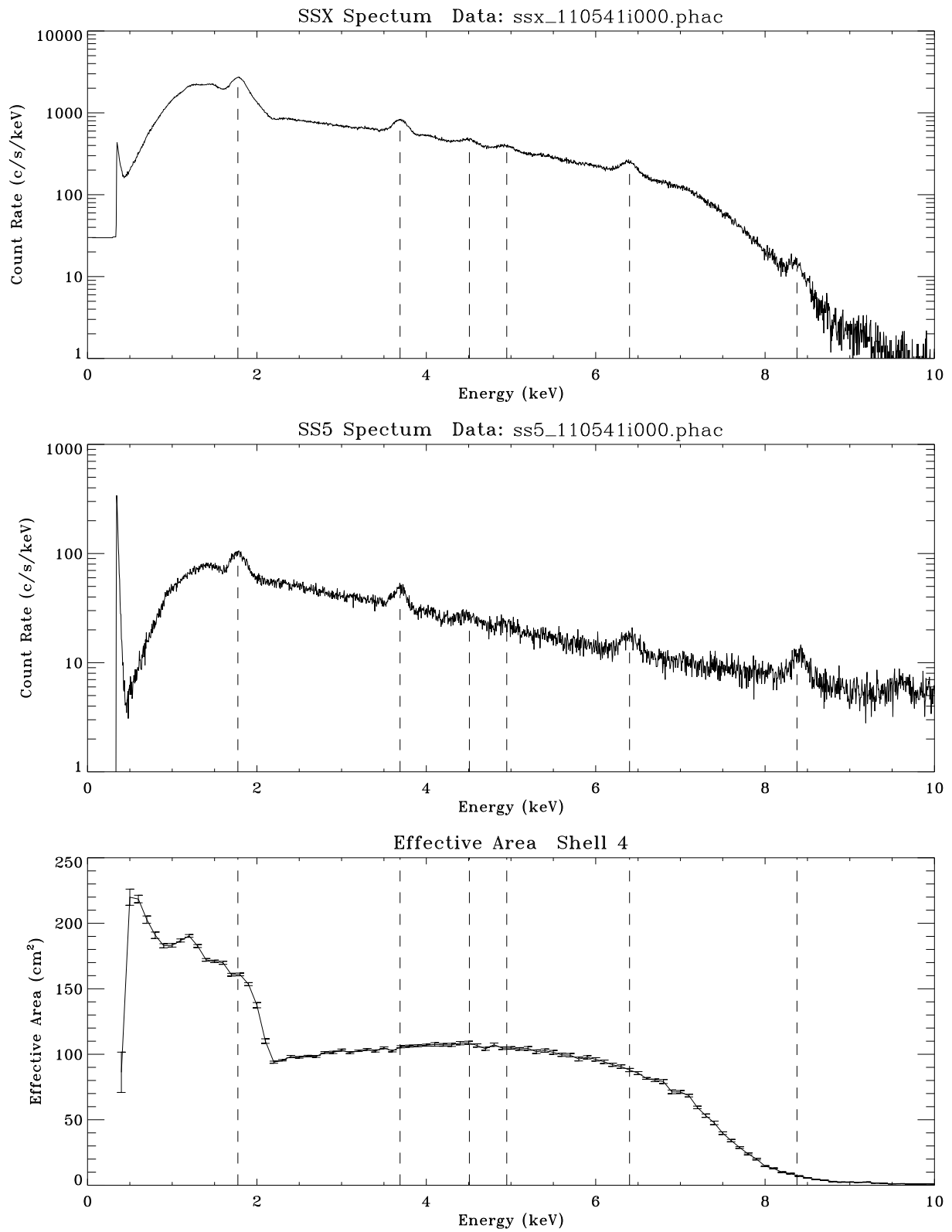


Figure 11.34: SSD C-continuum effective area measurement: Shell 4; 2 mm aperture; Run ID: 110541. Top panel is the SSX spectrum. Middle panel is the SS5 spectrum. Bottom panel is the measured effective area.

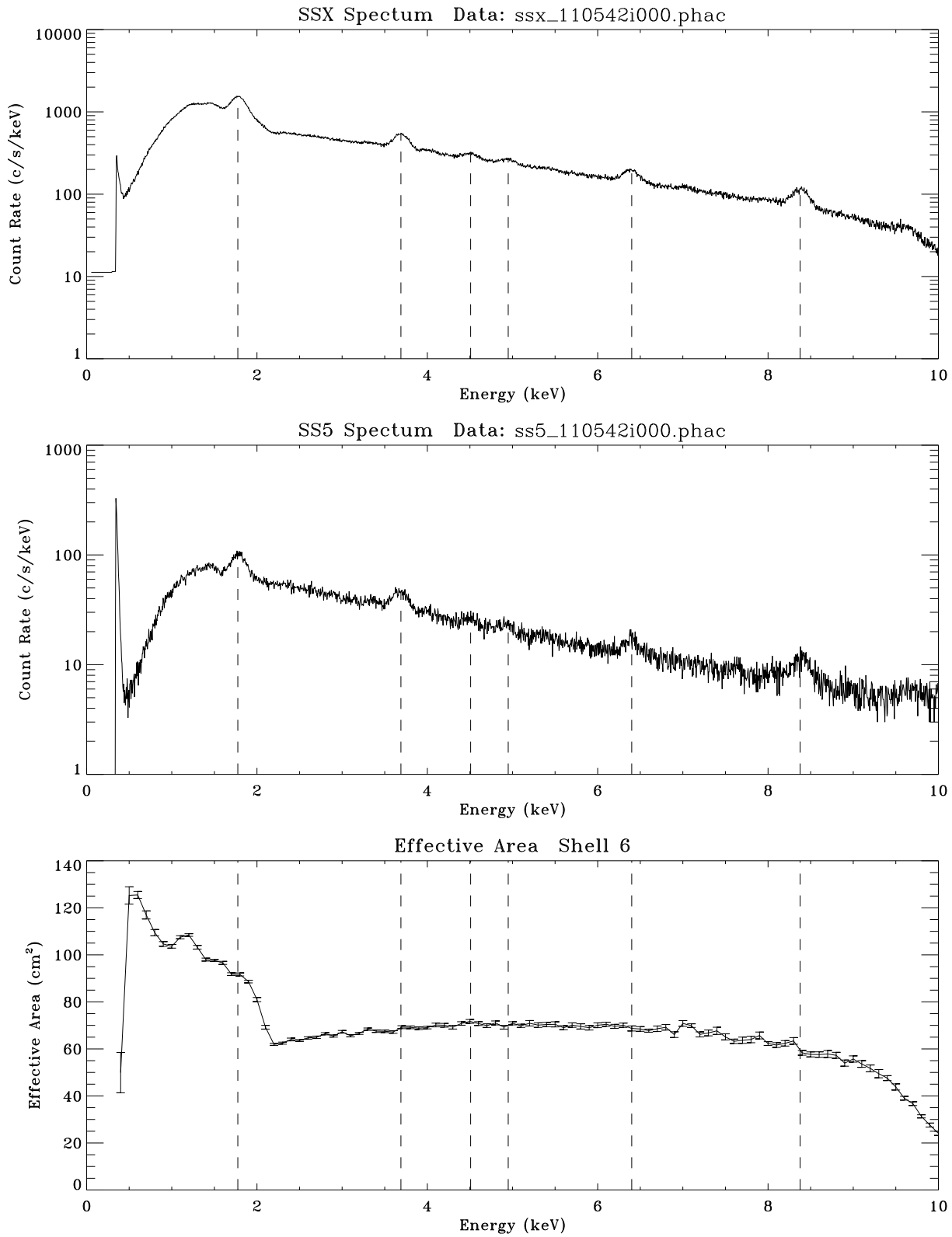


Figure 11.35: SSD C-continuum effective area measurement: Shell 6; 2 mm aperture; Run ID: 110542. Top panel is the SSX spectrum. Middle panel is the SS5 spectrum. Bottom panel is the measured effective area.

surface of the Central Aperture Plate), i.e. 526.01236 meters from the source.<sup>4</sup>

For the C-continuum SSD measurements, the HRMA mirror effective area,  $A_{eff}(E)$ , is:

$$A_{eff}(E) = \frac{C_{ssx}(E)}{C_{ss5}(E)} \cdot \frac{PDC_{ssx}}{PDC_{ss5}} \cdot \frac{D_{hrma}^2}{D_{ss5}^2} \cdot A_{ss5} \cdot R(E) \quad (11.12)$$

where

- $C_{ssx}(E)$  and  $C_{ss5}(E)$  are the `ssd_x` and `ssd_5` spectra with the correct energy scale and equal energy bins (in units of counts/second/keV).
- $PDC_{ssx}$  and  $PDC_{ss5}$  are the pulser deadtime corrections for the `ssd_x` and `ssd_5`.
- $D_{hrma} = 526.01236$  meter is the distance from the source to the HRMA pre-collimator entrance, where the effective area is defined.
- $D_{ss5} = 38.199$  meters is the distance from the source to `ssd_5`.
- $A_{ss5}$  is the `ssd_5` aperture area. A 2 mm aperture was used for all the measurements. Its actual equivalent diameter is  $1.9990 \pm 0.0073$  mm. So  $A_{ss5} = 0.031385 \pm 0.00023$  cm<sup>2</sup>
- $R(E) = 1.0141 \pm 0.0089$  is the relative `ssd_5/ssd_x` quantum efficiency from the flat field test.

Because each of the `ssd_5` spectra are rather noisy, four `ssd_5` spectra are averaged to make  $C_{ss5}(E)$ , which has the noise reduced by a factor of two. The source intensity was stable enough during these four measurements so the temporal fluctuation is negligible.

The  $C_{ssx}(E)$  and  $C_{ss5}(E)$  are obtained using the method discussed in the previous Section. The  $PDC_{ssx}$  and  $PDC_{ss5}$  are obtained using the method discussed in §11.6 and listed in Table 11.6.

Table 11.6: Effective Area Measurements SSD Pulser Deadtime Corrections

Run ID	$PDC_{ssx}$	$PDC_{average\ ss5}$	$PDC_{ssx}/PDC_{average\ ss5}$
110539	1.11827	1.01651	1.10011
110540	1.10408	1.01651	1.08615
110541	1.09579	1.01651	1.07799
110542	1.07069	1.01651	1.05330

So the effective area of each HRMA shell measured with the C-continuum and SSD is:

$$\begin{aligned} A_{eff}(E) &= \frac{C_{ssx}(E)}{C_{average\ ss5}(E)} \cdot \frac{PDC_{ssx}}{PDC_{average\ ss5}} \cdot \frac{526.01236^2}{38.199^2} \cdot 0.031385 \cdot 1.0141 \quad (cm^2) \\ &= 6.03519 \cdot \frac{C_{ssx}(E)}{C_{average\ ss5}(E)} \cdot \frac{PDC_{ssx}}{PDC_{average\ ss5}} \quad (cm^2) \end{aligned} \quad (11.13)$$

The bottom panels of Figures 11.32–11.35 show the effective area results according to Eq. 11.13. The six vertical dashed lines are the six energy lines used to determine the energy scale. Each

<sup>4</sup>This definition is necessary because of the diverging X-ray beam at the XRCF. It is not necessary for on-orbit case as the X-rays are parallel and the effective area is the same in any plane.

effective area curve was binned into 0.1 keV energy bins. According to the SSD energy scale, there are 20 channels in each energy bin. The plotted error bars are the standard deviation of the mean in the energy bins. Systematic errors such as the `ssd_5` aperture area uncertainty (0.0073) and the SSD quantum efficiency ratio error (0.0088) are not included in these four plots but will be included later in the final results.

## 11.13 Error Analysis

The error of the HRMA effective area is:

$$\sigma_{ea} = (\sigma_{e-bin}^2 + \sigma_{2mm-ap}^2 + \sigma_{qe}^2)^{1/2} \quad (11.14)$$

where

$\sigma_{e-bin}$	Standard deviation of the mean in each 0.1 keV bin of the SSD spectra	~1–4%
$\sigma_{2mm-ap}$	Uncertainty of the <code>ssd_5</code> 2 mm aperture area ( $0.031385 \pm 0.00023 \text{ cm}^2$ )	0.73%
$\sigma_{qe}$	Error of the SSD quantum efficiency ratio ( $1.0141 \pm 0.0089$ )	0.88%
$\sigma_{ea}$	Effective area error	~1.3–4%

where the error of the SSD quantum efficiency ratio is from the flat field test data reduction:

$$\sigma_{qe} = (\sigma_{std}^2 + \sigma_{bu}^2 + \sigma_{ap}^2)^{1/2} \quad (11.15)$$

where

$\sigma_{std}$	Standard deviation of the mean of QE ratio flatfield data in 3–10 keV band	0.21%
$\sigma_{bu}$	Error of beam uniformity	0.34%
$\sigma_{ap}$	Uncertainty of the 2 mm and 5 mm aperture areas	0.79%
$\sigma_{qe}$	Total quantum efficiency ratio error	0.88%

For the effective area of the entire HRMA, the absolute errors are the quadrature sum of the absolute errors from the four shells. Therefore its relative errors are reduced accordingly, to ~0.7–3.6%.

## 11.14 Comparing Measurements with the Raytrace Prediction

Figures 11.36–11.39 compare the measured effective area with the raytrace prediction within a 2 mm aperture for each mirror shells. In the top panels, the solid lines are the raytrace predictions, the dotted lines are the SSD measured effective area with the C-continuum source, which is the same as plotted in the bottom panel of Figures 11.32–11.35. As mentioned before, the SSD data below 2 keV (most parts are higher than the raytrace prediction) should be ignored due to the icing effect. The FPC spectral line data are also plotted in the figures for comparison.

For energies above 2 keV, the data are significantly below the prediction, especially for shell 1. The bottom panels of Figures 11.36–11.39 show the effective area ratio of data/raytrace. It is seen that for shell 1, the data is about ~10–15% less than the prediction at 2–4 keV and ~15–30% less than the prediction for shell 1 at 4–6 keV. For other shells the discrepancies are less than 15%.

Figure 11.40 shows the full HRMA effective area data with the raytrace prediction within a 2 mm aperture. The SSD C-continuum data and four of the seven FPC line spectral data (0.277 keV, 1.49 keV, 4.51 keV and 6.40keV) are the sums of data from the four shells. The SSD line spectral

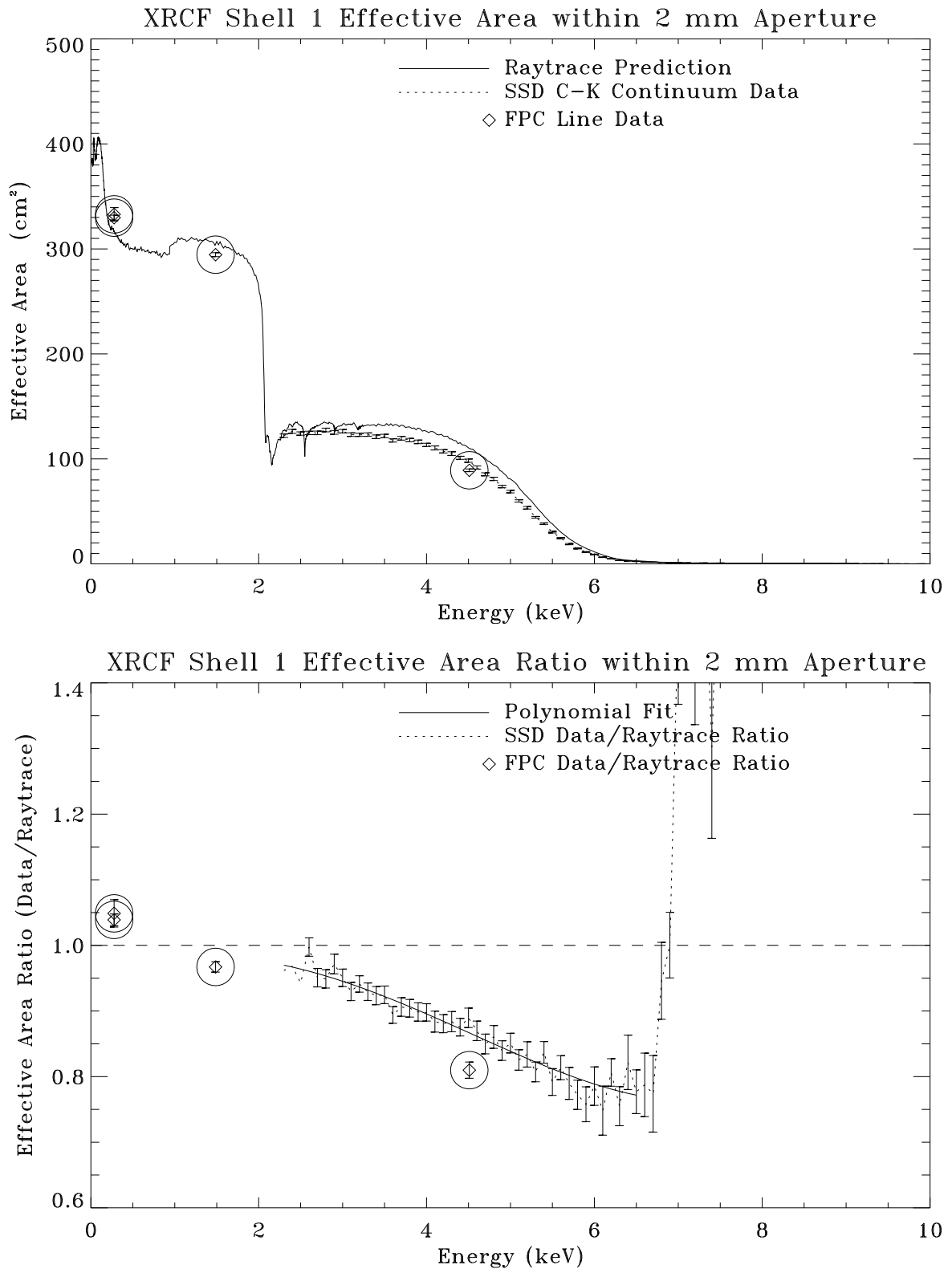


Figure 11.36: Calibration data vs. raytrace prediction. Top panel shows the XRCF Shell 1 effective area within 2 mm aperture. Bottom panel shows the effective area ratio of data/raytrace.

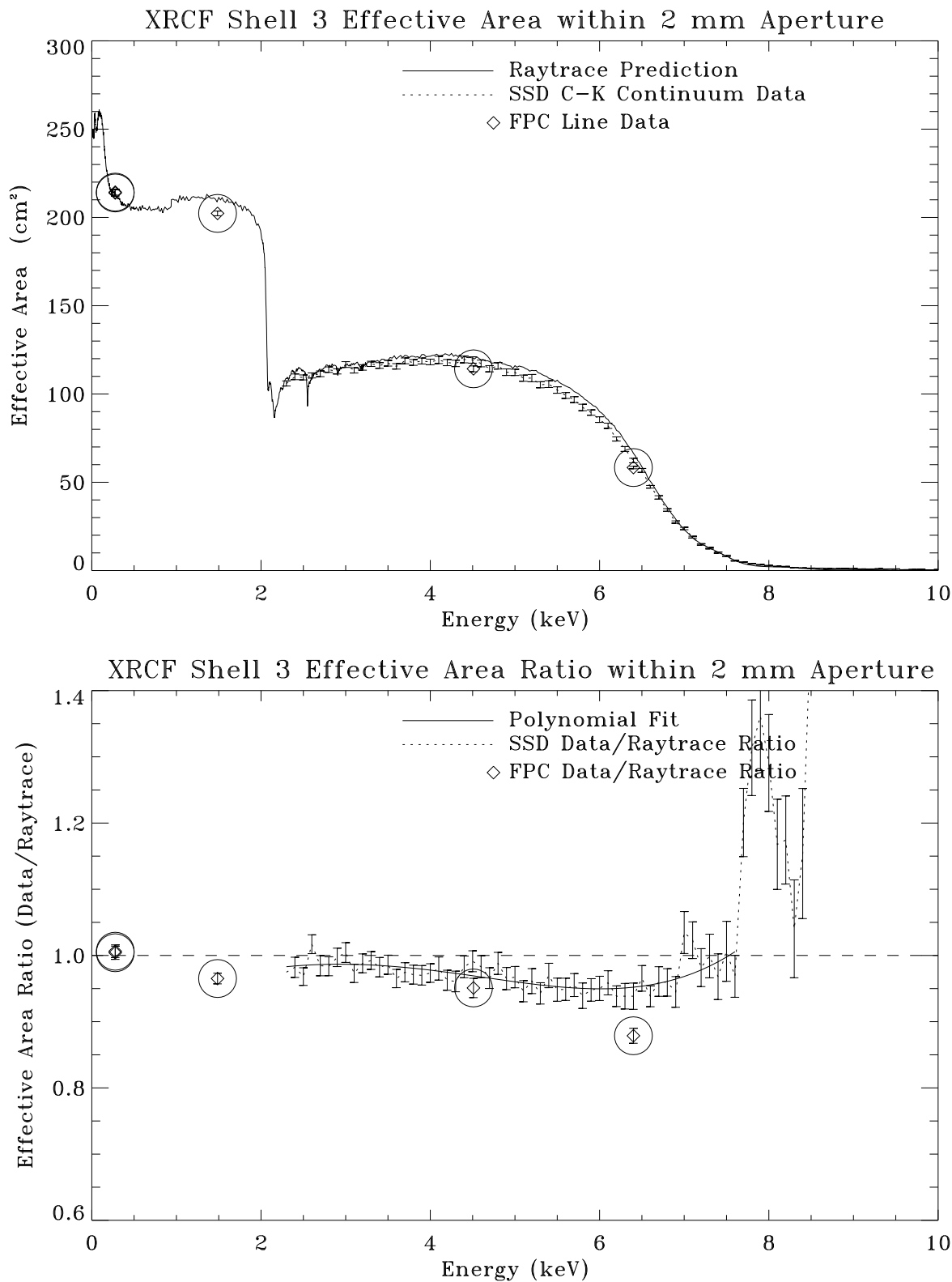


Figure 11.37: Calibration data vs. raytrace prediction. Top panel shows the XRCF Shell 3 effective area within 2 mm aperture. Bottom panel shows the effective area ratio of data/raytrace.

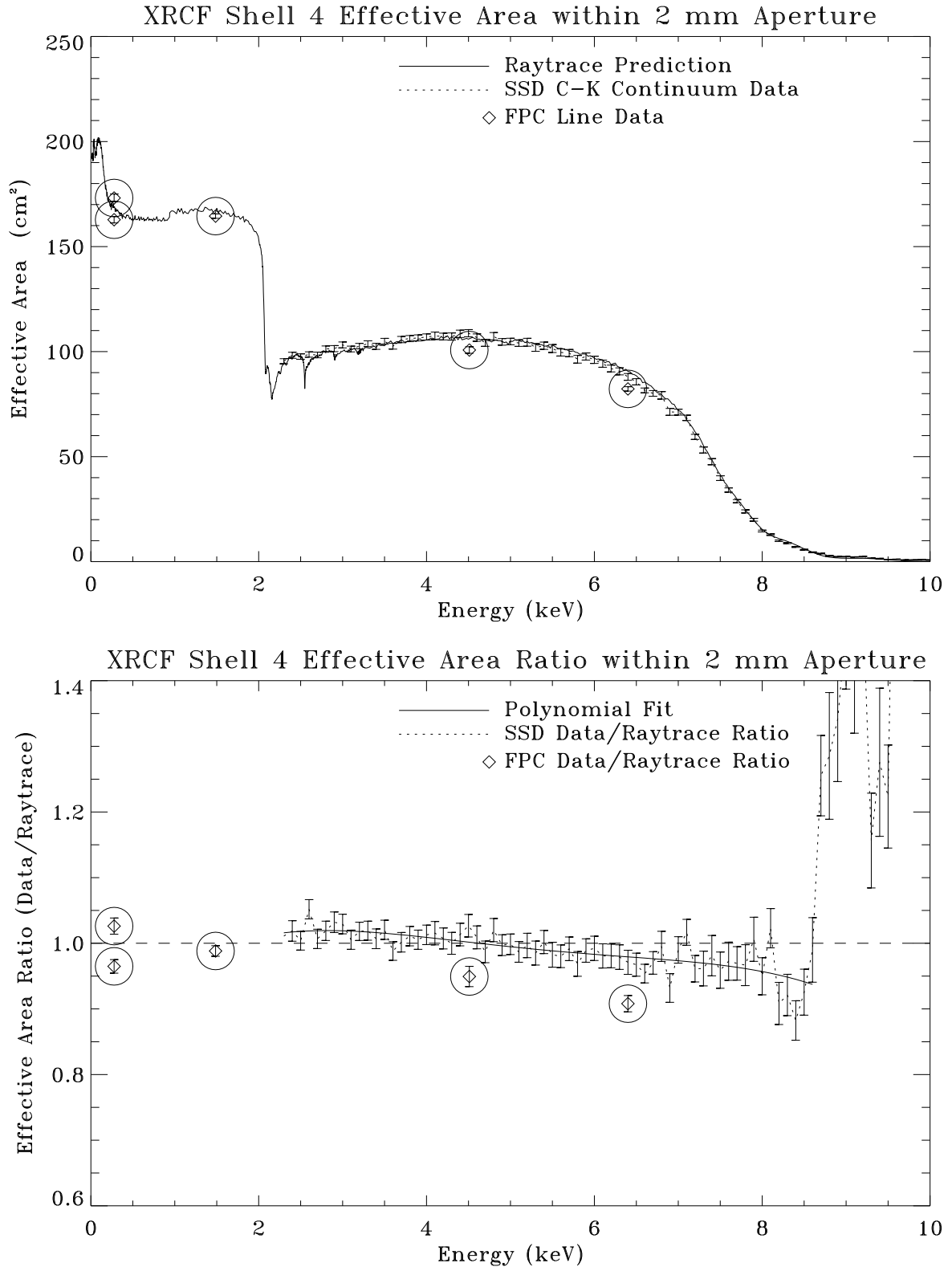


Figure 11.38: Calibration data vs. raytrace prediction. Top panel shows the XRCF Shell 4 effective area within 2 mm aperture. Bottom panel shows the effective area ratio of data/raytrace.

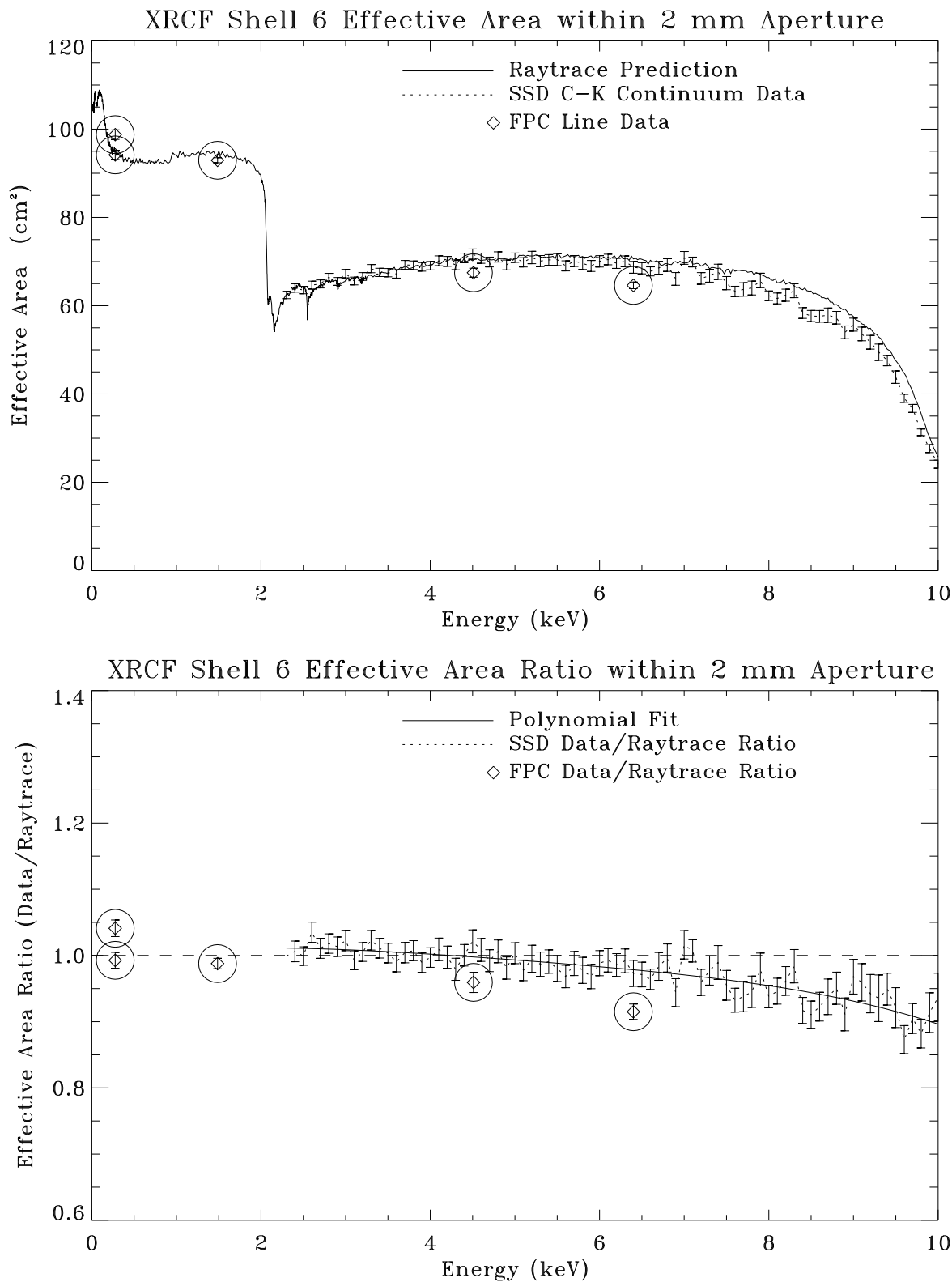


Figure 11.39: Calibration data vs. raytrace prediction. Top panel shows the XRCF Shell 6 effective area within 2 mm aperture. Bottom panel shows the effective area ratio of data/raytrace.

data and three of the seven FPC line spectral data (0.93 keV, 5.41 keV and 8.03 keV) are the direct measurements of the full HRMA. The data are below the raytrace prediction by  $\sim 5\text{--}10\%$  in the 2–10 keV band. In the raytrace prediction, there is a dip near the Ir M-edge (2.05 keV). The SSD C-continuum data could not reveal it due to the finite spectral resolution of the SSD. However, the SSD spectral line measurement at the 2.16 keV (Nb-L) did show a dip. The fluctuations in the EA ratio curves near the Ir M-edge in the 2.0–2.3 keV region are also due to the finite spectral resolution of the SSD.

In Figures 11.36–11.40, most of the FPC line data are below the SSD continuum data. Presently we do not know the exact cause of this. We hope to resolve this discrepancy as this work progresses.

Figures 11.36–11.40 can be accessed on the World Wide Web page:

[http://hea-www.harvard.edu/MST/mirror/www/xrcf/hrma\\_ea.html](http://hea-www.harvard.edu/MST/mirror/www/xrcf/hrma_ea.html)

at the beginning of the web page, please click:

Shell 1 Effective Area within 2 mm aperture

Shell 3 Effective Area within 2 mm aperture

Shell 4 Effective Area within 2 mm aperture

Shell 6 Effective Area within 2 mm aperture

HRMA Effective Area within 2 mm aperture

## 11.15 Calibrating the HRMA Effective Area

The XRCF HRMA effective area raytrace predictions were originally generated based on the HRMA model which is accurate to the best of our knowledge, including the HRMA tilt and decenter measured during the calibration. However, as we can see in the previous section, the calibration data show that for energies higher than 2 keV, the measured effective area is substantially less than the predicted effective area by well more than the experimental errors, especially for shell 1. At least part of this discrepancy is due to differences in the way the raytrace model calculates reflectivity, compared to our derivation of optical constants via our synchrotron measurements. There are also some discrepancies between the mirror surface roughness scattering model and the data measured from the wing scan measurements (see Chapter 14). We are currently assessing and correcting for these differences. For the present, based on the principle that theory should yield to the experiment, we use the XRCF calibration data to scale down the raytrace empirically for both on-orbit and XRCF HRMA effective area predictions.

In order to smooth the Poisson noise in the correction factor, a fourth order polynomial is used to fit the deficit curve of the effective area ratio between 2.3 keV and 10 keV. The polynomial fit curves for the four shells and the HRMA are plotted as solid curves in the bottom panels of Figures 11.36–11.40. These polynomials as functions of energy are to be used to scale the raytrace prediction. For higher energies where the effective area drops to below a few  $\text{cm}^2$  (i.e.  $\geq 6.7$  keV for shell 1,  $\geq 7.9$  keV for shell 3, and  $\geq 9.0$  keV for shell 4), there are not enough data to make a reasonable fit, and a ratio of unity is used.

Since the SSD data are not reliable for lower energies, FPC spectral line data for energies below 2.3 keV are used for scaling. The average ratios between the FPC data and the raytrace are used as the scaling factor. They are 1.0234, 0.9983, 0.9998, 1.0136, and 1.0055, for shells 1,3,4,6 and the HRMA, respectively.

The errors for the scaling factors are:

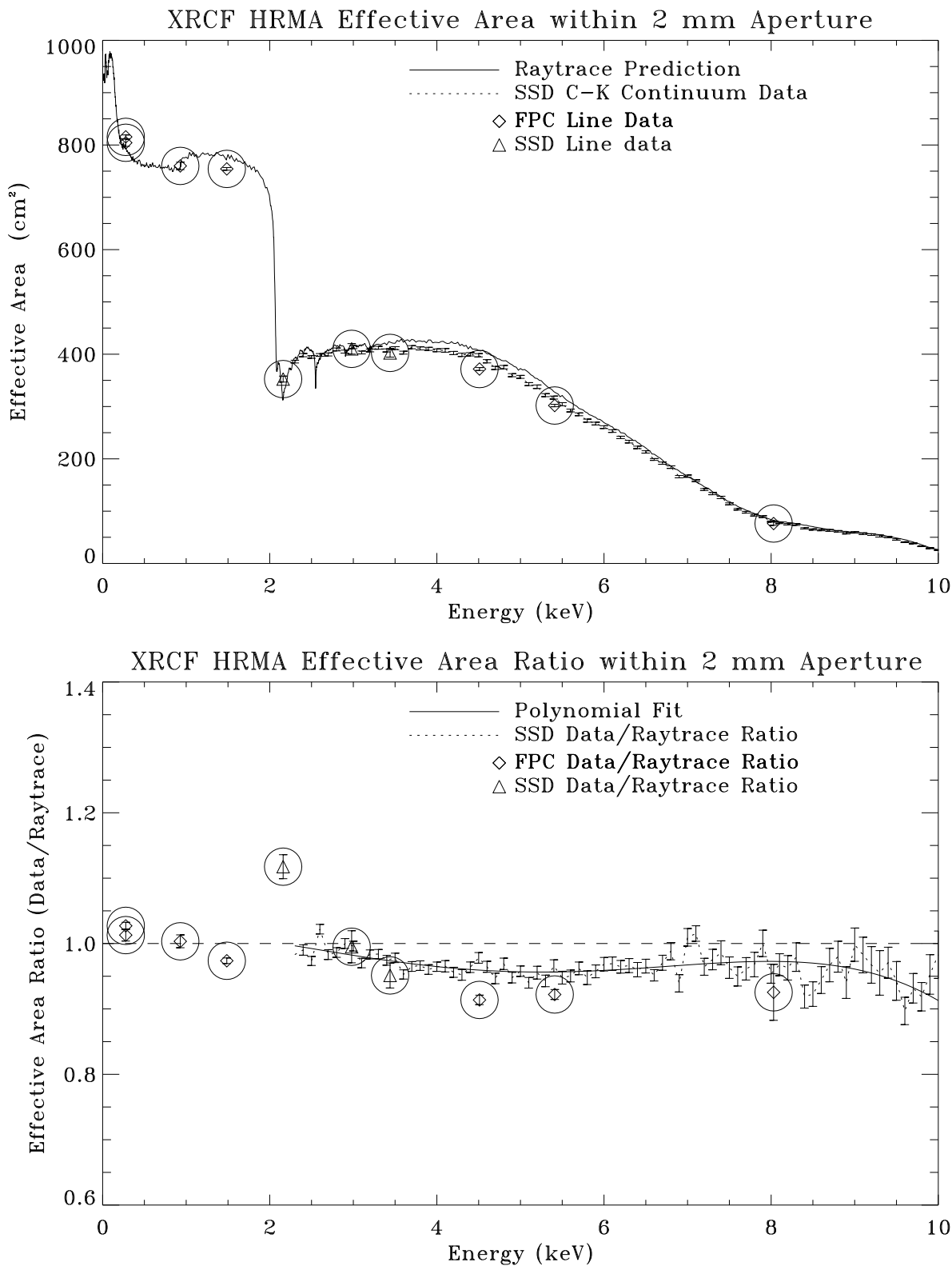


Figure 11.40: Calibration data vs. raytrace prediction. Top panel shows the XRCF HRMA effective area within 2 mm aperture. Bottom panel shows the effective area ratio of data/raytrace.

E < 2.3 keV:	FPC measurement errors	0.3–1.9%
	Deviations of the FPC data from the scaling factor	0.7–3.2%
	Statistical errors from raytrace simulation	<0.3%
	Total scaling factor errors	~1.1–3.4%
E ≥ 2.3 keV:	Standard deviation of the polynomial fit	1.7–3.3%
	Deviation of each data point from the polynomial fit	0.2–6.0%
	Statistical errors from raytrace simulation	<0.3%
	Total scaling factor errors	~2–7%

In the next three Sections we describe the raytrace predictions and the calibrated effective area at XRCF and on-orbit cases.

## 11.16 HRMA Effective Area Raytrace Predictions

The original raytrace predictions of the HRMA effective area for both the on-orbit and at XRCF cases were generated based on the HRMA model. The HRMA model includes mirror tilts and decenters measured at Kodak and XRCF, mirror low frequency surface maps from the HDOS metrology measurements, mirror CAP, pre- and post-collimators, apertures, ghost baffles, and mirror distortion due to epoxy cure shrinkage. For the XRCF case, the HRMA model also includes the finite source distance at the XRCF and the mirror distortion due to gravity.

The reflectivities are based on:<sup>5</sup>

E < 2 keV: Gullikson '95 optical constant table. (Henke et al., 1993)

E ≥ 2 keV: AXAF mirror witness flat synchrotron measurements made by Graessle et al. (Graessle et al., 1997)

The mirror surface roughness scattering is based on the Power Spectral Density (PSD) produced from the HDOS metrology measurements and calculated with a program “foldw1” written by Leon Van Speybroeck, which is based on the scattering theory by Beckmann and Spizzichino. (Beckmann and Spizzichino, 1963)

The XRCF HRMA trace-shell configuration file can be found at

[http://hea-www.harvard.edu/MST/simul/raytrace/databases/ts\\_config/00Index.html#xrcf\\_SAO1G+HDOS\\_HDOS-scat-980623\\_01](http://hea-www.harvard.edu/MST/simul/raytrace/databases/ts_config/00Index.html#xrcf_SAO1G+HDOS_HDOS-scat-980623_01)

The on-orbit HRMA trace-shell configuration file can be found at

[http://hea-www.harvard.edu/MST/simul/raytrace/databases/ts\\_config/00Index.html#orbit\\_HDOS+HATS+XRCF\\_scat-980623\\_01](http://hea-www.harvard.edu/MST/simul/raytrace/databases/ts_config/00Index.html#orbit_HDOS+HATS+XRCF_scat-980623_01)

Figures 11.41–11.45 show the raytrace predicted effective areas and encircled energies of the four shells and the HRMA at the XRCF. The top panels shows the effective area curves within 2 mm, 35 mm diameter apertures, and  $2\pi$  steradians. The bottom panels show the encircled energies of 2 mm and 35 mm apertures as fractions of that within  $2\pi$  steradians.

Figures 11.46–11.50 show the raytrace predicted effective areas and encircled energies of the four shells and the HRMA on-orbit.

The purpose of showing these figures is to compare the encircled energy curves between the XRCF and the on-orbit cases.

<sup>5</sup>Because we used different optical constant tables for E < 2 keV and E ≥ 2 keV for the raytracing, there is a discontinuity at 2 keV in all the raytrace effective area curves. Obviously this discontinuity is not real and the optical constant in two tables should agree at 2 keV. We are currently working to resolve this discrepancy.

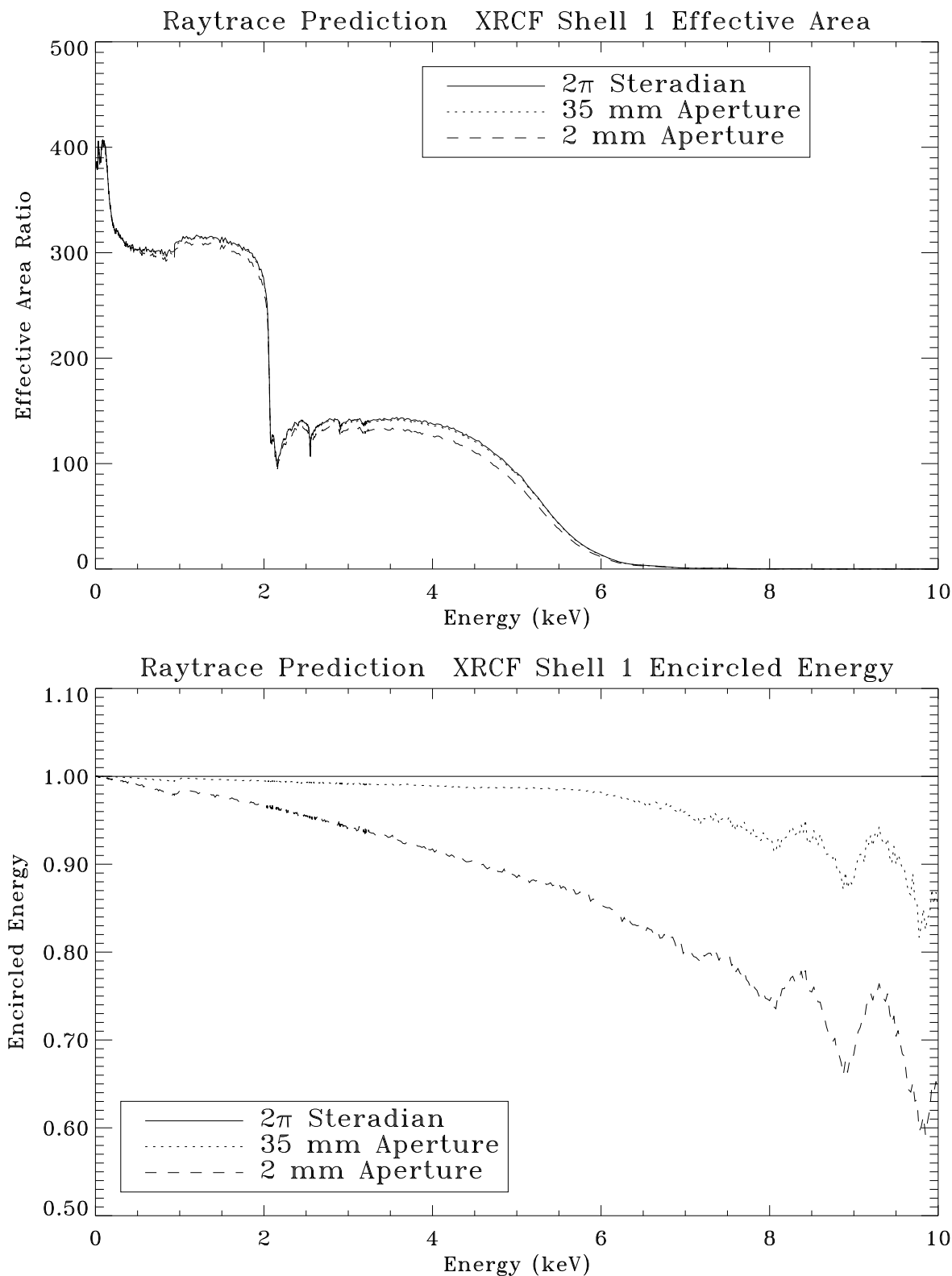


Figure 11.41: Raytrace prediction of XRCF Shell 1 effective area and encircled energy. Top panel shows the effective area curves within 2 mm, 35 mm apertures, and  $2\pi$  steradian. Bottom panel shows the encircled energies of 2 mm and 35 mm apertures as fractions of that within  $2\pi$  steradian.

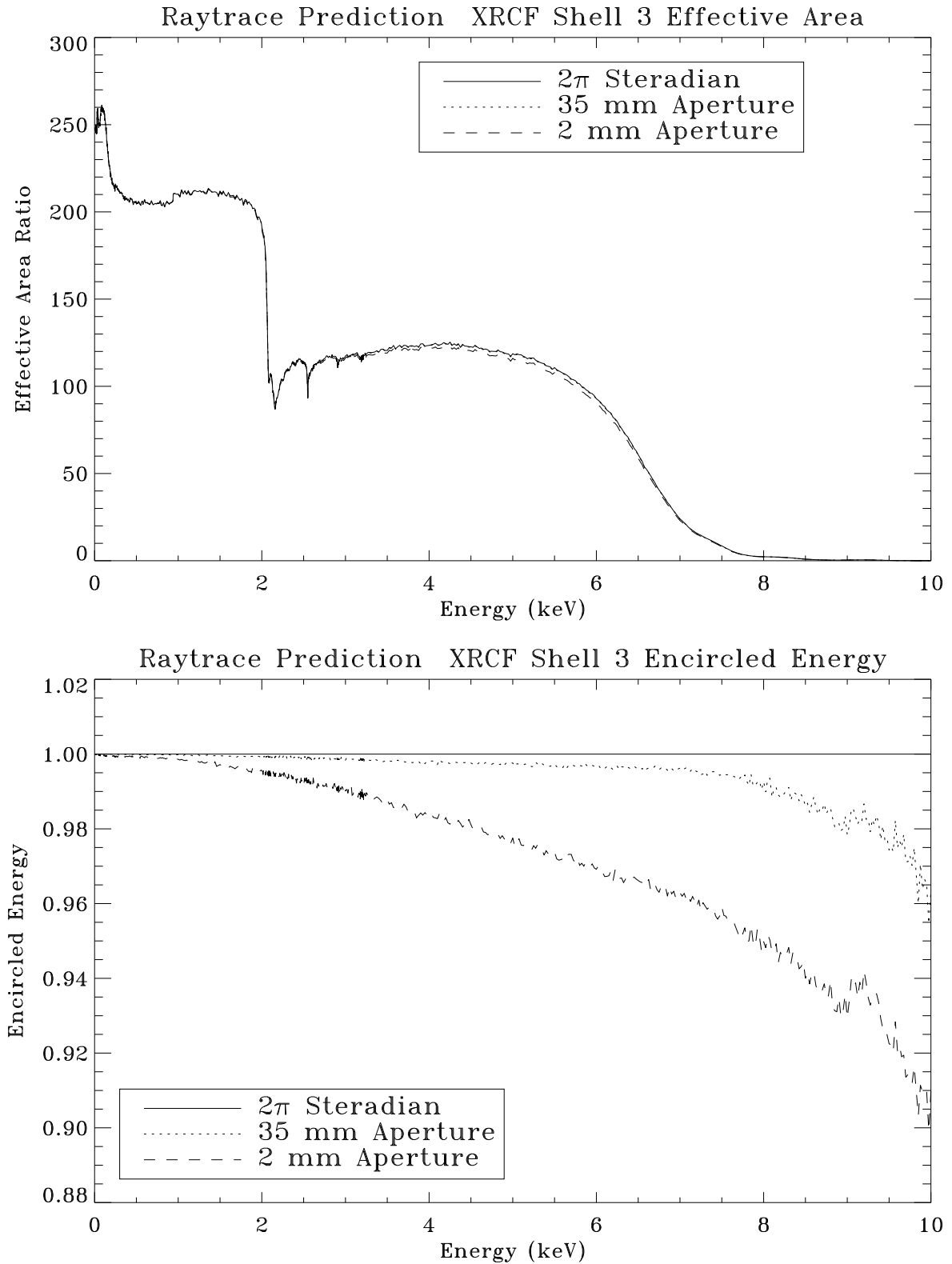


Figure 11.42: Raytrace prediction of XRCF Shell 3 effective area and encircled energy. Top panel shows the effective area curves within 2 mm, 35 mm apertures, and  $2\pi$  steradian. Bottom panel shows the encircled energies of 2 mm and 35 mm apertures as fractions of that within  $2\pi$  steradian.

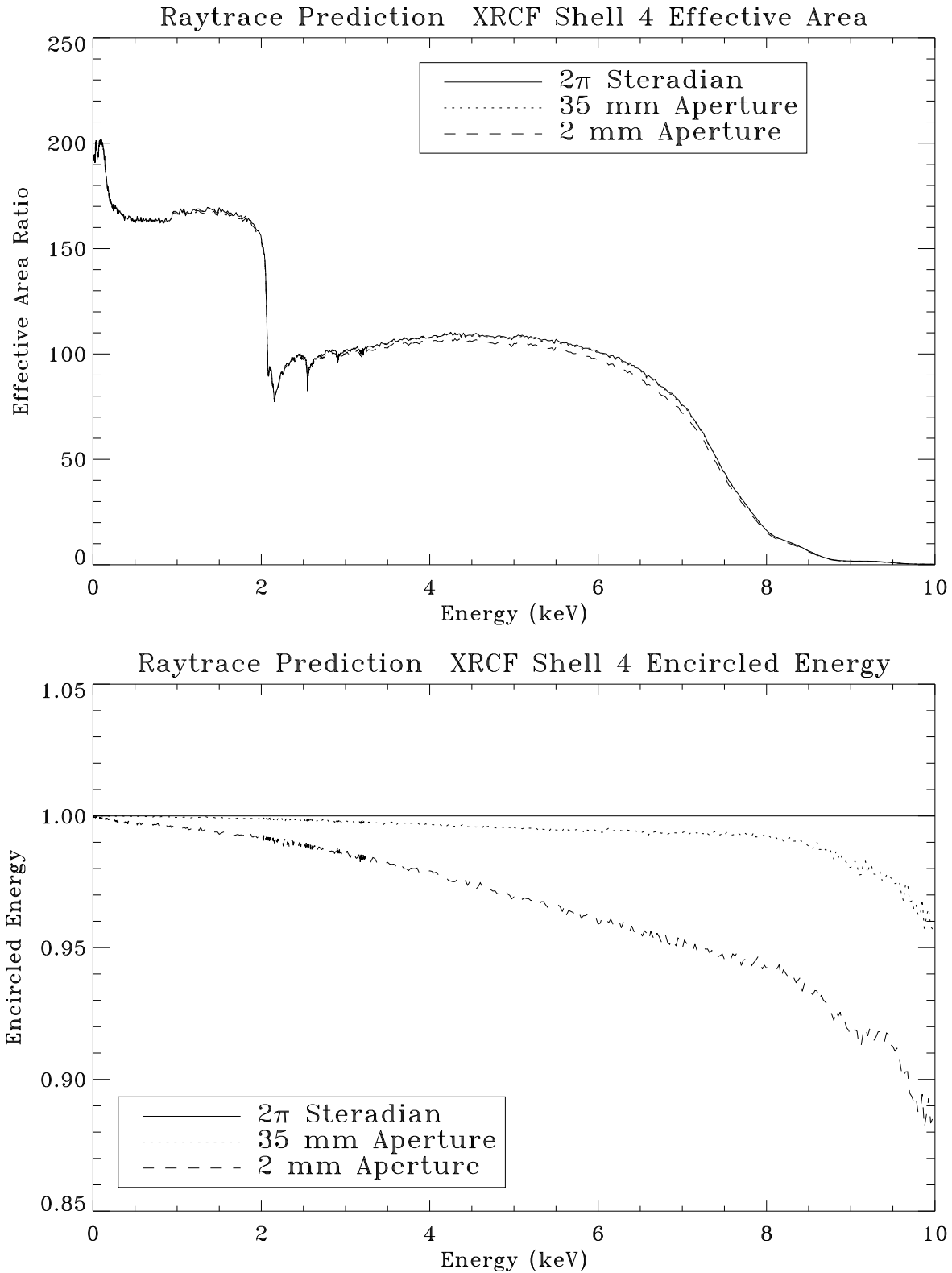


Figure 11.43: Raytrace prediction of XRCF Shell 4 effective area and encircled energy. Top panel shows the effective area curves within 2 mm, 35 mm apertures, and  $2\pi$  steradian. Bottom panel shows the encircled energies of 2 mm and 35 mm apertures as fractions of that within  $2\pi$  steradian.

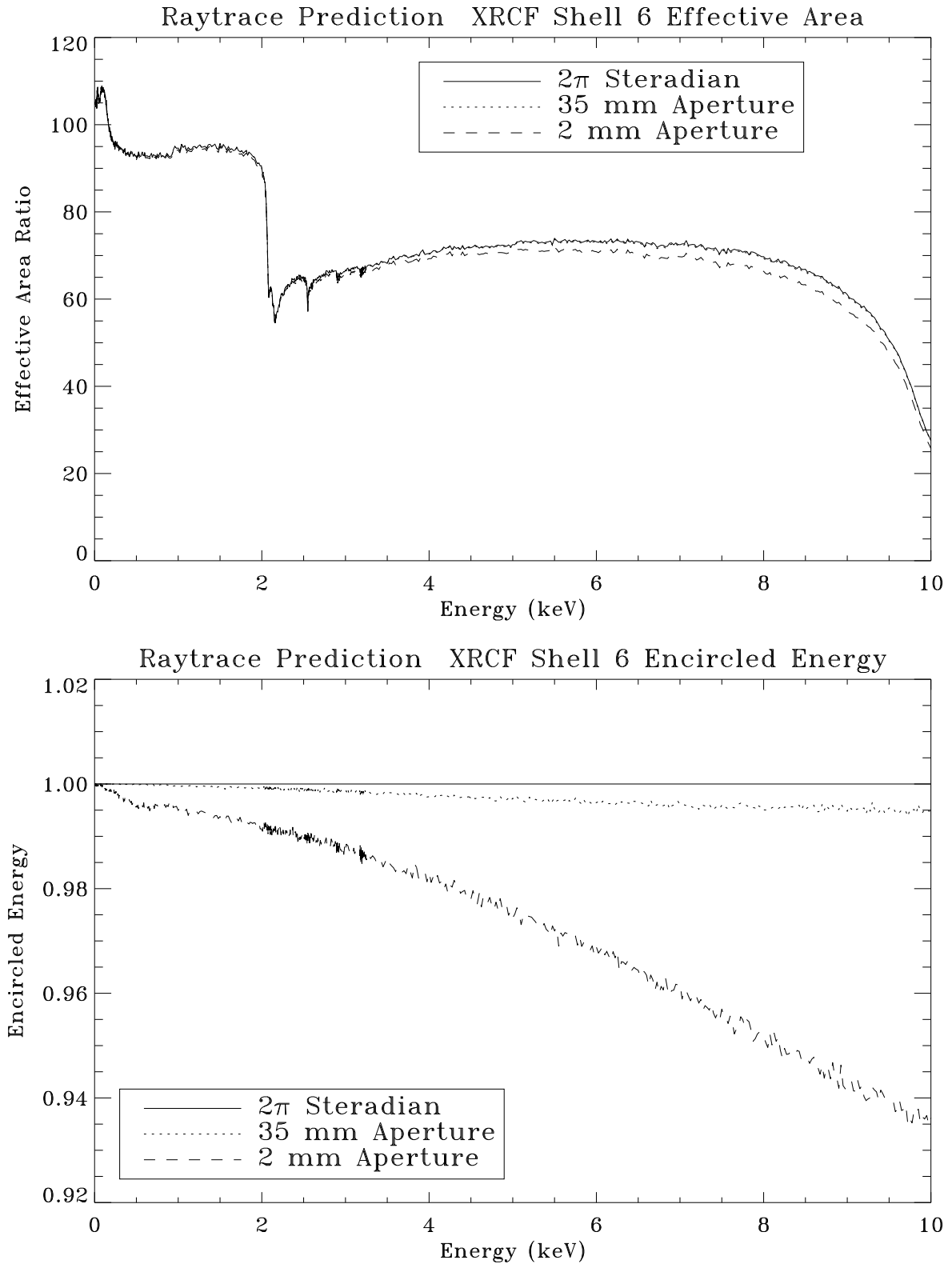


Figure 11.44: Raytrace prediction of XRCF Shell 6 effective area and encircled energy. Top panel shows the effective area curves within 2 mm, 35 mm apertures, and  $2\pi$  steradian. Bottom panel shows the encircled energies of 2 mm and 35 mm apertures as fractions of that within  $2\pi$  steradian.

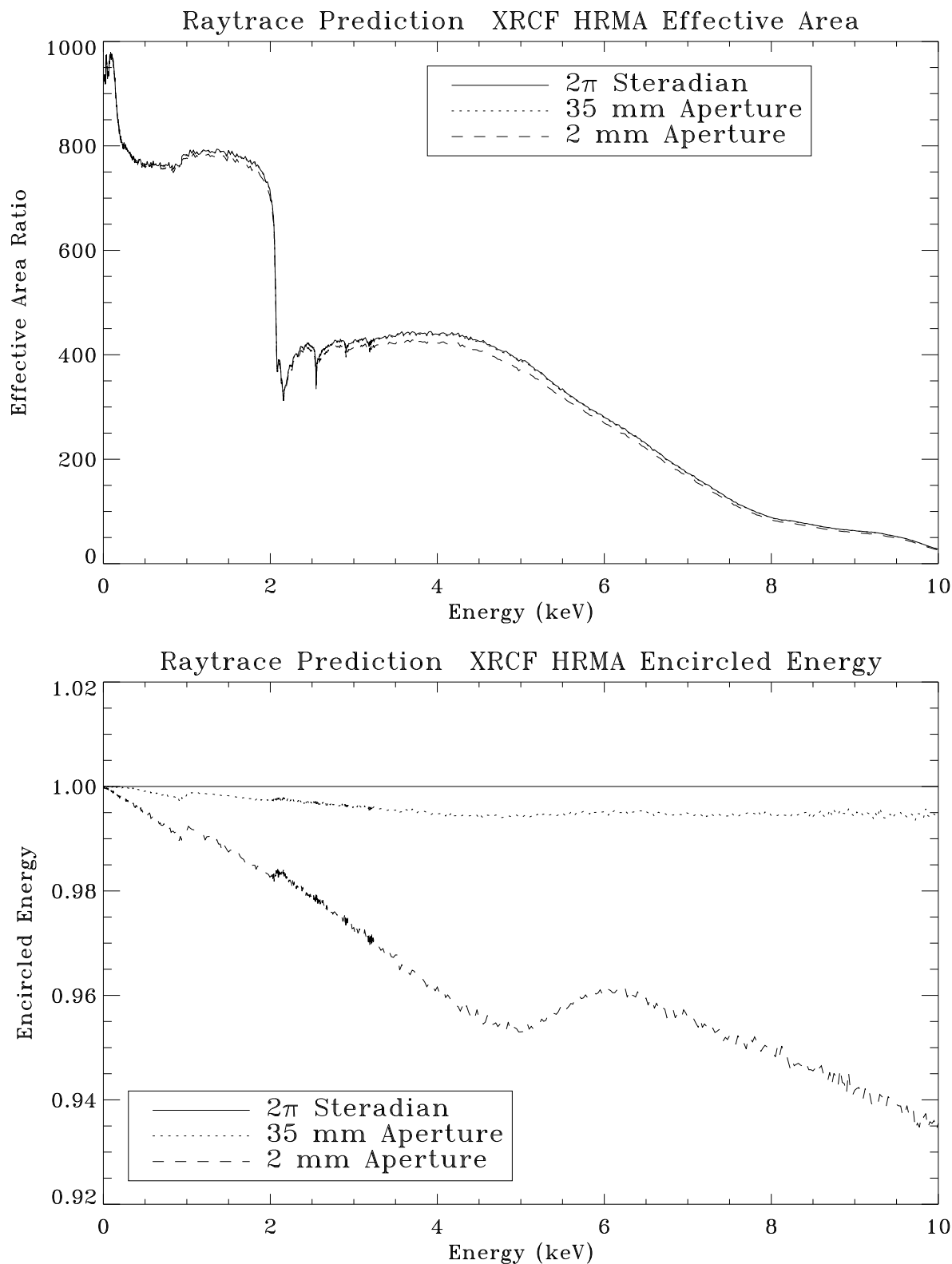


Figure 11.45: Raytrace prediction of XRCF HRMA effective area and encircled energy. Top panel shows the effective area curves within 2 mm, 35 mm apertures, and  $2\pi$  steradian. Bottom panel shows the encircled energies of 2 mm and 35 mm apertures as fractions of that within  $2\pi$  steradian.

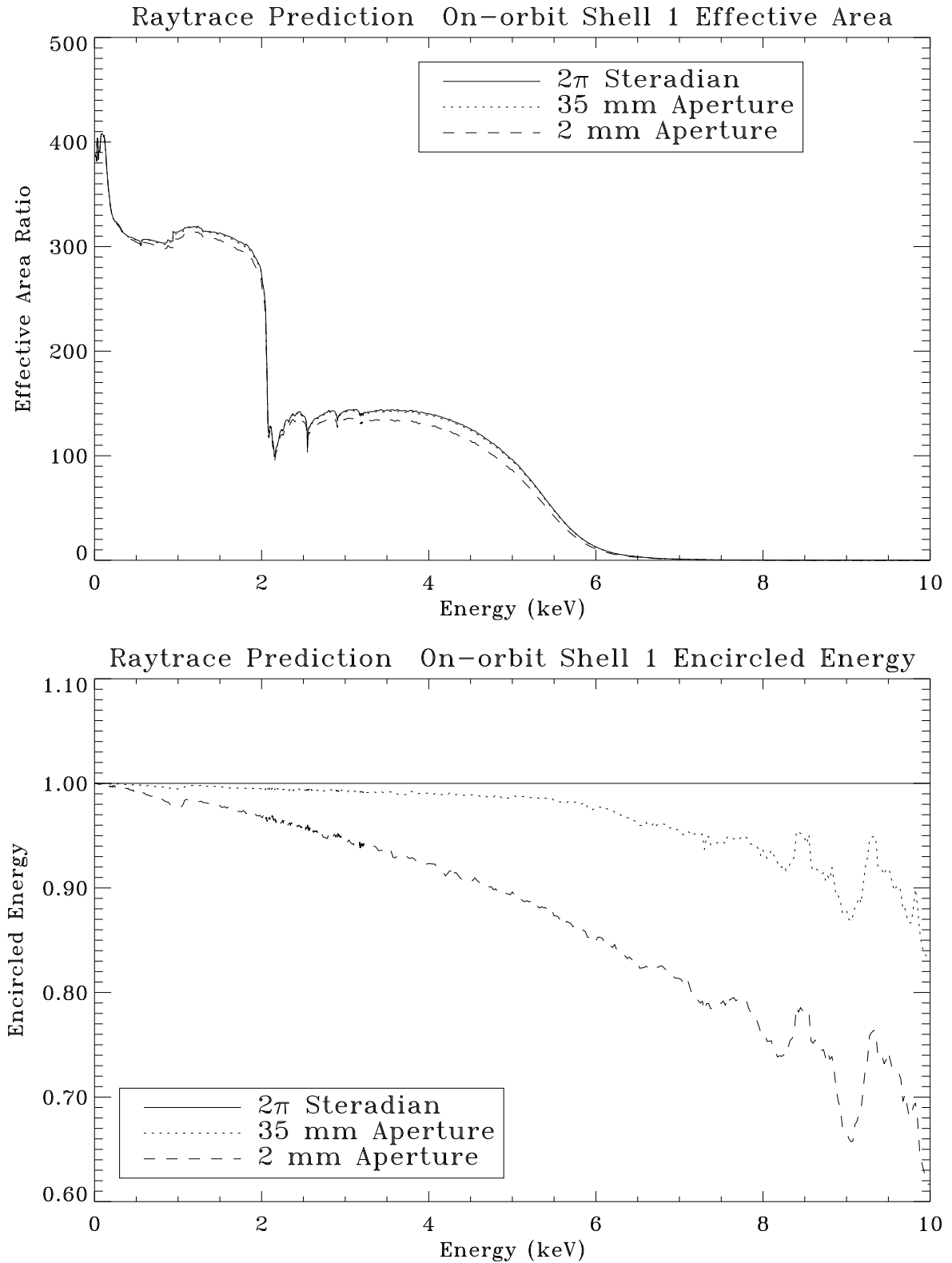


Figure 11.46: Raytrace prediction of on-orbit Shell 1 effective area and encircled energy. Top panel shows the effective area curves within 2 mm, 35 mm apertures, and  $2\pi$  steradian. Bottom panel shows the encircled energies of 2 mm and 35 mm apertures as fractions of that within  $2\pi$  steradian.

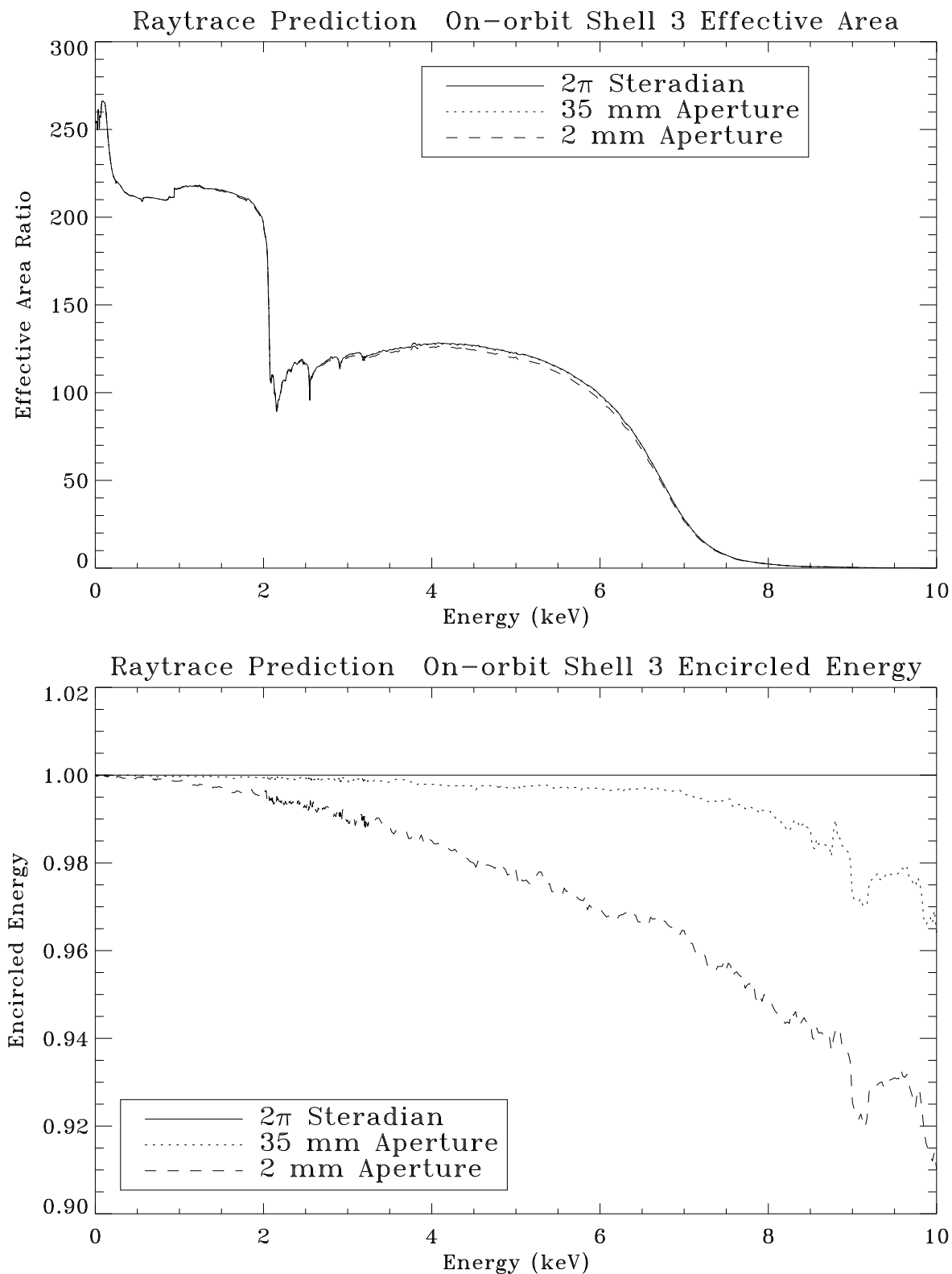


Figure 11.47: Raytrace prediction of on-orbit Shell 3 effective area and encircled energy. Top panel shows the effective area curves within 2 mm, 35 mm apertures, and  $2\pi$  steradian. Bottom panel shows the encircled energies of 2 mm and 35 mm apertures as fractions of that within  $2\pi$  steradian.

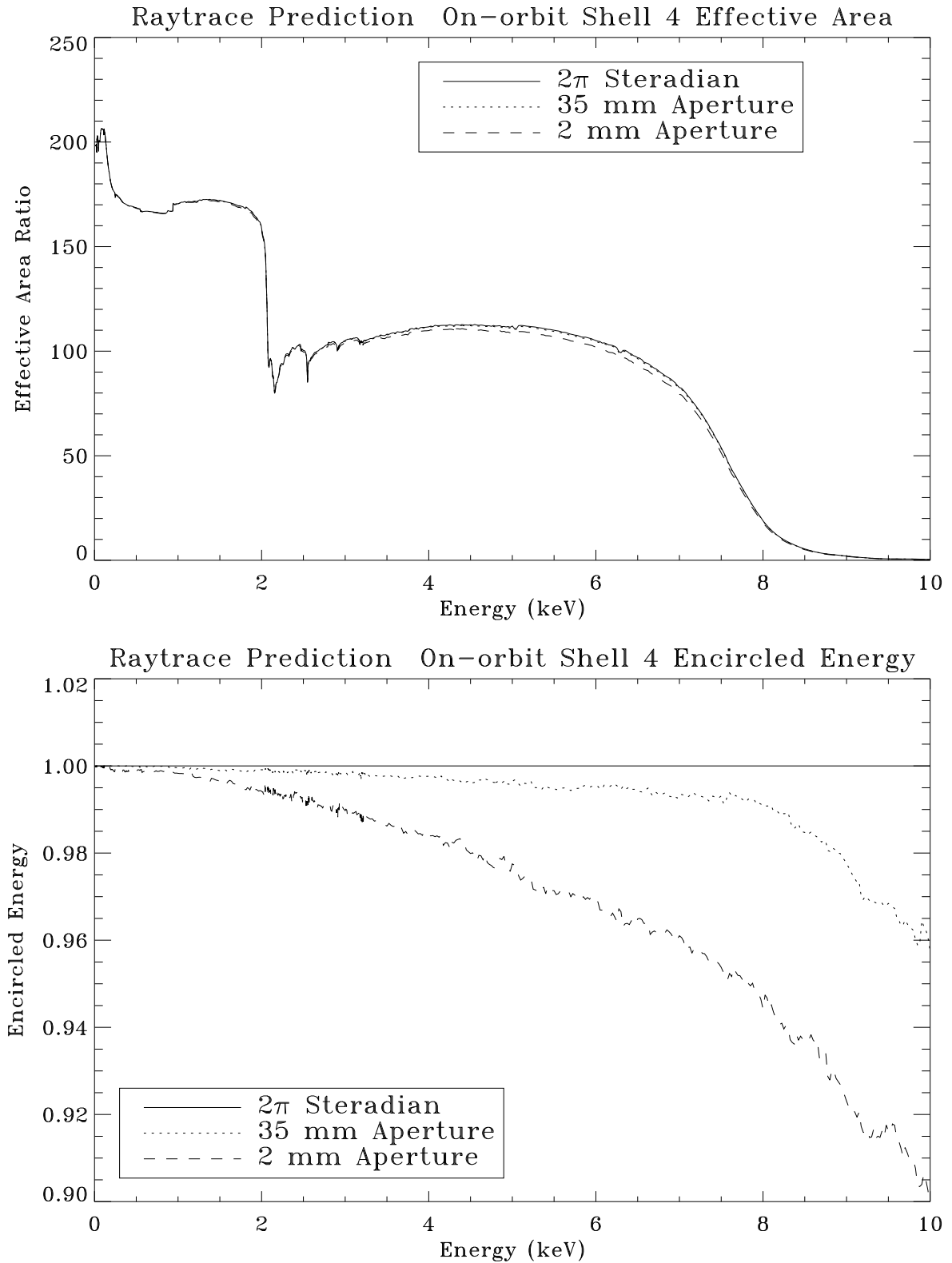


Figure 11.48: Raytrace prediction of on-orbit Shell 4 effective area and encircled energy. Top panel shows the effective area curves within 2 mm, 35 mm apertures, and  $2\pi$  steradian. Bottom panel shows the encircled energies of 2 mm and 35 mm apertures as fractions of that within  $2\pi$  steradian.

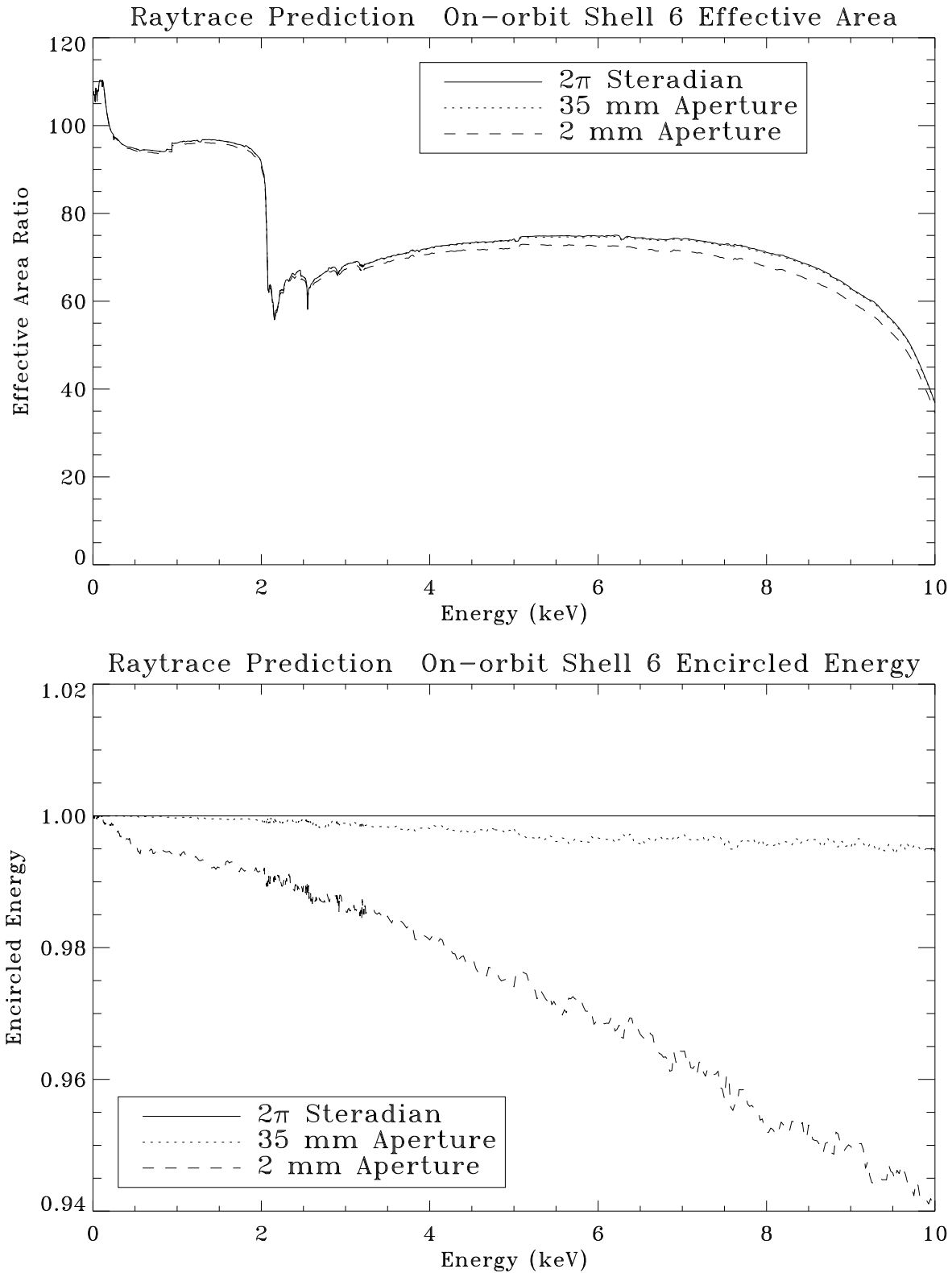


Figure 11.49: Raytrace prediction of on-orbit Shell 6 effective area and encircled energy. Top panel shows the effective area curves within 2 mm, 35 mm apertures, and  $2\pi$  steradian. Bottom panel shows the encircled energies of 2 mm and 35 mm apertures as fractions of that within  $2\pi$  steradian.

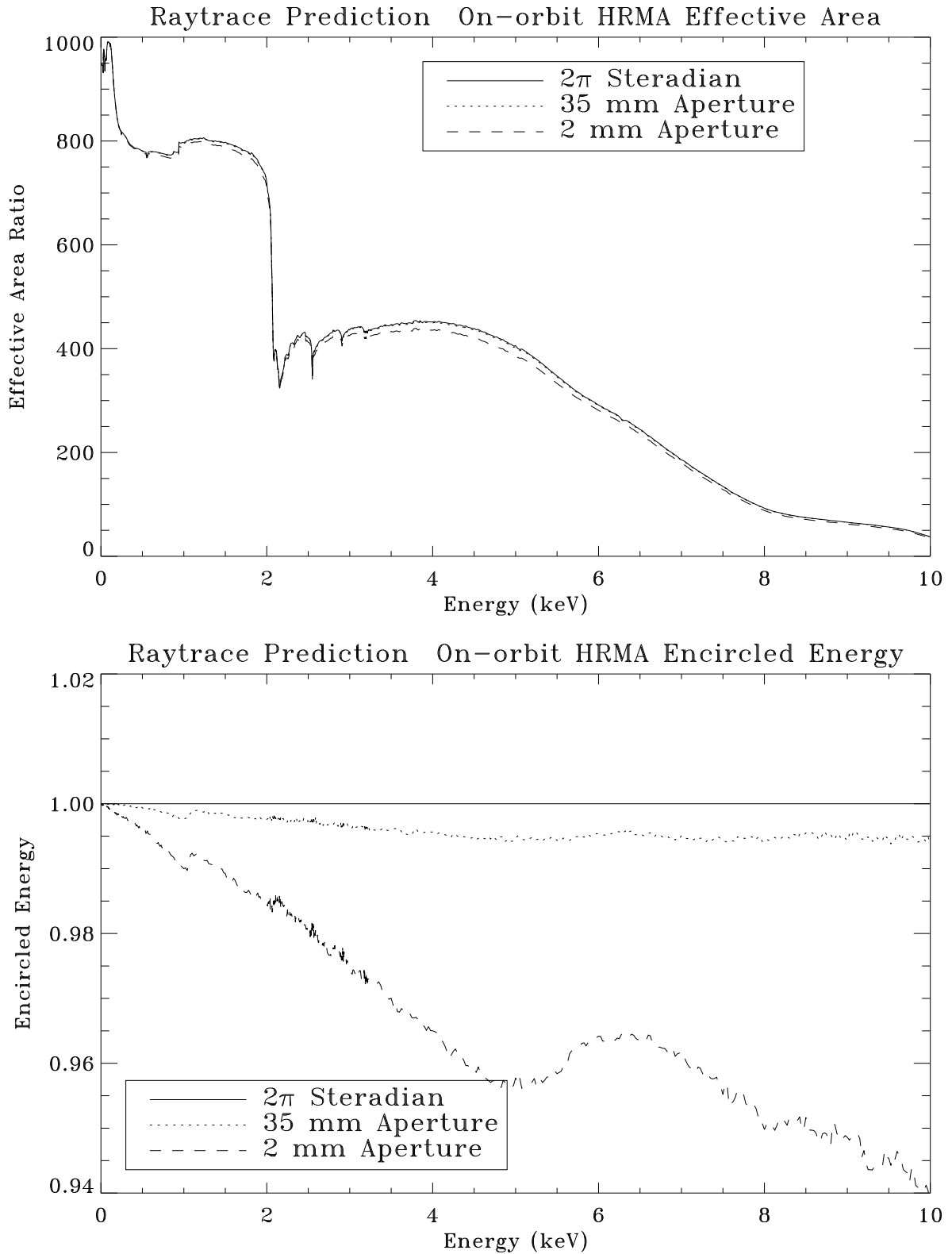


Figure 11.50: Raytrace prediction of on-orbit HRMA effective area and encircled energy. Top panel shows the effective area curves within 2 mm, 35 mm apertures, and  $2\pi$  steradian. Bottom panel shows the encircled energies of 2 mm and 35 mm apertures as fractions of that within  $2\pi$  steradian.

Since the SSD C-continuum effective area data we reduced are for only 2 mm aperture, we should be able to use these data to scale down the raytrace predicted XRCF effective area curve within 2 mm diameter. How about the XRCF effective area within larger apertures and  $2\pi$  steradians? How about the on-orbit cases? Can we use the XRCF 2 mm aperture measurement to scale down other effective area curves the same way?

Let's first look at the XRCF cases. The fractional encircled energy within 2 mm aperture varies as a function of energy and from shell to shell. For shell 1 at 6.5 keV, it can be as low as 86% (see Figure 11.41). For other shells, the fractional encircled energy curve are all higher than 92%. Can we use the 2 mm aperture data to scale down the effective area within larger apertures and  $2\pi$  steradians? The short answer is "we don't know", because we still don't know the exact cause or causes of the discrepancy between the data and the model. But we have some FPC spectral line measurements using the 35 mm diameter aperture (see Chapter 3). The data disagree with the raytrace prediction by about the same amount as the 2 mm aperture data did. As we can see the fractional encircled energy within 35 mm aperture are more than 99% for almost all the shells and all energies (see Figures 11.41–11.45). Therefore with good confidence we should be able to use the 2 mm aperture data scale down the XRCF effective area within larger apertures as well as within the  $2\pi$  steradians.

Next let's look at the on-orbit cases. The effective area and fractional encircled energy curves are very similar to the same curves for the XRCF cases. Therefore we can, with the same confident level, scale down the on-orbit HRMA effective area prediction curve the same way as for the XRCF cases.

Therefore, we will use the 2 mm aperture calibration data to scale down the raytrace predicted effective areas within any apertures greater or equal to 2 mm diameter for both on-orbit and at XRCF cases.

## 11.17 XRCF HRMA Effective Area

Figures 11.51–11.53 show the XRCF HRMA and four shells effective areas within 2 mm, 35 mm diameters and  $2\pi$  steradians, for the original raytrace and the calibrated curves with errors estimated in §11.15. Tables 11.7 – 11.9 list the values of the XRCF effective areas with energy grid of 0.1 keV.<sup>6</sup> The "rdb" tables on the web (see below) have denser energy grid.

These are our current best estimates for the HRMA effective area at the XRCF. Other calibration teams can use these data to calibrate their instruments. The "rdb" tables of the XRCF HRMA effective area, as well as Figures 11.51–11.53, can be accessed on the World Wide Web page:

[http://hea-www.harvard.edu/MST/mirror/www/xrcf/hrma\\_ea.html](http://hea-www.harvard.edu/MST/mirror/www/xrcf/hrma_ea.html)

at the bottom of the web page, please click:

[XRCF HRMA Effective Area within 2 mm aperture and its figure.](#)

[XRCF HRMA Effective Area within 35 mm aperture and its figure.](#)

[XRCF HRMA Effective Area within 2pi steradians and its figure.](#)

---

<sup>6</sup>Careful readers will notice that the effective area of four shells do not exactly add up to the HRMA effective area listed in the tables. This is because, when generating these tables, we used polynomial curves to fit the deficit curve of the effective area ratio of the four shells and of the HRMA to smooth our the noise. This process produces the small discrepancy as seen here. However, the discrepancy is only 1-2% and well within the quoted errors.

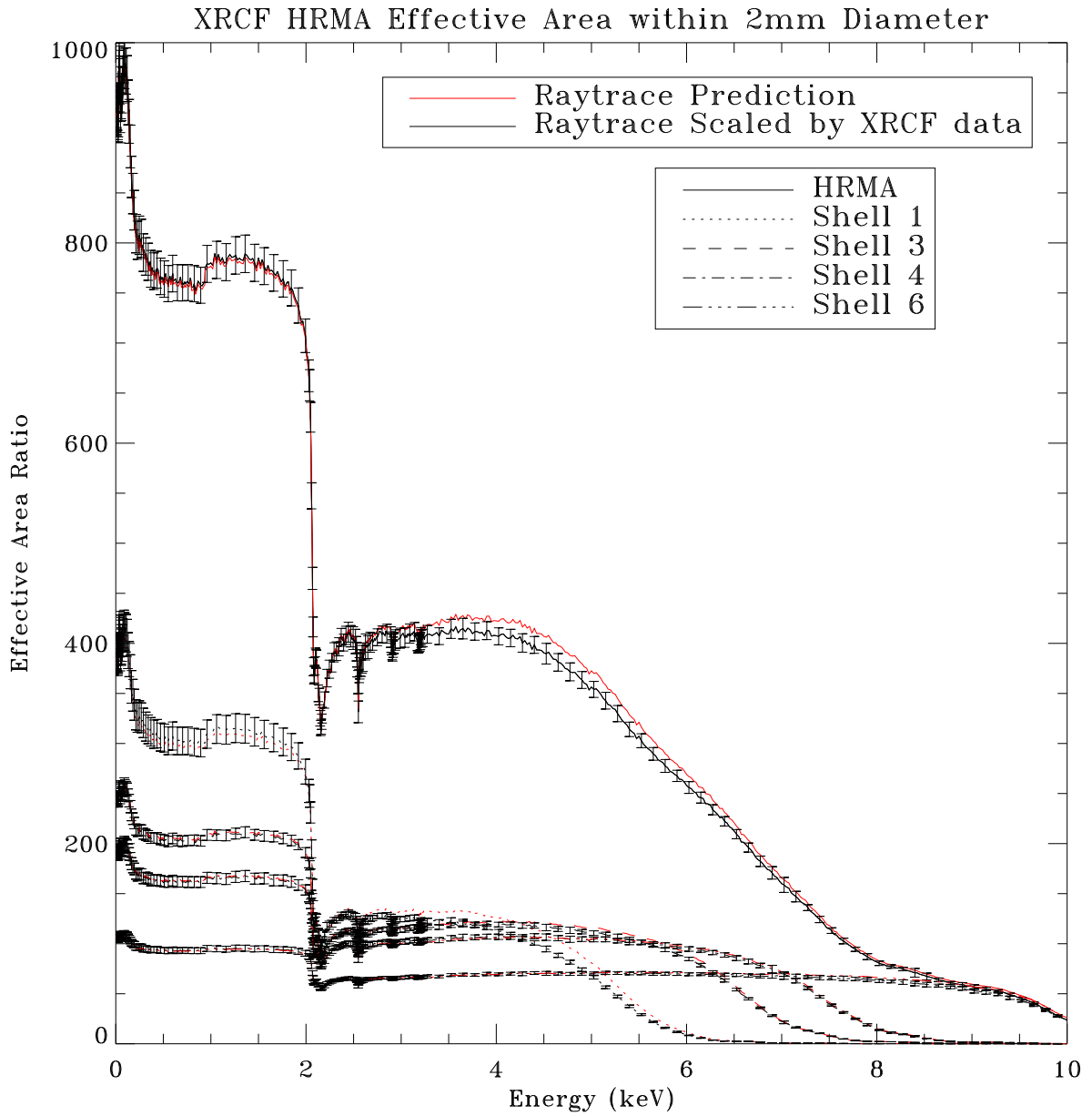


Figure 11.51: The XRCF HRMA and four shells effective areas within 2 mm aperture. The original raytrace predictions and the calibration data scaled raytrace predictions.

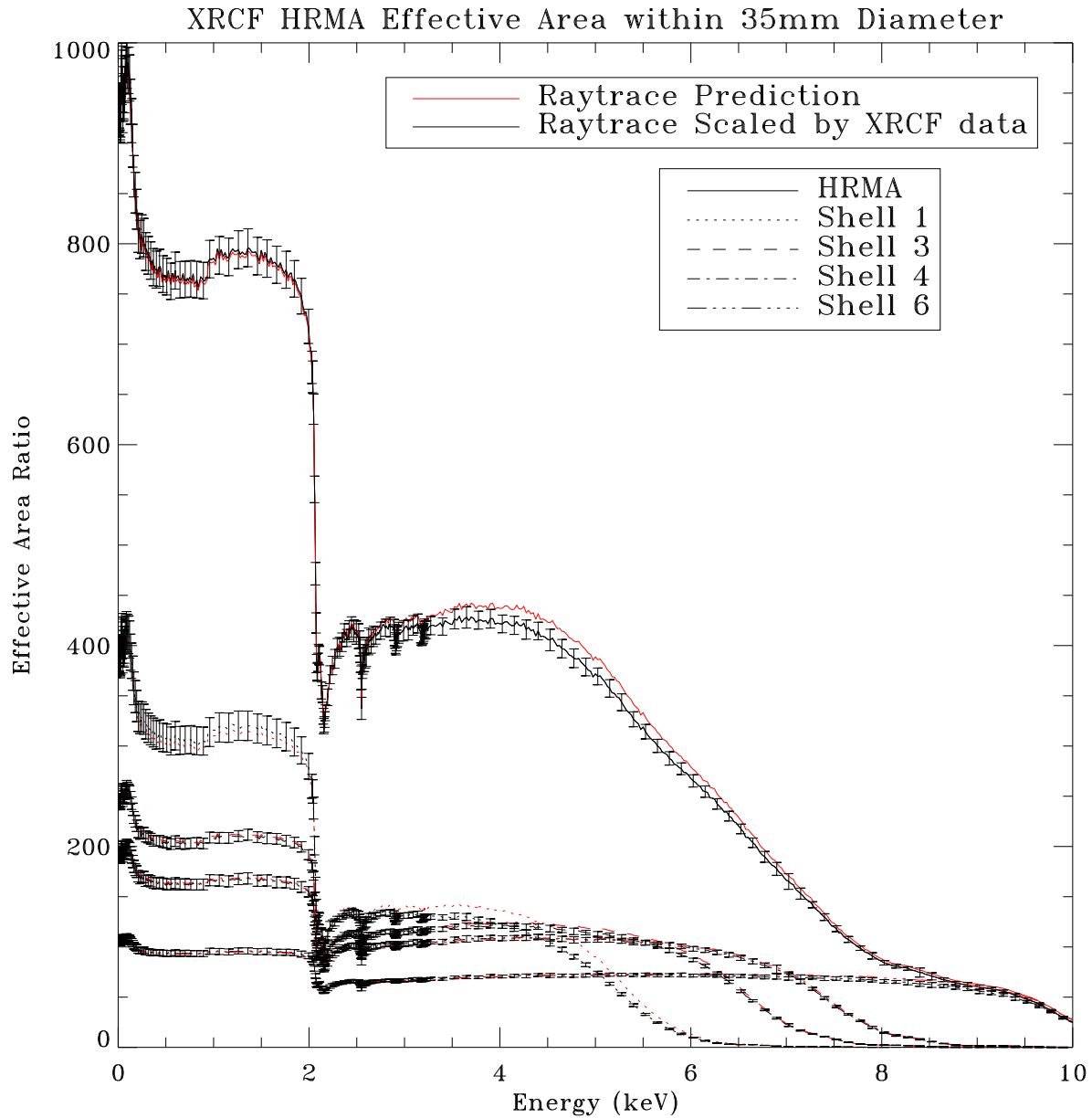


Figure 11.52: The XRCF HRMA and four shells effective areas within 35 mm aperture. The original raytrace predictions and the calibration data scaled raytrace predictions.

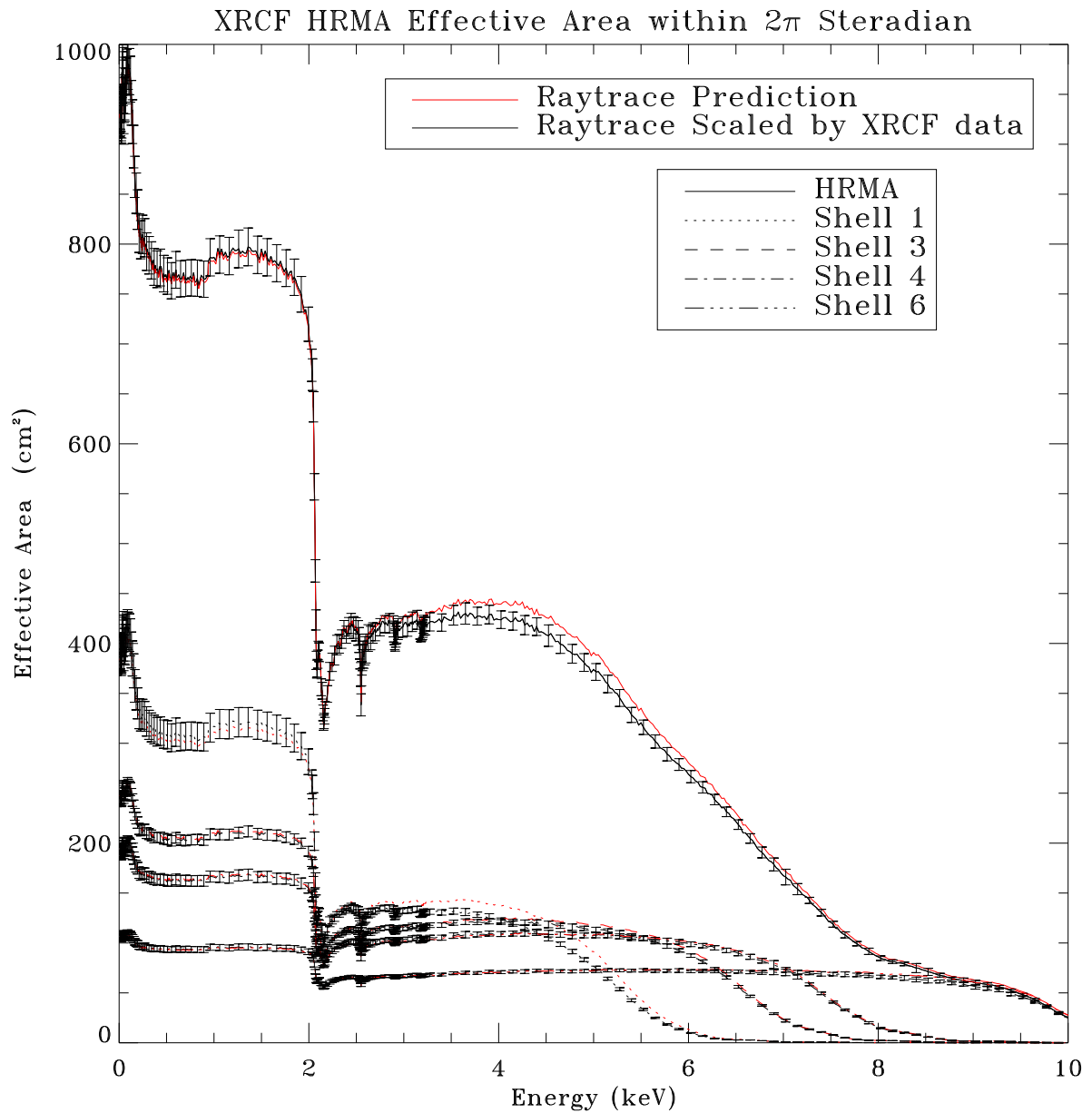


Figure 11.53: The XRCF HRMA and four shells effective areas within  $2\pi$  steradian. The original raytrace predictions and the calibration data scaled raytrace predictions.

Table 11.7: XRCF HRMA Effective Area within 2 mm Aperture. Units: cm<sup>2</sup>

Energy (keV)	Shell 1		Shell 3		Shell 4		Shell 6		HRMA	
	$A_{eff}$	Error								
0.10	413.70	11.68	257.57	2.90	199.79	6.71	108.90	2.90	974.86	15.63
0.20	338.44	9.56	219.28	2.47	173.26	5.82	97.95	2.61	824.80	13.22
0.30	324.28	9.16	211.96	2.39	168.09	5.64	95.75	2.55	796.13	12.76
0.40	314.85	8.89	207.16	2.33	164.66	5.53	94.29	2.51	777.14	12.46
0.50	311.89	8.81	205.79	2.32	163.69	5.50	93.82	2.50	771.40	12.37
0.60	312.13	8.81	206.11	2.32	163.91	5.50	93.95	2.51	772.31	12.38
0.70	311.07	8.78	205.76	2.32	163.66	5.49	93.89	2.50	770.61	12.35
0.80	309.10	8.73	204.92	2.31	163.11	5.48	93.67	2.50	767.06	12.30
0.90	311.13	8.79	206.23	2.32	164.01	5.51	94.08	2.51	771.69	12.37
1.00	310.91	8.78	206.37	2.32	164.09	5.51	94.11	2.51	771.70	12.37
1.10	310.81	8.78	206.59	2.33	164.26	5.51	94.22	2.51	772.12	12.38
1.20	309.77	8.75	206.36	2.32	164.14	5.51	94.17	2.51	770.69	12.35
1.30	308.27	8.71	205.87	2.32	163.82	5.50	94.07	2.51	768.31	12.32
1.40	306.12	8.65	205.08	2.31	163.31	5.48	93.87	2.50	764.69	12.26
1.50	302.93	8.56	203.86	2.30	162.51	5.46	93.56	2.50	759.21	12.17
1.60	298.93	8.44	202.13	2.28	161.28	5.41	93.08	2.48	751.82	12.05
1.70	293.10	8.28	199.48	2.25	159.49	5.35	92.36	2.46	740.92	11.88
1.80	284.30	8.03	195.28	2.20	156.65	5.26	91.21	2.43	724.03	11.61
1.90	268.38	7.58	187.51	2.11	151.30	5.08	89.00	2.37	693.01	11.11
2.00	244.30	6.90	175.51	1.98	143.06	4.80	85.59	2.28	645.58	10.35
2.10	128.98	3.64	108.01	1.22	94.03	3.16	63.29	1.69	392.87	6.30
2.20	115.99	3.28	98.58	1.11	86.55	2.91	59.40	1.58	359.23	5.76
2.30	123.30	4.28	107.20	2.97	96.11	2.34	63.19	1.34	392.21	10.01
2.40	126.41	4.19	109.99	2.75	98.26	2.27	64.22	1.13	400.53	8.14
2.50	126.07	4.64	110.65	3.06	98.78	2.59	64.53	1.52	400.95	10.11
2.60	120.46	5.66	107.32	4.05	96.13	3.26	63.26	1.74	387.35	13.14
2.70	125.95	4.40	111.92	2.83	99.71	2.69	65.00	1.13	402.36	8.38
2.80	127.71	4.30	114.10	2.85	101.40	2.35	65.85	1.27	408.38	8.01
2.90	122.99	4.65	112.02	2.86	99.91	2.74	65.26	1.15	399.05	9.67
3.00	125.05	4.39	114.22	3.67	101.63	2.79	66.07	1.64	405.65	11.00
3.10	125.80	5.17	115.82	3.84	102.90	2.95	66.76	1.67	409.79	10.50
3.20	121.65	4.31	113.91	3.03	101.55	2.57	66.22	1.21	401.69	9.53
3.30	122.98	4.23	115.97	3.07	103.18	2.46	67.06	1.74	407.54	9.30
3.40	122.61	4.59	116.92	3.04	104.02	2.90	67.53	1.17	409.47	8.49
3.50	122.19	4.29	117.89	2.99	104.88	2.45	68.06	1.32	411.56	8.20
3.60	120.45	5.24	117.95	3.80	105.08	3.62	68.26	1.62	410.47	11.30
3.70	119.26	4.23	118.47	2.97	105.72	2.47	68.67	1.31	411.06	8.52
3.80	117.71	4.19	118.81	3.16	106.16	2.50	69.01	1.21	410.96	8.23
3.90	115.31	4.21	118.65	2.99	106.26	2.51	69.17	1.27	409.01	8.27
4.00	113.00	4.09	118.72	3.06	106.55	2.54	69.45	1.28	407.68	8.20
4.10	111.55	4.28	119.70	3.06	107.61	2.54	70.11	1.22	409.40	8.53
4.20	108.31	4.16	119.06	3.29	107.41	2.56	70.17	1.23	405.80	8.98
4.30	104.54	3.89	118.28	3.18	107.08	2.54	70.15	1.54	401.36	8.56

Table 11.7: XRCF HRMA Effective Area within 2 mm Aperture. Units: cm<sup>2</sup> (continued)

Energy (keV)	Shell 1		Shell 3		Shell 4		Shell 6		HRMA	
	$A_{eff}$	Error								
4.40	101.42	3.83	118.23	3.25	107.33	2.76	70.45	1.29	399.21	8.11
4.50	97.13	3.81	117.26	3.54	106.95	3.08	70.45	1.73	393.98	8.87
4.60	92.14	3.54	116.02	3.20	106.36	2.54	70.38	1.29	387.44	7.95
4.70	85.36	3.28	115.29	3.13	106.44	3.47	70.72	1.51	380.39	10.35
4.80	79.90	3.24	114.16	3.40	105.99	2.82	70.70	1.28	373.55	7.78
4.90	73.87	2.91	113.12	3.03	105.65	2.75	70.76	2.01	366.27	9.97
5.00	67.43	2.94	111.53	2.94	104.93	2.52	70.64	1.27	357.41	7.34
5.10	60.03	2.40	110.03	3.06	104.42	2.54	70.64	1.51	347.72	8.70
5.20	52.71	2.23	108.32	2.87	103.72	2.58	70.54	1.29	337.52	6.86
5.30	45.06	1.98	106.61	3.12	103.10	2.76	70.56	1.33	327.02	8.64
5.40	37.68	1.67	104.28	2.98	102.04	2.55	70.36	1.24	315.44	6.63
5.50	30.55	1.33	101.64	2.70	100.88	2.49	70.16	1.27	303.60	6.20
5.60	24.35	1.05	98.85	2.59	99.75	2.42	70.03	1.62	292.71	5.98
5.70	19.26	0.94	96.01	2.61	98.69	2.45	69.92	1.26	283.09	6.06
5.80	15.07	0.79	92.98	2.52	97.68	2.75	69.90	1.29	274.45	5.80
5.90	11.10	0.51	89.26	2.34	96.62	2.55	69.91	1.55	265.25	5.76
6.00	8.58	0.54	85.45	2.24	95.45	2.40	69.80	1.26	257.54	6.01
6.10	6.56	0.36	80.92	2.34	93.96	2.30	69.63	1.48	249.31	6.24
6.20	5.02	0.29	75.69	2.34	92.24	2.28	69.39	1.25	240.65	4.87
6.30	3.83	0.61	69.78	2.07	90.46	2.21	69.19	1.50	231.66	4.80
6.40	2.93	0.16	63.01	1.81	88.39	2.22	68.97	1.27	221.87	4.49
6.50	2.27	0.12	55.61	1.81	85.81	2.11	68.58	1.23	211.02	4.71
6.60	1.75	0.24	48.20	1.50	83.63	3.01	68.45	1.42	200.94	4.65
6.70	1.34	0.24	40.58	1.34	81.15	2.28	68.50	1.23	190.66	3.95
6.80	1.87	0.08	34.24	0.90	78.01	2.21	68.23	1.54	180.86	4.83
6.90	1.54	0.06	28.45	1.25	74.07	3.44	67.79	2.16	170.72	6.05
7.00	1.26	0.05	23.40	0.74	69.88	2.12	67.50	3.38	161.24	6.34
7.10	1.04	0.04	18.96	0.50	64.76	3.82	67.11	2.92	151.40	7.19
7.20	0.88	0.04	15.38	0.70	58.52	1.68	66.18	1.20	140.78	2.83
7.40	0.59	0.03	9.34	0.34	45.85	1.14	66.37	1.26	122.05	2.52
7.60	0.44	0.02	6.01	0.51	33.96	1.56	65.58	1.80	105.96	3.93
7.80	0.32	0.01	3.89	0.34	24.20	0.61	64.68	1.39	93.13	1.85
8.00	0.24	0.01	2.55	0.23	16.49	0.44	63.64	2.46	83.02	2.74
8.20	0.18	0.01	1.74	0.06	10.91	0.28	62.44	1.67	75.44	1.96
8.40	0.14	0.01	1.25	0.03	7.18	0.18	61.36	1.16	70.17	1.57
8.60	0.11	0.00	0.89	0.04	4.57	0.12	59.62	2.07	65.52	1.69
8.80	0.08	0.00	0.70	0.02	2.94	0.35	57.84	1.35	61.92	2.73
9.00	0.06	0.00	0.51	0.01	1.96	0.07	55.55	1.29	58.56	1.78
9.20	0.05	0.00	0.38	0.01	1.36	0.11	52.30	1.07	54.64	1.16
9.40	0.04	0.00	0.29	0.01	0.95	0.03	48.20	1.75	50.09	1.31
9.60	0.03	0.00	0.23	0.01	0.72	0.02	42.22	1.77	43.81	2.21
9.80	0.03	0.00	0.18	0.00	0.53	0.02	33.83	1.31	35.12	1.62
10.00	0.02	0.00	0.14	0.00	0.39	0.01	24.70	0.63	25.69	0.82

Table 11.8: XRCF HRMA Effective Area within 35 mm Aperture. Units: cm<sup>2</sup>

Energy (keV)	Shell 1		Shell 3		Shell 4		Shell 6		HRMA	
	$A_{eff}$	Error								
0.10	414.16	11.70	257.64	2.90	199.94	6.71	108.96	2.91	975.58	15.64
0.20	339.13	9.58	219.38	2.47	173.48	5.82	98.07	2.62	825.92	13.24
0.30	325.13	9.18	212.09	2.39	168.38	5.65	95.93	2.56	797.57	12.79
0.40	315.89	8.92	207.28	2.33	165.01	5.54	94.52	2.52	778.86	12.49
0.50	313.16	8.84	205.88	2.32	164.04	5.51	94.12	2.51	773.39	12.40
0.60	313.68	8.86	206.23	2.32	164.30	5.52	94.24	2.51	774.64	12.42
0.70	312.90	8.84	205.90	2.32	164.08	5.51	94.16	2.51	773.22	12.40
0.80	311.22	8.79	205.08	2.31	163.52	5.49	93.95	2.51	769.98	12.34
0.90	313.54	8.85	206.42	2.33	164.47	5.52	94.38	2.52	775.00	12.42
1.00	313.63	8.86	206.58	2.33	164.60	5.53	94.44	2.52	775.44	12.43
1.10	313.88	8.86	206.83	2.33	164.81	5.53	94.55	2.52	776.27	12.44
1.20	313.27	8.85	206.64	2.33	164.70	5.53	94.52	2.52	775.33	12.43
1.30	312.21	8.82	206.21	2.32	164.44	5.52	94.43	2.52	773.50	12.40
1.40	310.44	8.77	205.48	2.31	163.96	5.50	94.26	2.51	770.37	12.35
1.50	307.70	8.69	204.31	2.30	163.17	5.48	93.95	2.51	765.41	12.27
1.60	304.05	8.59	202.61	2.28	162.03	5.44	93.51	2.49	758.52	12.16
1.70	298.53	8.43	200.01	2.25	160.27	5.38	92.79	2.47	748.00	11.99
1.80	290.06	8.19	195.88	2.21	157.47	5.29	91.66	2.44	731.59	11.73
1.90	274.29	7.75	188.11	2.12	152.14	5.11	89.48	2.39	700.72	11.23
2.00	250.12	7.06	176.13	1.98	143.89	4.83	86.08	2.30	653.24	10.47
2.10	132.29	3.74	108.44	1.22	94.62	3.18	63.66	1.70	397.51	6.37
2.20	119.18	3.37	98.99	1.12	87.13	2.92	59.76	1.59	363.71	5.83
2.30	126.92	4.41	107.71	2.98	96.78	2.36	63.60	1.35	397.56	10.15
2.40	130.39	4.32	110.53	2.76	98.97	2.29	64.65	1.14	406.34	8.26
2.50	130.31	4.80	111.23	3.08	99.52	2.61	64.97	1.53	407.10	10.27
2.60	124.71	5.86	107.93	4.07	96.88	3.28	63.71	1.76	393.56	13.35
2.70	130.67	4.56	112.60	2.85	100.52	2.71	65.49	1.14	409.22	8.52
2.80	132.75	4.47	114.83	2.87	102.29	2.37	66.39	1.28	415.77	8.16
2.90	128.09	4.85	112.76	2.88	100.81	2.76	65.80	1.16	406.53	9.85
3.00	130.54	4.59	115.03	3.70	102.58	2.82	66.65	1.65	413.72	11.22
3.10	131.60	5.41	116.69	3.87	103.92	2.98	67.38	1.68	418.35	10.72
3.20	127.52	4.52	114.84	3.05	102.58	2.59	66.85	1.22	410.40	9.74
3.30	129.23	4.45	116.94	3.10	104.32	2.48	67.73	1.76	416.87	9.51
3.40	129.15	4.83	117.95	3.06	105.20	2.93	68.25	1.18	419.27	8.69
3.50	129.02	4.53	118.95	3.02	106.11	2.48	68.79	1.34	421.80	8.40
3.60	127.46	5.55	119.05	3.84	106.36	3.67	69.02	1.64	421.03	11.59
3.70	126.51	4.48	119.69	3.00	107.05	2.51	69.45	1.33	422.11	8.75
3.80	125.17	4.46	120.13	3.19	107.58	2.53	69.83	1.23	422.50	8.46
3.90	122.90	4.49	120.01	3.02	107.74	2.54	70.06	1.29	420.89	8.51
4.00	120.76	4.38	120.14	3.10	108.08	2.57	70.37	1.30	419.93	8.45
4.10	119.52	4.58	121.17	3.10	109.20	2.58	71.04	1.24	422.06	8.79
4.20	116.31	4.47	120.64	3.34	109.03	2.60	71.12	1.25	418.72	9.26
4.30	112.54	4.19	119.90	3.22	108.76	2.58	71.17	1.57	414.47	8.84

Table 11.8: XRCF HRMA Effective Area within 35 mm Aperture. Units: cm<sup>2</sup> (continued)

Energy (keV)	Shell 1		Shell 3		Shell 4		Shell 6		HRMA	
	$A_{eff}$	Error								
4.40	109.44	4.13	119.91	3.29	109.09	2.80	71.49	1.30	412.59	8.39
4.50	105.08	4.12	119.02	3.59	108.76	3.13	71.54	1.75	407.51	9.18
4.60	99.91	3.84	117.82	3.25	108.25	2.59	71.50	1.31	400.99	8.23
4.70	92.84	3.57	117.16	3.18	108.41	3.53	71.88	1.53	393.85	10.72
4.80	87.12	3.53	116.06	3.45	108.04	2.87	71.92	1.31	386.95	8.06
4.90	80.76	3.18	115.03	3.08	107.75	2.80	72.02	2.05	379.46	10.33
5.00	73.88	3.22	113.49	2.99	107.07	2.57	71.92	1.29	370.26	7.60
5.10	65.94	2.63	112.03	3.11	106.56	2.59	71.97	1.53	360.08	9.01
5.20	58.02	2.45	110.40	2.92	105.93	2.64	71.93	1.32	349.45	7.10
5.30	49.75	2.18	108.68	3.18	105.34	2.82	71.96	1.36	338.29	8.94
5.40	41.70	1.85	106.39	3.04	104.35	2.61	71.80	1.27	326.11	6.86
5.50	33.88	1.47	103.71	2.76	103.25	2.55	71.67	1.29	313.57	6.40
5.60	27.07	1.17	100.90	2.64	102.15	2.48	71.53	1.66	301.96	6.17
5.70	21.46	1.04	98.05	2.66	101.13	2.51	71.47	1.28	291.80	6.25
5.80	16.85	0.89	95.07	2.57	100.17	2.82	71.45	1.32	282.78	5.97
5.90	12.45	0.57	91.31	2.39	99.17	2.62	71.54	1.59	273.15	5.93
6.00	9.65	0.61	87.46	2.29	97.98	2.46	71.47	1.29	265.09	6.18
6.10	7.42	0.40	82.89	2.40	96.53	2.36	71.35	1.52	256.63	6.42
6.20	5.69	0.33	77.57	2.40	94.84	2.34	71.18	1.28	247.76	5.01
6.30	4.36	0.69	71.55	2.12	93.06	2.27	71.03	1.53	238.54	4.94
6.40	3.35	0.18	64.65	1.86	90.99	2.28	70.87	1.30	228.52	4.62
6.50	2.60	0.13	57.10	1.86	88.37	2.17	70.50	1.27	217.42	4.85
6.60	2.01	0.28	49.51	1.54	86.16	3.10	70.47	1.46	207.15	4.79
6.70	1.54	0.28	41.70	1.37	83.67	2.35	70.55	1.27	196.60	4.07
6.80	2.16	0.09	35.20	0.92	80.51	2.29	70.32	1.59	186.63	4.99
6.90	1.77	0.08	29.26	1.29	76.51	3.55	69.93	2.23	176.29	6.24
7.00	1.46	0.06	24.08	0.76	72.24	2.19	69.69	3.49	166.64	6.55
7.10	1.21	0.05	19.53	0.51	67.00	3.95	69.33	3.02	156.56	7.44
7.20	1.02	0.04	15.84	0.73	60.57	1.74	68.40	1.23	145.64	2.93
7.40	0.69	0.03	9.64	0.36	47.50	1.18	68.70	1.30	126.42	2.61
7.60	0.51	0.02	6.21	0.53	35.23	1.62	67.98	1.87	109.91	4.08
7.80	0.38	0.02	4.02	0.35	25.12	0.64	67.17	1.44	96.74	1.92
8.00	0.28	0.01	2.64	0.24	17.15	0.46	66.19	2.56	86.37	2.85
8.20	0.21	0.01	1.80	0.06	11.36	0.29	65.05	1.73	78.60	2.05
8.40	0.17	0.01	1.29	0.04	7.50	0.19	64.02	1.21	73.22	1.63
8.60	0.13	0.01	0.93	0.04	4.78	0.12	62.29	2.16	68.47	1.77
8.80	0.10	0.00	0.72	0.02	3.09	0.37	60.53	1.42	64.82	2.86
9.00	0.08	0.00	0.53	0.01	2.07	0.07	58.25	1.36	61.42	1.87
9.20	0.06	0.00	0.40	0.01	1.43	0.11	54.90	1.12	57.37	1.22
9.40	0.05	0.00	0.30	0.01	1.01	0.03	50.68	1.84	52.67	1.38
9.60	0.04	0.00	0.24	0.01	0.76	0.02	44.45	1.87	46.14	2.33
9.80	0.03	0.00	0.18	0.00	0.56	0.02	35.67	1.38	37.03	1.71
10.00	0.02	0.00	0.14	0.00	0.41	0.01	26.07	0.67	27.13	0.87

Table 11.9: XRCF HRMA Effective Area within  $2\pi$  Steradian. Units:  $\text{cm}^2$ 

Energy (keV)	Shell 1		Shell 3		Shell 4		Shell 6		HRMA	
	$A_{eff}$	Error								
0.10	414.21	11.70	257.65	2.90	199.94	6.71	108.96	2.91	975.65	15.64
0.20	339.19	9.58	219.39	2.47	173.48	5.82	98.07	2.62	825.98	13.24
0.30	325.23	9.18	212.10	2.39	168.39	5.65	95.94	2.56	797.69	12.79
0.40	316.03	8.93	207.29	2.34	165.02	5.54	94.53	2.52	779.03	12.49
0.50	313.38	8.85	205.90	2.32	164.05	5.51	94.13	2.51	773.65	12.40
0.60	313.95	8.87	206.26	2.32	164.32	5.52	94.25	2.51	774.96	12.42
0.70	313.22	8.85	205.92	2.32	164.10	5.51	94.17	2.51	773.60	12.40
0.80	311.58	8.80	205.11	2.31	163.54	5.49	93.96	2.51	770.41	12.35
0.90	313.97	8.87	206.45	2.33	164.50	5.52	94.40	2.52	775.51	12.43
1.00	314.12	8.87	206.61	2.33	164.64	5.53	94.47	2.52	776.01	12.44
1.10	314.44	8.88	206.87	2.33	164.85	5.53	94.58	2.52	776.91	12.45
1.20	313.90	8.86	206.68	2.33	164.75	5.53	94.55	2.52	776.06	12.44
1.30	312.87	8.84	206.26	2.32	164.49	5.52	94.46	2.52	774.28	12.41
1.40	311.18	8.79	205.54	2.32	164.01	5.51	94.29	2.51	771.24	12.36
1.50	308.54	8.71	204.36	2.30	163.24	5.48	93.99	2.51	766.39	12.29
1.60	304.93	8.61	202.66	2.28	162.11	5.44	93.55	2.49	759.55	12.18
1.70	299.49	8.46	200.06	2.25	160.35	5.38	92.84	2.48	749.10	12.01
1.80	290.99	8.22	195.95	2.21	157.56	5.29	91.71	2.45	732.70	11.75
1.90	275.26	7.77	188.17	2.12	152.23	5.11	89.53	2.39	701.87	11.25
2.00	251.05	7.09	176.19	1.98	143.99	4.83	86.13	2.30	654.37	10.49
2.10	132.79	3.75	108.47	1.22	94.69	3.18	63.70	1.70	398.14	6.38
2.20	119.66	3.38	99.03	1.12	87.19	2.93	59.80	1.59	364.32	5.84
2.30	127.46	4.43	107.75	2.98	96.85	2.36	63.65	1.35	398.29	10.16
2.40	130.96	4.34	110.58	2.76	99.04	2.29	64.71	1.14	407.10	8.27
2.50	130.89	4.82	111.29	3.08	99.61	2.61	65.03	1.53	407.91	10.29
2.60	125.29	5.89	107.98	4.08	96.97	3.28	63.78	1.76	394.38	13.38
2.70	131.30	4.59	112.65	2.85	100.63	2.72	65.56	1.14	410.11	8.54
2.80	133.43	4.49	114.88	2.87	102.39	2.38	66.47	1.28	416.70	8.18
2.90	128.76	4.87	112.83	2.89	100.91	2.76	65.88	1.16	407.46	9.87
3.00	131.25	4.61	115.11	3.70	102.68	2.82	66.74	1.65	414.73	11.25
3.10	132.34	5.44	116.77	3.87	104.03	2.98	67.47	1.69	419.40	10.74
3.20	128.25	4.54	114.91	3.05	102.70	2.60	66.93	1.22	411.44	9.76
3.30	129.96	4.47	117.03	3.10	104.43	2.49	67.83	1.76	417.93	9.54
3.40	129.93	4.86	118.03	3.07	105.33	2.94	68.35	1.19	420.41	8.71
3.50	129.80	4.56	119.05	3.02	106.26	2.49	68.89	1.34	422.97	8.43
3.60	128.24	5.58	119.15	3.84	106.50	3.67	69.12	1.64	422.21	11.62
3.70	127.30	4.51	119.80	3.00	107.21	2.51	69.57	1.33	423.35	8.77
3.80	125.96	4.49	120.24	3.19	107.75	2.53	69.96	1.23	423.75	8.49
3.90	123.70	4.52	120.14	3.02	107.91	2.55	70.20	1.29	422.19	8.54
4.00	121.55	4.40	120.27	3.10	108.27	2.58	70.51	1.30	421.24	8.48
4.10	120.32	4.61	121.31	3.10	109.39	2.58	71.19	1.24	423.42	8.82
4.20	117.11	4.50	120.77	3.34	109.24	2.60	71.27	1.25	420.08	9.29
4.30	113.33	4.22	120.03	3.22	108.97	2.58	71.31	1.57	415.82	8.87

Table 11.9: XRCF HRMA Effective Area within  $2\pi$  Steradian. Units:  $\text{cm}^2$  (continued)

Energy (keV)	Shell 1		Shell 3		Shell 4		Shell 6		HRMA	
	$A_{eff}$	Error								
4.40	110.22	4.16	120.03	3.30	109.32	2.81	71.65	1.31	413.95	8.41
4.50	105.83	4.15	119.15	3.59	109.00	3.14	71.71	1.76	408.87	9.21
4.60	100.62	3.87	117.96	3.25	108.50	2.59	71.67	1.31	402.34	8.26
4.70	93.51	3.59	117.31	3.19	108.66	3.54	72.06	1.54	395.17	10.76
4.80	87.75	3.56	116.23	3.46	108.28	2.88	72.09	1.31	388.25	8.08
4.90	81.34	3.20	115.18	3.08	108.00	2.81	72.20	2.05	380.70	10.36
5.00	74.42	3.25	113.63	3.00	107.32	2.58	72.11	1.29	371.46	7.62
5.10	66.44	2.65	112.18	3.11	106.83	2.60	72.16	1.54	361.26	9.04
5.20	58.46	2.47	110.54	2.93	106.19	2.64	72.13	1.32	350.56	7.12
5.30	50.13	2.20	108.83	3.18	105.61	2.83	72.16	1.36	339.35	8.97
5.40	42.02	1.86	106.51	3.04	104.63	2.62	72.02	1.27	327.11	6.88
5.50	34.16	1.49	103.85	2.76	103.53	2.56	71.87	1.30	314.50	6.42
5.60	27.30	1.18	101.04	2.64	102.44	2.49	71.75	1.66	302.87	6.19
5.70	21.65	1.05	98.18	2.67	101.42	2.51	71.68	1.29	292.65	6.27
5.80	17.00	0.90	95.20	2.58	100.46	2.83	71.66	1.32	283.58	5.99
5.90	12.57	0.57	91.44	2.39	99.46	2.62	71.74	1.59	273.92	5.95
6.00	9.75	0.61	87.59	2.29	98.27	2.47	71.68	1.29	265.83	6.20
6.10	7.50	0.41	83.01	2.40	96.81	2.37	71.57	1.53	257.36	6.44
6.20	5.76	0.33	77.69	2.41	95.12	2.35	71.40	1.29	248.46	5.02
6.30	4.42	0.70	71.66	2.13	93.32	2.28	71.25	1.54	239.21	4.96
6.40	3.39	0.18	64.75	1.86	91.26	2.29	71.08	1.30	229.17	4.63
6.50	2.64	0.13	57.18	1.86	88.64	2.18	70.71	1.27	218.04	4.87
6.60	2.05	0.28	49.58	1.54	86.43	3.11	70.68	1.46	207.74	4.80
6.70	1.57	0.28	41.76	1.38	83.93	2.36	70.76	1.27	197.18	4.09
6.80	2.20	0.09	35.26	0.93	80.75	2.29	70.54	1.59	187.19	5.00
6.90	1.81	0.08	29.31	1.29	76.75	3.56	70.14	2.23	176.82	6.26
7.00	1.49	0.06	24.13	0.76	72.47	2.20	69.92	3.50	167.17	6.57
7.10	1.23	0.05	19.57	0.51	67.21	3.96	69.55	3.03	157.06	7.46
7.20	1.04	0.04	15.88	0.73	60.77	1.75	68.63	1.24	146.12	2.94
7.40	0.71	0.03	9.67	0.36	47.65	1.19	68.94	1.31	126.85	2.62
7.60	0.53	0.02	6.22	0.53	35.34	1.62	68.22	1.87	110.30	4.09
7.80	0.39	0.02	4.04	0.35	25.21	0.64	67.40	1.45	97.08	1.92
8.00	0.29	0.01	2.65	0.24	17.21	0.46	66.42	2.56	86.68	2.86
8.20	0.22	0.01	1.81	0.06	11.41	0.29	65.26	1.74	78.88	2.05
8.40	0.17	0.01	1.30	0.04	7.53	0.19	64.22	1.22	73.48	1.64
8.60	0.13	0.01	0.94	0.04	4.81	0.12	62.50	2.16	68.73	1.77
8.80	0.10	0.00	0.73	0.02	3.11	0.37	60.72	1.42	65.04	2.87
9.00	0.08	0.00	0.54	0.01	2.08	0.07	58.45	1.36	61.64	1.87
9.20	0.06	0.00	0.40	0.01	1.45	0.11	55.09	1.13	57.59	1.22
9.40	0.05	0.00	0.30	0.01	1.02	0.03	50.85	1.85	52.86	1.39
9.60	0.04	0.00	0.24	0.01	0.77	0.02	44.61	1.87	46.31	2.33
9.80	0.03	0.00	0.19	0.00	0.57	0.02	35.80	1.39	37.18	1.71
10.00	0.03	0.00	0.15	0.00	0.42	0.01	26.17	0.67	27.24	0.87

## 11.18 On-orbit HRMA Effective Area Prediction

Figures 11.54–11.56 show the on-orbit HRMA and four shells effective areas within 2 mm, 35 mm diameters and  $2\pi$  steradians,<sup>7</sup> for the original raytrace and the calibrated curves with errors estimated in §11.15. Tables 11.10 – 11.12 list the values of the on-orbit effective areas with energy grid of 0.1 keV.<sup>6</sup> The “rdb” tables on the web (see below) have denser energy grid.

These are our current best on-orbit effective area predictions for the HRMA. They can be used to make AXAF on-orbit performance predictions. The “rdb” tables of the predicted on-orbit HRMA effective area, as well as Figures 11.54–11.56, can be accessed on the World Wide Web page:

[http://hea-www.harvard.edu/MST/mirror/www/orbit/hrma\\_ea.html](http://hea-www.harvard.edu/MST/mirror/www/orbit/hrma_ea.html)

at the bottom of the web page, please click:

[On-orbit HRMA Effective Area within 2 mm aperture and its figure.](#)

[On-orbit HRMA Effective Area within 35 mm aperture and its figure.](#)

[On-orbit HRMA Effective Area within 2pi steradians and its figure.](#)

---

<sup>7</sup>Although it is not possible to use just a single shell on-orbit. The HETG operations do require the effective area predictions for Shells 1+3 and Shells 4+6 separately.

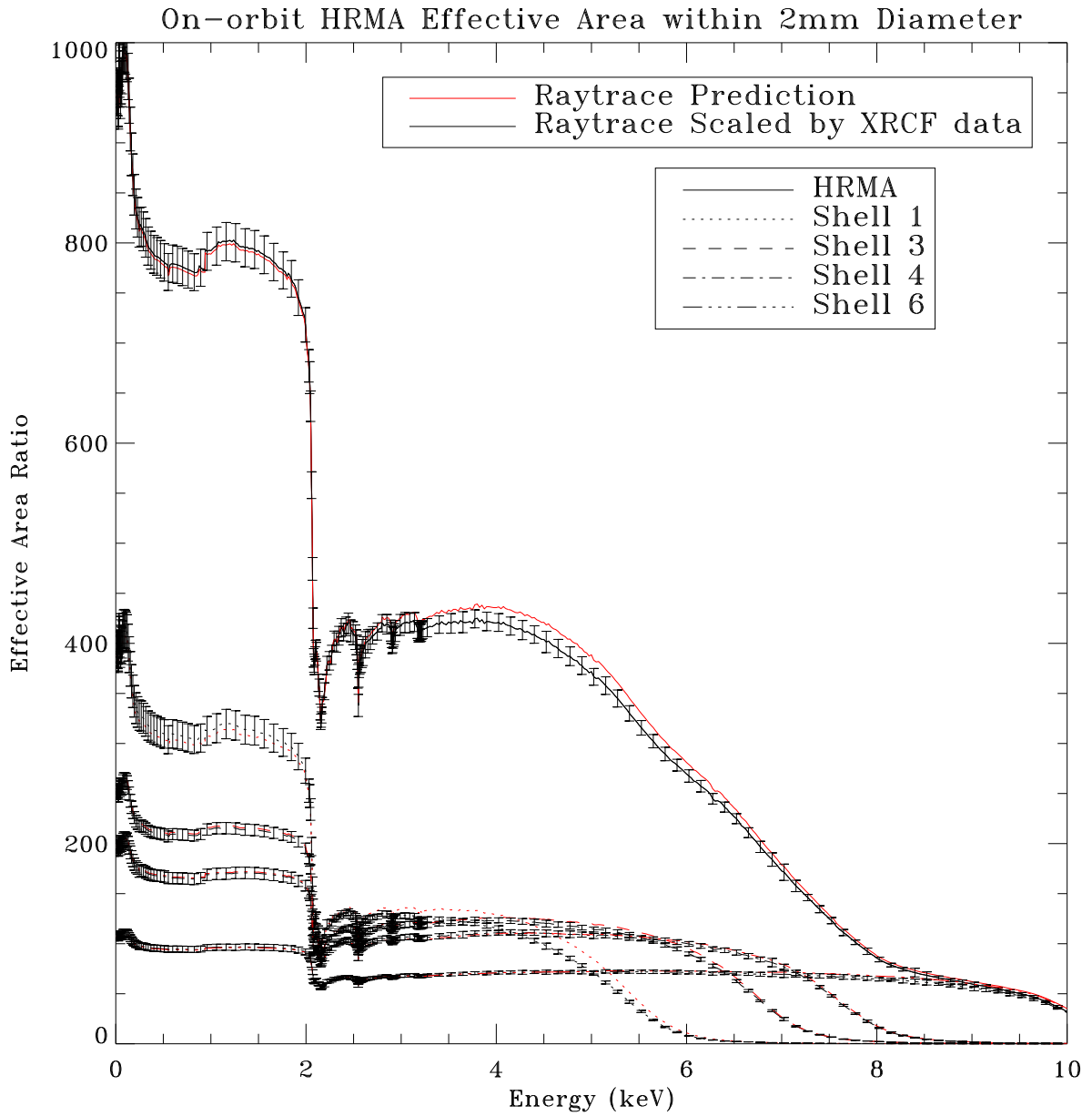


Figure 11.54: The on-orbit HRMA and four shells effective areas within 2 mm aperture. The original raytrace predictions and the calibration data scaled raytrace predictions.

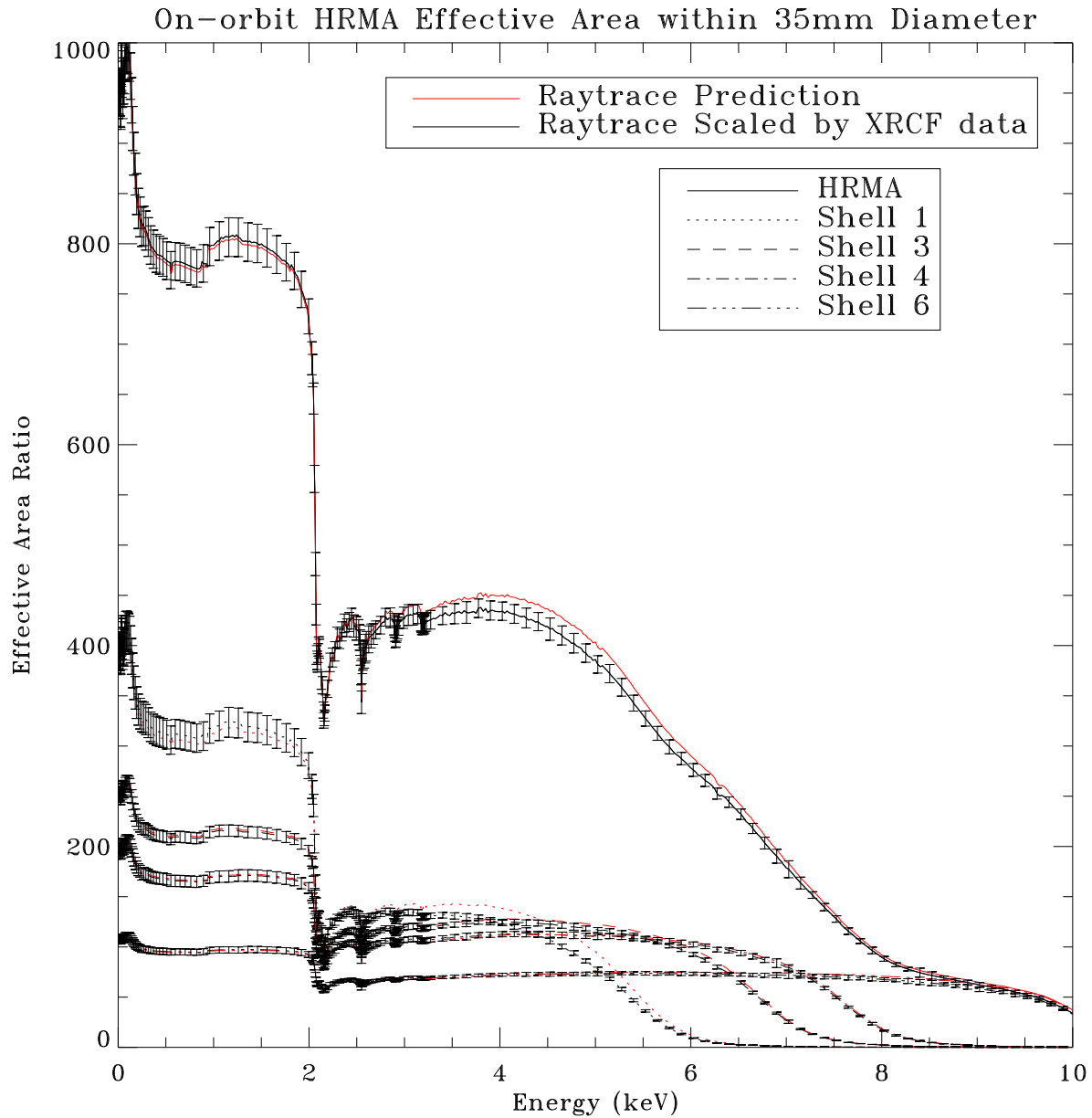


Figure 11.55: The on-orbit HRMA and four shells effective areas within 35 mm aperture. The original raytrace predictions and the calibration data scaled raytrace predictions.

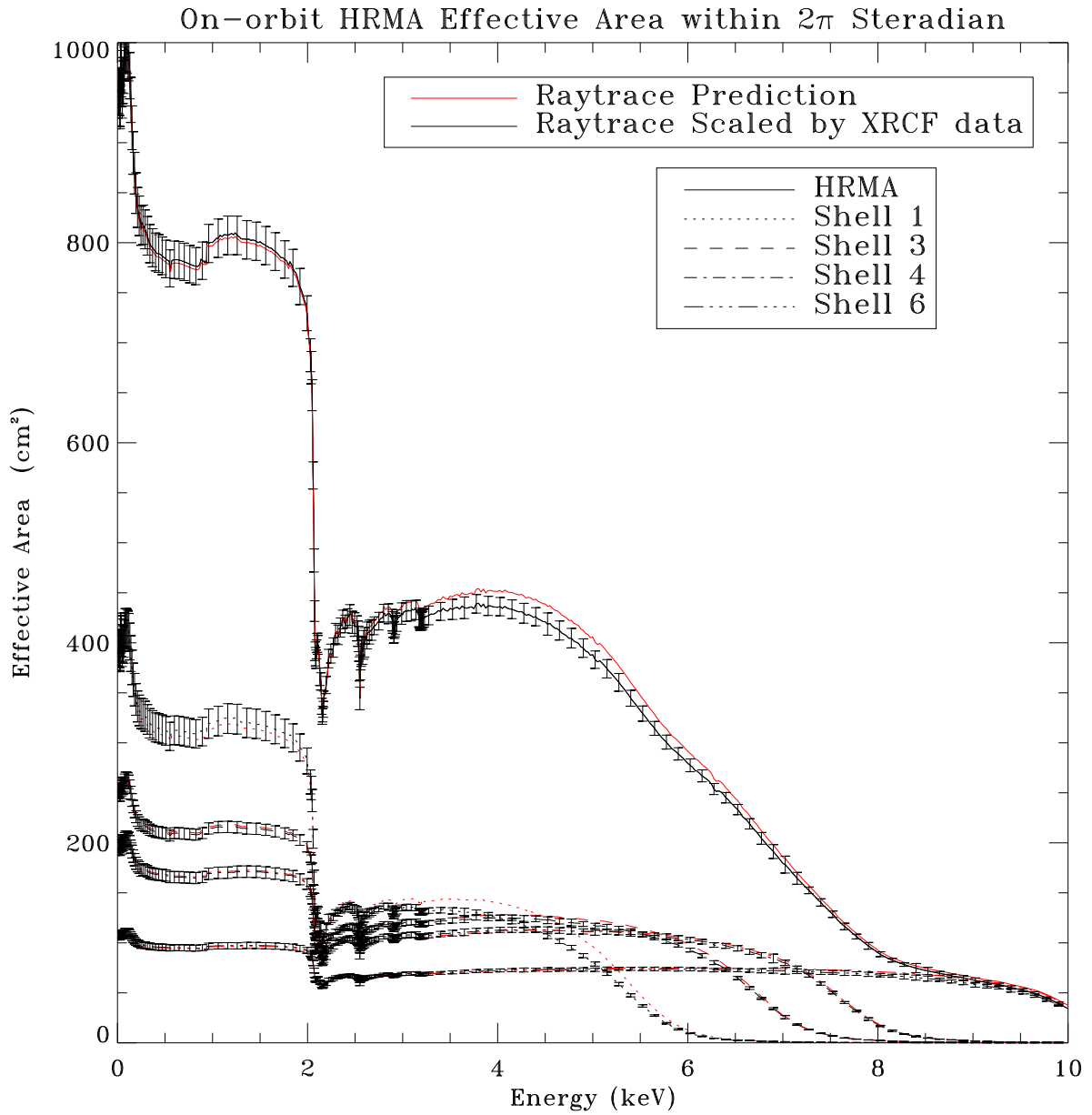


Figure 11.56: The on-orbit HRMA and four shells effective areas within  $2\pi$  steradian. The original raytrace predictions and the calibration data scaled raytrace predictions.

Table 11.10: On-orbit HRMA Effective Area within 2 mm Diameter. Units: cm<sup>2</sup>

Energy (keV)	Shell 1		Shell 3		Shell 4		Shell 6		HRMA	
	$A_{eff}$	Error								
0.10	417.05	11.78	264.44	2.98	205.31	6.89	111.03	2.96	992.73	15.91
0.20	341.10	9.63	225.11	2.53	178.10	5.98	99.83	2.66	840.01	13.47
0.30	326.93	9.23	217.61	2.45	172.82	5.80	97.53	2.60	810.95	13.00
0.40	317.43	8.96	212.67	2.39	169.35	5.68	96.00	2.56	791.63	12.69
0.50	314.39	8.88	211.23	2.38	168.37	5.65	95.45	2.55	785.67	12.59
0.60	314.71	8.89	211.58	2.38	168.62	5.66	95.54	2.55	786.67	12.61
0.70	313.52	8.85	211.23	2.38	168.39	5.65	95.47	2.55	784.84	12.58
0.80	311.52	8.80	210.36	2.37	167.82	5.63	95.23	2.54	781.19	12.52
0.90	313.53	8.85	211.71	2.38	168.77	5.67	95.65	2.55	785.90	12.60
1.00	313.30	8.85	211.84	2.39	168.87	5.67	95.70	2.55	785.96	12.60
1.10	313.07	8.84	212.06	2.39	169.05	5.67	95.79	2.55	786.22	12.60
1.20	312.10	8.81	211.81	2.39	168.92	5.67	95.74	2.55	784.84	12.58
1.30	310.48	8.77	211.34	2.38	168.61	5.66	95.62	2.55	782.35	12.54
1.40	308.34	8.71	210.55	2.37	168.06	5.64	95.42	2.54	778.70	12.48
1.50	305.32	8.62	209.27	2.36	167.21	5.61	95.10	2.54	773.26	12.40
1.60	301.12	8.50	207.43	2.34	166.01	5.57	94.62	2.52	765.60	12.27
1.70	295.20	8.34	204.69	2.30	164.17	5.51	93.88	2.50	754.44	12.09
1.80	286.33	8.09	200.45	2.26	161.26	5.41	92.69	2.47	737.35	11.82
1.90	270.36	7.64	192.45	2.17	155.73	5.23	90.47	2.41	705.83	11.31
2.00	246.35	6.96	180.13	2.03	147.28	4.94	87.02	2.32	657.91	10.55
2.10	130.12	3.67	110.91	1.25	96.85	3.25	64.34	1.72	400.79	6.42
2.20	116.99	3.30	101.19	1.14	89.14	2.99	60.40	1.61	366.44	5.87
2.30	124.31	4.32	110.06	3.04	98.99	2.41	64.25	1.36	400.00	10.21
2.40	127.44	4.22	112.91	2.82	101.19	2.34	65.29	1.15	408.42	8.30
2.50	127.14	4.68	113.59	3.14	101.74	2.66	65.61	1.54	408.93	10.31
2.60	121.48	5.71	110.18	4.16	99.02	3.35	64.28	1.77	395.06	13.40
2.70	127.06	4.44	114.92	2.90	102.69	2.77	66.04	1.15	410.40	8.55
2.80	128.87	4.33	117.14	2.93	104.47	2.42	66.93	1.29	416.62	8.18
2.90	124.14	4.70	115.00	2.94	102.93	2.82	66.33	1.17	407.14	9.86
3.00	126.31	4.44	117.26	3.77	104.71	2.88	67.18	1.66	414.02	11.23
3.10	127.03	5.22	118.91	3.94	106.03	3.04	67.87	1.70	418.20	10.71
3.20	122.81	4.35	116.96	3.11	104.61	2.65	67.31	1.23	409.89	9.72
3.30	124.24	4.28	119.07	3.15	106.32	2.53	68.19	1.77	416.00	9.49
3.40	123.92	4.64	120.02	3.12	107.19	2.99	68.68	1.19	418.03	8.66
3.50	123.56	4.34	121.03	3.07	108.11	2.53	69.20	1.34	420.29	8.37
3.60	121.83	5.30	121.10	3.91	108.32	3.73	69.41	1.64	419.21	11.54
3.70	120.72	4.28	121.73	3.05	108.95	2.55	69.83	1.34	420.01	8.70
3.80	119.25	4.25	122.11	3.24	109.47	2.57	70.19	1.23	420.14	8.41
3.90	116.88	4.27	121.97	3.07	109.55	2.59	70.38	1.29	418.26	8.46
4.00	114.65	4.15	122.02	3.14	109.87	2.61	70.69	1.30	417.06	8.39
4.10	113.37	4.35	123.02	3.15	110.91	2.62	71.33	1.25	418.97	8.72
4.20	110.13	4.23	122.40	3.39	110.72	2.64	71.38	1.25	415.41	9.19
4.30	106.56	3.97	121.60	3.27	110.42	2.62	71.40	1.57	411.23	8.77

Table 11.10: On-orbit HRMA Effective Area within 2 mm Diameter. Units: cm<sup>2</sup> (continued)

Energy (keV)	Shell 1		Shell 3		Shell 4		Shell 6		HRMA	
	$A_{eff}$	Error								
4.40	103.54	3.91	121.57	3.34	110.69	2.84	71.70	1.31	409.27	8.32
4.50	99.42	3.90	120.63	3.64	110.35	3.18	71.71	1.76	404.32	9.11
4.60	94.59	3.64	119.40	3.29	109.79	2.62	71.65	1.31	398.04	8.17
4.70	88.28	3.39	118.74	3.23	109.93	3.58	71.98	1.53	391.68	10.66
4.80	83.12	3.37	117.64	3.50	109.46	2.91	71.97	1.31	385.24	8.02
4.90	77.41	3.04	116.63	3.12	109.12	2.84	72.02	2.05	378.41	10.30
5.00	71.27	3.11	115.03	3.03	108.39	2.60	71.89	1.29	369.93	7.59
5.10	64.26	2.57	113.58	3.15	107.86	2.62	71.89	1.53	360.76	9.03
5.20	57.12	2.41	111.94	2.96	107.16	2.67	71.84	1.32	350.99	7.13
5.30	49.47	2.17	110.25	3.23	106.55	2.85	71.83	1.35	340.55	9.00
5.40	41.64	1.85	107.98	3.08	105.54	2.64	71.65	1.27	328.63	6.91
5.50	33.67	1.47	105.39	2.80	104.41	2.58	71.45	1.29	315.90	6.45
5.60	26.43	1.14	102.74	2.69	103.26	2.51	71.29	1.65	303.83	6.21
5.70	20.35	0.99	100.08	2.72	102.26	2.54	71.18	1.28	293.22	6.28
5.80	15.45	0.81	97.30	2.63	101.26	2.85	71.13	1.31	283.94	6.00
5.90	10.99	0.50	93.92	2.46	100.31	2.65	71.17	1.58	274.60	5.97
6.00	8.32	0.52	90.42	2.37	99.11	2.49	71.06	1.28	266.98	6.23
6.10	6.29	0.34	86.38	2.50	97.69	2.39	70.88	1.51	259.31	6.49
6.20	4.79	0.28	81.72	2.53	96.09	2.37	70.68	1.28	251.46	5.09
6.30	3.66	0.58	76.49	2.27	94.39	2.30	70.52	1.52	243.38	5.04
6.40	2.80	0.15	70.42	2.03	92.42	2.32	70.28	1.29	234.47	4.74
6.50	2.18	0.11	63.46	2.07	89.96	2.21	69.88	1.25	224.26	5.01
6.60	1.69	0.23	56.22	1.75	87.99	3.16	69.80	1.45	214.67	4.96
6.70	1.29	0.23	48.05	1.58	85.83	2.41	69.88	1.25	204.21	4.23
6.80	1.81	0.08	40.44	1.06	83.04	2.36	69.59	1.57	193.50	5.17
6.90	1.49	0.06	32.88	1.44	79.54	3.69	69.16	2.20	182.02	6.45
7.00	1.23	0.05	26.04	0.82	75.94	2.31	68.91	3.45	171.38	6.74
7.10	1.01	0.04	20.13	0.53	71.51	4.21	68.47	2.98	160.69	7.63
7.20	0.86	0.04	15.65	0.72	65.83	1.89	67.54	1.22	149.76	3.01
7.40	0.58	0.02	8.87	0.33	54.92	1.37	67.79	1.28	132.15	2.73
7.60	0.43	0.02	5.64	0.48	41.97	1.92	67.00	1.84	115.14	4.27
7.80	0.32	0.01	3.68	0.32	28.82	0.73	66.14	1.42	99.08	1.96
8.00	0.23	0.01	2.44	0.22	17.68	0.47	65.15	2.52	85.63	2.83
8.20	0.18	0.01	1.68	0.05	10.59	0.27	64.01	1.71	76.61	1.99
8.40	0.14	0.01	1.21	0.03	6.69	0.17	63.02	1.19	71.29	1.59
8.60	0.11	0.00	0.88	0.04	4.26	0.11	61.44	2.13	67.00	1.73
8.80	0.08	0.00	0.69	0.02	2.78	0.33	59.83	1.40	63.74	2.81
9.00	0.06	0.00	0.51	0.01	1.88	0.07	57.91	1.35	60.85	1.85
9.20	0.05	0.00	0.38	0.01	1.32	0.10	55.16	1.13	57.48	1.22
9.40	0.04	0.00	0.29	0.01	0.93	0.03	52.13	1.89	54.04	1.42
9.60	0.03	0.00	0.23	0.01	0.70	0.02	47.63	2.00	49.29	2.48
9.80	0.03	0.00	0.18	0.00	0.52	0.02	41.45	1.61	42.85	1.98
10.00	0.02	0.00	0.14	0.00	0.39	0.01	32.78	0.84	33.92	1.09

Table 11.11: On-orbit HRMA Effective Area within 35 mm Diameter. Units: cm<sup>2</sup>

Energy (keV)	Shell 1		Shell 3		Shell 4		Shell 6		HRMA	
	$A_{eff}$	Error								
0.10	417.51	11.79	264.48	2.98	205.36	6.89	111.07	2.96	993.31	15.92
0.20	341.81	9.65	225.18	2.54	178.17	5.98	99.95	2.67	840.98	13.48
0.30	327.68	9.25	217.70	2.45	172.94	5.81	97.75	2.61	812.12	13.02
0.40	318.34	8.99	212.76	2.40	169.48	5.69	96.30	2.57	793.05	12.71
0.50	315.56	8.91	211.32	2.38	168.48	5.66	95.87	2.56	787.44	12.62
0.60	316.08	8.93	211.69	2.38	168.75	5.66	95.98	2.56	788.69	12.64
0.70	315.25	8.90	211.34	2.38	168.52	5.66	95.88	2.56	787.20	12.62
0.80	313.53	8.85	210.51	2.37	167.95	5.64	95.64	2.55	783.87	12.57
0.90	315.88	8.92	211.88	2.39	168.94	5.67	96.07	2.56	788.97	12.65
1.00	315.93	8.92	212.05	2.39	169.07	5.68	96.14	2.56	789.38	12.65
1.10	316.15	8.93	212.31	2.39	169.28	5.68	96.25	2.57	790.18	12.67
1.20	315.53	8.91	212.12	2.39	169.17	5.68	96.22	2.57	789.23	12.65
1.30	314.37	8.88	211.68	2.38	168.90	5.67	96.12	2.56	787.30	12.62
1.40	312.54	8.83	210.92	2.38	168.40	5.65	95.94	2.56	784.05	12.57
1.50	309.90	8.75	209.71	2.36	167.60	5.63	95.63	2.55	779.12	12.49
1.60	306.15	8.65	207.95	2.34	166.44	5.59	95.18	2.54	772.04	12.38
1.70	300.58	8.49	205.27	2.31	164.62	5.53	94.46	2.52	761.33	12.20
1.80	291.97	8.25	201.05	2.26	161.75	5.43	93.30	2.49	744.59	11.94
1.90	276.13	7.80	193.07	2.17	156.27	5.25	91.08	2.43	713.27	11.43
2.00	251.91	7.11	180.80	2.04	147.83	4.96	87.62	2.34	665.21	10.66
2.10	133.33	3.77	111.36	1.25	97.23	3.26	64.82	1.73	405.24	6.50
2.20	120.06	3.39	101.64	1.14	89.52	3.01	60.84	1.62	370.72	5.94
2.30	127.84	4.44	110.58	3.06	99.43	2.43	64.75	1.37	405.12	10.34
2.40	131.31	4.35	113.49	2.83	101.68	2.35	65.81	1.16	414.05	8.41
2.50	131.25	4.83	114.22	3.16	102.26	2.68	66.15	1.55	414.87	10.46
2.60	125.60	5.91	110.83	4.18	99.56	3.37	64.86	1.79	401.09	13.60
2.70	131.61	4.60	115.62	2.92	103.30	2.79	66.67	1.16	417.05	8.68
2.80	133.74	4.50	117.90	2.94	105.12	2.44	67.58	1.30	423.73	8.32
2.90	129.08	4.88	115.79	2.96	103.60	2.84	66.98	1.18	414.39	10.04
3.00	131.57	4.62	118.12	3.80	105.42	2.90	67.86	1.68	421.75	11.44
3.10	132.64	5.46	119.83	3.97	106.81	3.06	68.59	1.71	426.47	10.93
3.20	128.54	4.55	117.93	3.13	105.43	2.67	68.05	1.24	418.40	9.92
3.30	130.26	4.49	120.11	3.18	107.20	2.55	68.95	1.79	425.01	9.70
3.40	130.22	4.87	121.13	3.15	108.13	3.02	69.47	1.21	427.51	8.86
3.50	130.11	4.57	122.19	3.10	109.10	2.55	70.02	1.36	430.17	8.57
3.60	128.56	5.60	122.31	3.95	109.35	3.77	70.27	1.66	429.46	11.82
3.70	127.67	4.52	122.98	3.08	110.05	2.58	70.73	1.35	430.66	8.92
3.80	126.39	4.50	123.43	3.28	110.61	2.60	71.11	1.25	431.15	8.63
3.90	124.19	4.54	123.35	3.10	110.77	2.61	71.32	1.31	429.65	8.69
4.00	122.11	4.42	123.50	3.18	111.12	2.64	71.63	1.32	428.79	8.63
4.10	121.01	4.64	124.59	3.19	112.27	2.65	72.34	1.26	431.21	8.98
4.20	117.90	4.53	124.02	3.43	112.12	2.67	72.43	1.27	427.99	9.47
4.30	114.27	4.25	123.27	3.31	111.87	2.65	72.46	1.59	423.90	9.04

Table 11.11: On-orbit HRMA Effective Area within 35 mm Diameter. Units: cm<sup>2</sup> (continued)

Energy (keV)	Shell 1		Shell 3		Shell 4		Shell 6		HRMA	
	$A_{eff}$	Error								
4.40	111.34	4.20	123.31	3.39	112.22	2.88	72.80	1.33	422.29	8.58
4.50	107.13	4.20	122.45	3.69	111.90	3.22	72.84	1.78	417.43	9.40
4.60	102.18	3.93	121.27	3.34	111.38	2.66	72.80	1.34	411.19	8.44
4.70	95.61	3.67	120.66	3.28	111.56	3.63	73.20	1.56	404.74	11.02
4.80	90.21	3.66	119.61	3.56	111.18	2.96	73.24	1.33	398.29	8.29
4.90	84.26	3.31	118.62	3.18	110.91	2.88	73.34	2.09	391.39	10.65
5.00	77.76	3.39	117.08	3.09	110.23	2.65	73.25	1.31	382.72	7.85
5.10	70.28	2.81	115.67	3.21	109.76	2.67	73.30	1.56	373.22	9.34
5.20	62.64	2.65	114.06	3.02	109.12	2.72	73.28	1.34	363.03	7.38
5.30	54.37	2.38	112.41	3.29	108.54	2.91	73.32	1.38	352.03	9.30
5.40	45.91	2.03	110.18	3.15	107.57	2.69	73.18	1.29	339.52	7.14
5.50	37.23	1.62	107.60	2.86	106.46	2.63	73.03	1.32	326.04	6.66
5.60	29.31	1.27	104.94	2.75	105.40	2.56	72.91	1.69	313.31	6.40
5.70	22.67	1.10	102.28	2.78	104.40	2.59	72.85	1.31	302.08	6.47
5.80	17.26	0.91	99.52	2.69	103.48	2.92	72.83	1.34	292.31	6.17
5.90	12.32	0.56	96.12	2.52	102.55	2.71	72.93	1.62	282.44	6.14
6.00	9.35	0.59	92.66	2.42	101.42	2.54	72.86	1.31	274.61	6.40
6.10	7.09	0.39	88.56	2.56	100.03	2.45	72.75	1.55	266.70	6.67
6.20	5.41	0.31	83.81	2.59	98.43	2.43	72.58	1.31	258.55	5.23
6.30	4.14	0.66	78.47	2.33	96.72	2.36	72.43	1.56	250.21	5.19
6.40	3.18	0.17	72.28	2.08	94.80	2.38	72.24	1.33	241.13	4.88
6.50	2.48	0.13	65.18	2.12	92.31	2.27	71.88	1.29	230.71	5.15
6.60	1.92	0.27	57.79	1.79	90.35	3.25	71.85	1.49	220.96	5.11
6.70	1.48	0.26	49.42	1.63	88.20	2.48	71.93	1.29	210.25	4.36
6.80	2.07	0.09	41.60	1.09	85.38	2.42	71.71	1.62	199.32	5.33
6.90	1.71	0.07	33.86	1.49	81.80	3.80	71.31	2.27	187.59	6.64
7.00	1.41	0.06	26.84	0.85	78.14	2.37	71.11	3.56	176.73	6.95
7.10	1.17	0.05	20.76	0.54	73.63	4.34	70.73	3.08	165.84	7.88
7.20	0.99	0.04	16.15	0.74	67.83	1.95	69.81	1.26	154.65	3.11
7.40	0.68	0.03	9.16	0.34	56.65	1.41	70.17	1.33	136.64	2.82
7.60	0.50	0.02	5.83	0.50	43.38	1.99	69.47	1.91	119.28	4.43
7.80	0.37	0.02	3.81	0.33	29.84	0.76	68.67	1.48	102.82	2.04
8.00	0.28	0.01	2.53	0.23	18.35	0.49	67.73	2.62	89.01	2.94
8.20	0.21	0.01	1.74	0.06	11.02	0.28	66.64	1.78	79.77	2.08
8.40	0.16	0.01	1.26	0.03	6.97	0.18	65.69	1.24	74.31	1.66
8.60	0.13	0.01	0.91	0.04	4.44	0.11	64.11	2.22	69.92	1.81
8.80	0.10	0.00	0.71	0.02	2.90	0.34	62.55	1.46	66.65	2.94
9.00	0.08	0.00	0.53	0.01	1.97	0.07	60.63	1.41	63.70	1.94
9.20	0.06	0.00	0.40	0.01	1.38	0.11	57.83	1.18	60.27	1.28
9.40	0.05	0.00	0.30	0.01	0.98	0.03	54.73	1.99	56.74	1.49
9.60	0.04	0.00	0.24	0.01	0.74	0.02	50.09	2.10	51.83	2.61
9.80	0.03	0.00	0.18	0.00	0.55	0.02	43.63	1.69	45.11	2.08
10.00	0.02	0.00	0.14	0.00	0.41	0.01	34.62	0.89	35.82	1.15

Table 11.12: On-orbit HRMA Effective Area within  $2\pi$  Steradian. Units:  $\text{cm}^2$ 

Energy (keV)	Shell 1		Shell 3		Shell 4		Shell 6		HRMA	
	$A_{eff}$	Error								
0.10	417.52	11.79	264.49	2.98	205.36	6.89	111.07	2.96	993.33	15.92
0.20	341.87	9.65	225.19	2.54	178.18	5.98	99.95	2.67	841.05	13.48
0.30	327.75	9.26	217.71	2.45	172.95	5.81	97.76	2.61	812.21	13.02
0.40	318.48	8.99	212.78	2.40	169.49	5.69	96.30	2.57	793.21	12.72
0.50	315.73	8.92	211.35	2.38	168.50	5.66	95.88	2.56	787.66	12.63
0.60	316.31	8.93	211.72	2.38	168.77	5.67	95.99	2.56	788.97	12.65
0.70	315.56	8.91	211.38	2.38	168.54	5.66	95.89	2.56	787.57	12.62
0.80	313.88	8.86	210.54	2.37	167.98	5.64	95.66	2.55	784.28	12.57
0.90	316.27	8.93	211.92	2.39	168.97	5.67	96.09	2.56	789.44	12.65
1.00	316.39	8.93	212.08	2.39	169.11	5.68	96.16	2.56	789.92	12.66
1.10	316.66	8.94	212.35	2.39	169.33	5.68	96.27	2.57	790.79	12.68
1.20	316.08	8.93	212.16	2.39	169.22	5.68	96.24	2.57	789.90	12.66
1.30	314.99	8.90	211.73	2.38	168.95	5.67	96.15	2.56	788.03	12.63
1.40	313.26	8.85	210.97	2.38	168.46	5.66	95.97	2.56	784.90	12.58
1.50	310.65	8.77	209.76	2.36	167.67	5.63	95.67	2.55	780.02	12.50
1.60	306.94	8.67	208.01	2.34	166.51	5.59	95.21	2.54	772.99	12.39
1.70	301.41	8.51	205.33	2.31	164.70	5.53	94.50	2.52	762.33	12.22
1.80	292.83	8.27	201.12	2.26	161.83	5.43	93.35	2.49	745.64	11.95
1.90	277.01	7.82	193.14	2.17	156.35	5.25	91.12	2.43	714.33	11.45
2.00	252.74	7.14	180.86	2.04	147.92	4.97	87.67	2.34	666.22	10.68
2.10	133.79	3.78	111.39	1.25	97.29	3.27	64.87	1.73	405.84	6.51
2.20	120.51	3.40	101.68	1.14	89.58	3.01	60.88	1.62	371.31	5.95
2.30	128.35	4.46	110.62	3.06	99.51	2.43	64.80	1.37	405.82	10.36
2.40	131.85	4.37	113.54	2.84	101.76	2.35	65.87	1.16	414.78	8.43
2.50	131.80	4.85	114.27	3.16	102.35	2.68	66.21	1.56	415.64	10.48
2.60	126.15	5.93	110.88	4.19	99.64	3.37	64.92	1.79	401.86	13.63
2.70	132.21	4.62	115.67	2.92	103.40	2.79	66.73	1.16	417.88	8.70
2.80	134.37	4.52	117.96	2.95	105.21	2.44	67.65	1.30	424.61	8.33
2.90	129.69	4.91	115.86	2.96	103.70	2.84	67.07	1.18	415.27	10.06
3.00	132.19	4.64	118.19	3.80	105.52	2.90	67.95	1.68	422.65	11.46
3.10	133.30	5.48	119.90	3.98	106.92	3.07	68.69	1.72	427.43	10.95
3.20	129.18	4.58	117.99	3.13	105.54	2.67	68.15	1.24	419.36	9.95
3.30	130.95	4.51	120.18	3.18	107.33	2.55	69.06	1.79	426.03	9.72
3.40	130.92	4.90	121.20	3.15	108.24	3.02	69.59	1.21	428.54	8.88
3.50	130.83	4.60	122.26	3.10	109.21	2.56	70.15	1.36	431.24	8.59
3.60	129.29	5.63	122.39	3.95	109.48	3.77	70.40	1.67	430.56	11.85
3.70	128.40	4.55	123.07	3.09	110.19	2.58	70.85	1.36	431.79	8.95
3.80	127.13	4.53	123.53	3.28	110.75	2.60	71.25	1.25	432.32	8.66
3.90	124.93	4.56	123.45	3.11	110.92	2.62	71.45	1.31	430.83	8.71
4.00	122.85	4.45	123.59	3.18	111.29	2.65	71.78	1.32	430.00	8.65
4.10	121.76	4.67	124.69	3.19	112.45	2.65	72.49	1.27	432.45	9.01
4.20	118.64	4.56	124.14	3.43	112.31	2.67	72.59	1.27	429.25	9.50
4.30	114.99	4.28	123.39	3.31	112.05	2.66	72.63	1.60	425.15	9.07

Table 11.12: On-orbit HRMA Effective Area within  $2\pi$  Steradian. Units:  $\text{cm}^2$  (continued)

Energy (keV)	Shell 1		Shell 3		Shell 4		Shell 6		HRMA	
	$A_{eff}$	Error								
4.40	112.06	4.23	123.42	3.39	112.41	2.89	72.97	1.33	423.55	8.61
4.50	107.82	4.23	122.56	3.70	112.11	3.23	73.02	1.79	418.69	9.43
4.60	102.85	3.95	121.39	3.35	111.60	2.67	72.98	1.34	412.44	8.46
4.70	96.25	3.70	120.78	3.28	111.78	3.64	73.39	1.56	405.99	11.05
4.80	90.83	3.68	119.72	3.56	111.41	2.96	73.43	1.33	399.52	8.32
4.90	84.84	3.34	118.73	3.18	111.15	2.89	73.54	2.09	392.59	10.69
5.00	78.31	3.42	117.20	3.09	110.46	2.65	73.46	1.32	383.89	7.88
5.10	70.79	2.83	115.80	3.22	109.99	2.67	73.50	1.57	374.36	9.37
5.20	63.10	2.66	114.18	3.02	109.37	2.72	73.48	1.35	364.13	7.40
5.30	54.81	2.40	112.54	3.29	108.79	2.91	73.51	1.38	353.11	9.33
5.40	46.30	2.05	110.30	3.15	107.82	2.69	73.38	1.30	340.54	7.16
5.50	37.56	1.64	107.72	2.86	106.72	2.64	73.22	1.32	327.01	6.68
5.60	29.60	1.28	105.07	2.75	105.66	2.57	73.10	1.70	314.22	6.42
5.70	22.90	1.11	102.39	2.78	104.66	2.60	73.04	1.31	302.93	6.49
5.80	17.45	0.92	99.63	2.70	103.74	2.92	73.02	1.35	293.11	6.19
5.90	12.47	0.57	96.23	2.52	102.81	2.71	73.11	1.62	283.17	6.15
6.00	9.47	0.60	92.76	2.43	101.68	2.55	73.06	1.32	275.31	6.42
6.10	7.19	0.39	88.66	2.57	100.29	2.46	72.94	1.55	267.37	6.69
6.20	5.49	0.32	83.90	2.60	98.68	2.44	72.77	1.31	259.19	5.24
6.30	4.20	0.67	78.57	2.33	96.99	2.37	72.61	1.57	250.84	5.20
6.40	3.23	0.18	72.37	2.08	95.06	2.39	72.43	1.33	241.74	4.89
6.50	2.52	0.13	65.28	2.13	92.58	2.28	72.08	1.29	231.33	5.16
6.60	1.96	0.27	57.88	1.80	90.60	3.26	72.05	1.49	221.54	5.12
6.70	1.51	0.27	49.50	1.63	88.44	2.48	72.13	1.29	210.82	4.37
6.80	2.12	0.09	41.67	1.09	85.63	2.43	71.91	1.63	199.88	5.34
6.90	1.75	0.07	33.92	1.49	82.05	3.81	71.52	2.28	188.14	6.66
7.00	1.44	0.06	26.90	0.85	78.38	2.38	71.30	3.57	177.25	6.97
7.10	1.20	0.05	20.80	0.54	73.87	4.35	70.95	3.09	166.37	7.90
7.20	1.01	0.04	16.19	0.74	68.05	1.96	70.03	1.26	155.16	3.12
7.40	0.69	0.03	9.19	0.34	56.85	1.42	70.38	1.33	137.10	2.83
7.60	0.51	0.02	5.85	0.50	43.54	2.00	69.69	1.91	119.69	4.44
7.80	0.38	0.02	3.83	0.33	29.97	0.76	68.88	1.48	103.18	2.05
8.00	0.29	0.01	2.54	0.23	18.44	0.49	67.94	2.62	89.34	2.95
8.20	0.22	0.01	1.75	0.06	11.08	0.29	66.87	1.78	80.08	2.08
8.40	0.17	0.01	1.27	0.03	7.01	0.18	65.91	1.25	74.60	1.67
8.60	0.13	0.01	0.92	0.04	4.48	0.12	64.31	2.23	70.17	1.81
8.80	0.10	0.00	0.72	0.02	2.94	0.35	62.75	1.47	66.89	2.95
9.00	0.08	0.00	0.53	0.01	1.99	0.07	60.82	1.42	63.94	1.94
9.20	0.06	0.00	0.40	0.01	1.40	0.11	58.04	1.18	60.50	1.28
9.40	0.05	0.00	0.30	0.01	0.99	0.03	54.91	1.99	56.95	1.49
9.60	0.04	0.00	0.24	0.01	0.75	0.02	50.26	2.11	52.02	2.62
9.80	0.03	0.00	0.19	0.00	0.56	0.02	43.80	1.70	45.29	2.09
10.00	0.03	0.00	0.14	0.00	0.41	0.01	34.76	0.89	35.97	1.15

## 11.19 Conclusion

The HRMA calibration at the XRCF of MSFC made novel use of the X-ray continuum radiation from a conventional electron-impact source. Taking advantage of the good spectral resolution of solid-state detectors, continuum measurements proved advantageous in calibrating the effective area of AXAF's High-Resolution Mirror Assembly (HRMA) for the entire AXAF energy band.

The HRMA effective area was obtained by comparing the spectrum detected by a SSD at the focal plane with the spectrum detected by a beam normalization SSD in Building 500. Many systematic effects such as pileup, deadtime, beam uniformity, energy scale, icing, relative quantum efficiency, background, *etc.*, must be analyzed during the data reduction process.

In the data analysis, we did not use the actual SSD spectral response matrices. This could introduce an error as the energy resolutions of the two SSDs are slightly different. However, we did convolutions of the preliminary SSD spectral response matrices with the calibration data scaled raytrace predictions, and compared them with the measured effective area for each shell. The fit was reasonably good. Had we used the original raytrace prediction in the convolution, the fit would not be acceptable. This justifies the method we used to reduce the data and the calibrated effective area we generated. This work will be improved in the near future by using more detailed SSD response matrices calibrated at the BESSY to unfold the spectra and a pileup correction model as a continuous function of energy.

The results of the SSD C-continuum measurements show that the measured effective area is substantially less than the predicted effective area by well more than the experimental errors, especially for shell 1. Although we still don't have a good explanation for the cause or causes of this discrepancy on this important AXAF capability, we are currently assessing the reflectivity and surface scattering calculations in our raytrace model. When this is done, we will re-assess the differences between the data and the model, and, if necessary, apply similar, but smaller, polynomial corrections to our improved raytrace predictions.

Presently we have yet to achieve the calibration goal of 1% precision for the HRMA effective area. We expect to approach this goal as this work progresses.

Based on the SSD C-continuum Measurements at the XRCF, we have calibrated the HRMA effective area for its on-orbit performance as well as its actual values at the XRCF. The HRMA effective area is one of the most important AXAF capabilities. These calibrated values of the effective area can be used to make AXAF on-orbit performance predictions, and by other AXAF teams to calibrate their science instruments.

The HRMA effective area "rdb" tables and their figures are available on the World Wide Web pages for:

XRCF: [http://hea-www.harvard.edu/MST/mirror/www/xrcf/hrma\\_ea.html](http://hea-www.harvard.edu/MST/mirror/www/xrcf/hrma_ea.html)

On-orbit: [http://hea-www.harvard.edu/MST/mirror/www/orbit/hrma\\_ea.html](http://hea-www.harvard.edu/MST/mirror/www/orbit/hrma_ea.html)

